UC Irvine
UC Irvine Electronic Theses and Dissertations

Title

Exploring Niobium Oxide Nanostructures for Lithium-Ion Energy Storage

Permalink

https://escholarship.org/uc/item/4dr8v3gv

Author

Andoni, Ilektra

Publication Date

2022

Peer reviewed|Thesis/dissertation

UNIVERSITY OF CALIFORNIA,
IRVINE

Exploring Niobium Oxide Nanostructures for Lithium-Ion Energy Storage

DISSERTATION

submitted in partial satisfaction of the requirements
for the degree of

DOCTOR OF PHILOSOPHY

in Chemistry

by

Ilektra Andoni

Dissertation Committee:
Professor Reginald Penner, Chair
Professor Matthew Law
Professor Robert M. Corn

2022

TABLE OF CONTENTS

LIST OF FIGURES

LIST OF TABLES

ACKNOWLEDGMENTS

of Mesoporous Niobium(V) Oxide Nanoscopic Films. *Chem. Mater.* **2018**, *30*, 6549–6558. (`https://doi.org/10.1021/acs.chemmater.8b03254`).

The text of Chapter 2 is an adaptation/reprint of the material as it appears in Pender, J. P.; Jha, G.; Youn, D. H.; Ziegler, J. M.; Andoni, I.; Choi, E. J.; Heller, A.; Dunn, B. S.; Weiss, P. S.; Penner, R. M.; Mullins, C. B. Electrode Degradation in Lithium-Ion Batteries. *ACS Nano* **2020**, *14* (2), 1243–1295. (`https://pubs.acs.org/doi/full/10.1021/acsnano.9b04365`), used with permission from The American Chemical Society. Further permissions related to the material excerpted should be directed to the ACS.

The text of Chapter 3 is a reprint of the material as it appears in Andoni, I.; Ziegler, J. M.; Jha, G.; Gadre, C. A.; Flores-Zuleta, H.; Dai, S.; Qiao, S.; Xu, M.; Chen, V. T.; Pan, X.; Penner, R. M. Investigating the Degradation of Nb2O5 Thin Films Across 10,000 Lithiation/Delithiation Cycles. *ACS Appl. Energy Mater.* **2021**, *4*, 6542–6552. (`https://pubs.acs.org/doi/10.1021/acsaem.1c00580`), used with permission from The American Chemical Society.

VITA

Ilektra Andoni

EDUCATION

Doctor of Philosophy in Chemistry **2022**
University of California Irvine *Irvine, CA*

Master of Science in Chemistry **2021**
University of California Irvine *Irvine, CA*

Bachelor of Science in Biochemistry **2017**
Boston College *Chestnut Hill, MA*

RESEARCH EXPERIENCE

Graduate Research Assistant **2018-2022**
University of California, Irvine *Irvine, California*

Undergraduate Research Assistant **2015-2017**
Boston College *Chestnut Hill, MA*

Summer Undergraduate Research Assistant **2016**
Boston College *Chestnut Hill, MA*

TEACHING EXPERIENCE

Chemistry Teaching Assistant **2017-2022**
University of California, Irvine *Irvine, California*

REFEREED JOURNAL PUBLICATIONS

Investigating the Degradation of Nb$_2$O$_5$ Thin Films across 10,000 Lithiation/Delithiation Cycles   **2021**
ACS Applied Energy Materials

Sensors Based Upon Nanowires, Nanotubes, and Nanoribbons: 2016-2020   **2020**
Analytical Chemistry

Electrode Degradation in Lithium-Ion Batteries   **2020**
ACS Nano

Strain-Enhanced Metallic Intermixing in Shape-Controlled Multilayered Core-Shell Nanostructures: Toward Shaped Intermetallics   **2020**
Angewandte Chemie

Promotion of the Halide Effect in the Formation of Shaped Metal Nanocrystals via a Hybrid Cationic, Polymeric Stabilizer: Octahedra, Cubes, and Anisotropic Growth   **2016**
Surface Science

ABSTRACT OF THE DISSERTATION

Exploring Niobium Oxide Nanostructures for Lithium-Ion Energy Storage

By

Ilektra Andoni

Doctor of Philosophy in Chemistry

University of California, Irvine, 2022

Professor Reginald Penner, Chair

Niobium pentoxide, Nb_2O_5, is a lithium-ion battery anode material that exhibits pseudoca-pacitance, particularly in the orthorhombic phase, from fast lithium intercalation kinetics. While the electrochemical characteristics of this material have been well studied, there is a gap in the knowledge of long-term cycle stability and degradation analysis of this material. Upon 10,000 lithiation/delithiation cycles, the main degradation pathways observed for electrophoretically deposited thin films of orthorhombic Nb_2O_5 were amorphization of the orthorhombic structure and delamination of the thin films from the current collector. Additionally, these films boasted exceptional capacities that exceeded the theoretical Faradaic capacity. This phenomenon can be attributed to high non-Faradaic surface capacitance arising from the observed 70% porosity of the films. Since pristine Nb_2O_5 is very insulating, these pores can only be accessed and contribute significantly to the capacitance if the conductivity of the films changes as a function of lithiation. *In situ* conductivity measurements of T-Nb_2O_5 nanoribbons illustrate a large $\sim$2000-fold increase in conductivity upon lithiation. Study of degradation and conductivity of electrophoretically deposited T-Nb_2O_5 is crucial in understanding why this material can perform beyond theoretical limits and how the electrochemical performance can be further improved.

Chapter 1

Introduction

1.1 Lithium-Ion Batteries and Electrochemical Capacitors

Lithium ion batteries (LIBs) have become increasingly popular as energy storage devices since the first rechargeable LIB in 1976 by Whittingham.[1,2] Research over the years has explored alterations of all main aspects of the battery - cathode, anode, and electrolyte - in attempts to improve energy storage, charge/discharge time, and longevity of the batteries (Figure 1.1).[2–4]
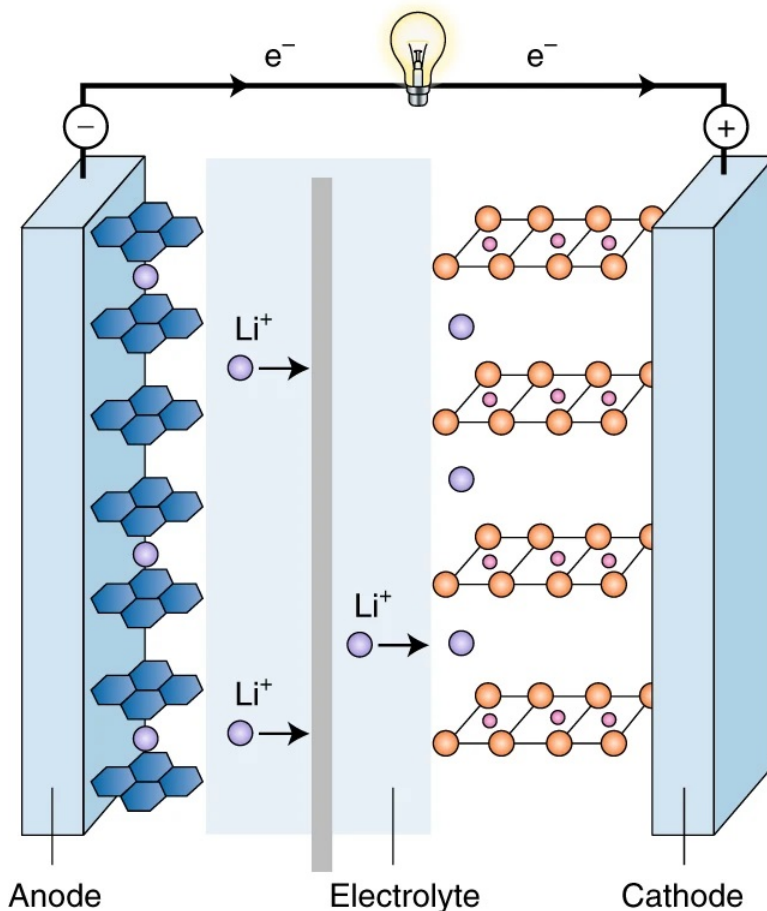
Figure 1.1: Components of a Rechargeable Lithium-Ion Battery. Reprinted by permission from Springer Nature Customer Service Centre GmbH: Springer Nature, Nature Electronics, ref 3, Copyright 2018.

A Ragone plot represents a couple of the most important metrics in energy storage materials: the specific energy (Wh/kg), which is related to the specific capacity, is a measure of how much charge the battery can store, and specific power (W/kg), which is related to the charge/discharge rate, is a measure of how quickly the battery can charge and discharge (Figure 1.2).[4–7] LIBs have excelled in specific energy but are lacking in specific power metrics due to diffusion-limited Faradaic electrochemistry that cannot occur at fast rates (Figure 1.2, green). On the other hand, traditional capacitors have high specific power due to fast non-Faradaic capacitive charge storage but poor specific energy since stored charge is limited by the surface area (Figure 1.2, gray). Thus, research in materials that are able

store energy in both ways is necessary to realize high capacity, high rate electrochemical energy storage.[4-7] These materials, called electrochemical capacitors (ECs), mainly consist of two categories: electrochemical double layer capacitors (EDLCs), also known as supercapacitors, and pseudocapacitors.[4,5] EDLCs store charge in a capacitor-like fashion with the electrostatic adsorption of electrolyte ions onto a high surface area, electrochemically stable, active material. Since there is no redox chemistry occurring in these materials, the specific energy is generally very low and these materials excel more in terms of specific power and longevity.[4,5] On the other hand, pseudocapacitive materials utilize redox electrochemistry and lie closer to LIBs.[4,5] The unique energy storage characteristics of pseudocapacitors set them apart from EDLCs and will be further explored in this thesis.
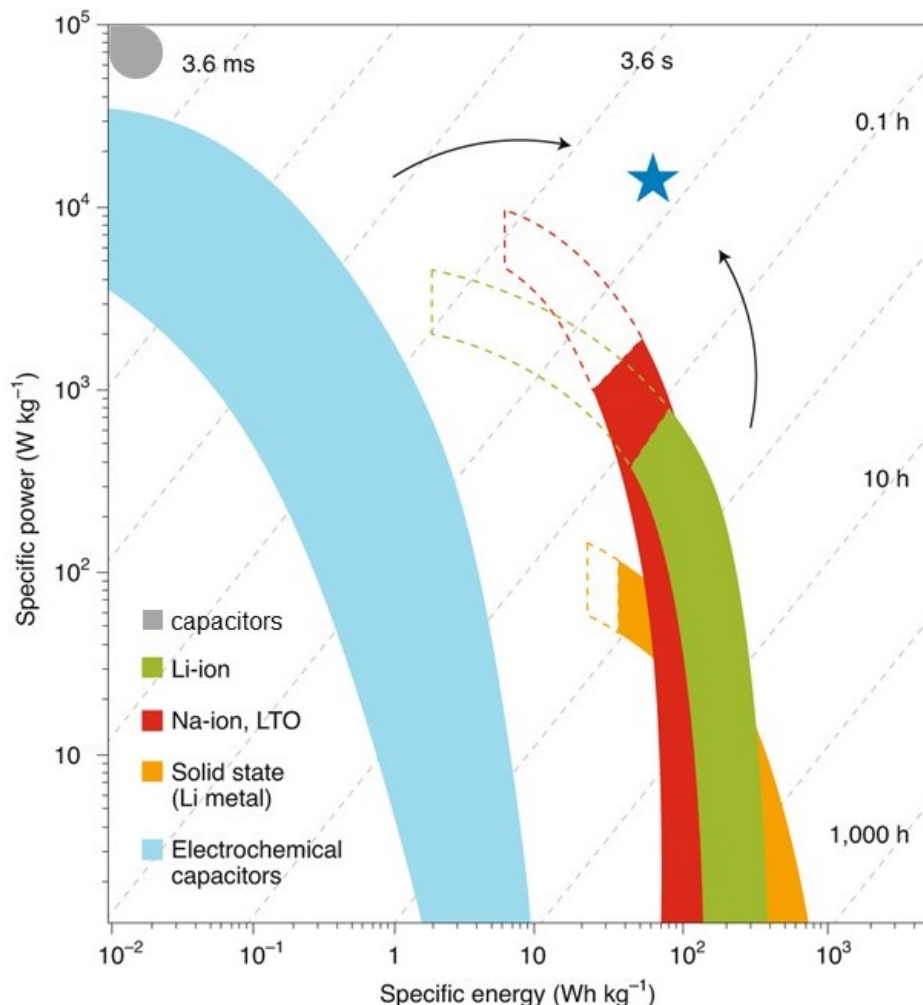
Figure 1.2: Ragone plot for electrochemical energy storage devices. The plot shows the trends towards greater specific power for batteries and specific energy for electrochemical capacitors (arrows), blurring the boundaries between the two as the trends approach the star. Dashed lines represent zones where the cyclability of the device is altered in the case of symmetric cycling (same charging and discharging rate at 100% depth of discharge). For Li-ion batteries, Li plating at the negative electrode is mainly responsible for the decrease in cycle life and the limitation of charging rate. All the data for generating this figure come from commercial devices (data sheets or real tests). The data for solid state batteries come from industry road maps The diagonal dotted lines and timescales represent characteristic operation timescales, obtained by dividing the energy by the power. LTO, lithium titanium oxide ($Li_4Ti_5O_{12}$). Adapted by permission from Springer Nature Customer Service Centre GmbH: Springer Nature, Nature Materials, ref 5, Copyright 2020.

1.2 Pseudocapacitive Materials

Pseudocapacitive materials take advantage of both electrostatic charge storage and redox reactions, resulting in a hybrid between capacitors and batteries.[4–7] Electrochemical, reversible redox reactions in pseudocapacitive materials occur either at the surface of the electrode or with fast kinetics such that the reactions are not limited by solid-state diffusion.[6,7] This allows these materials to store energy in the same way as LIBs but charge/discharge on the time scale of EDLCs, thus achieving high specific energy and specific power.

Two main types of pseudocapacitive phenomenon have been studied extensively: redox pseudocapacitance and intercalation pseudocapacitance.[5–7] Redox pseudocapacitance is well modeled by RuO_2 and MnO_2 and is characterized by fast redox reactions confined to the active material surface. In addition to surface redox, there is also insertion of lithium into the bulk of the material in intercalation pseudocapacitance. In pseudocapacitive materials, intercalation is allowed by layered crystal structures or low energy lithium pathways in the crystal structure, but intercalation does not induce a phase change in the material as seen with traditional LIBs electrodes.[5–7] Although these two types of pseudocapacitive materials differ slightly in their mechanism, they can be identified across three electrochemical methods: cyclic voltammetry, galvanostatic charge/discharge curves, and impedance spectroscopy (Figure 1.3). Cyclic voltammetry (CV) of pseudocapacitive materials will result in a rectangular shape due to capacitor-like charge storage and if redox peaks are present, they will have little to no separation between peak potentials due to fast, reversible redox electrochemistry. Galvanostatic charge/discharge curves will appear to be more similar to a capacitor profile, which is linear and sloped, instead of the "S" shape signature to batteries caused by phase transformations and diffusion-limited processes. Finally, impedance spectroscopy Nyquist plots of capacitors are vertical lines and pseudocapacitors are similarly straight lines with a phase angle of less than 90° with possible semi-circles at high frequency due to charge-transfer resistance.[5–7]
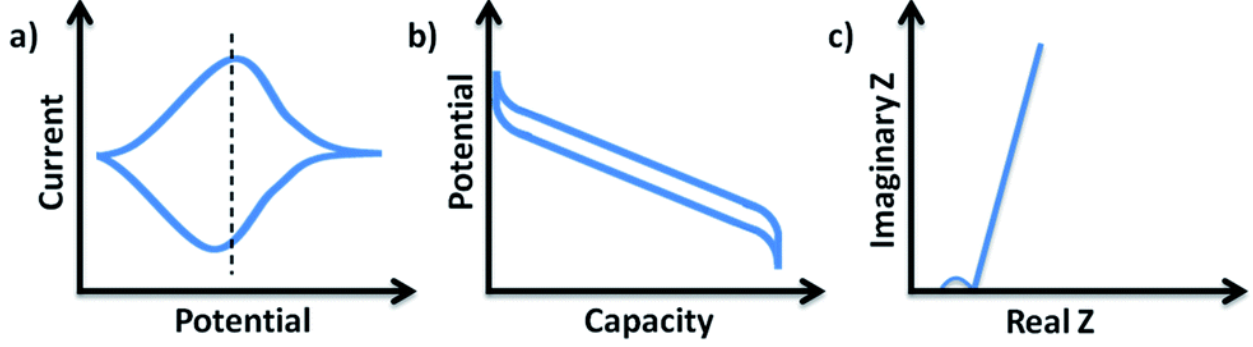
Figure 1.3: Electrochemical characteristics of pseudocapacitive materials.The general electrochemical features of pseudocapacitive materials. (a) In a cyclic voltammetry experiment, the shape is rectangular and if peaks are present, they are broad and exhibit a small peak-to-peak voltage separation. (b) In a galvanostatic experiment, the shape is sloping so that a capacitance value, $\Delta Q/\Delta V$, may be assigned at each point, and the voltage hysteresis is small. Here, Q is the capacity and V is the potential window. (c) In an AC impedance experiment, the Nyquist representation will contain a vertical line with a phase angle of 90° or less. A semi-circle at high frequencies, associated with charge-transfer resistance, may also be present. Used with permission of the Royal Society of Chemistry from ref 6 Copyright 2014; permission conveyed through Copyright Clearance Center, Inc.

Currents observed in pseudocapacitive materials are sums of currents from capacitive mechanisms and diffusion-limited mechanisms. It is well-known that the dependence of peak current on scan rate can indicate if the current is capacitive or limited by diffusion. Capacitive current is linearly dependent on scan rate while diffusion-limited current is linearly dependent on the square root of the scan rate. Considering that both contribute to the current in pseudocapacitive materials, the total current in pseudocapacitive materials is the sum of capacitive current and diffusion-limited current as modeled by Equation 1.1:[6–9]

$$i\left(V\right) = k_1 v^{\frac{1}{2}} + k_2 v \qquad (1.1)$$

where $i(V)$ is the current at each potential, ν is the scan rate, and k_1 and k_2 are calculated constants that respectively represent the weight of the diffusion-limited current and capacitive current at each potential. k_1 and k_2 are calculated by dividing both sizes of the equation by $v^{\frac{1}{2}}$ and fitting the plots of $i(V)/v^{\frac{1}{2}}$ versus $v^{\frac{1}{2}}$ to a line. This process is repeated for every

potential to extract k_1 and k_2 values at each potential. By doing this, the contributions to current from the two components can be deconvoluted. In intercalation pseudocapacitance, ions intercalate into the structure of a redox-active material. In these materials, diffusion-limited current is due to Faradaic processes at metal centers upon insertion, but if lithium kinetics are fast, lithium insertion will actually contribute to the capacitive current and add to the current due to surface charging.[6,7]

When discussing charge storage in energy storage electrodes, it is important to understand the difference between capacity and capacitance and which one should be used. Both quantify the amount of charge stored, but generally, capacity is used for battery electrodes and capacitance is used for capacitors. Specific capacity, represented in units of mAh/g, can be calculated theoretically using x, the number of electrons transferred in the reaction, F, Faraday's constant, n, the number of moles of active material, and M, the molar mass of the active material as shown in Equation 1.2:[2]

$$C_{sp} = \frac{xF}{nM} \tag{1.2}$$

Experimentally, the specific capacity is calculated by determining the charge stored, current (mA) $\times$ time (h), and dividing by the mass of the active material. Generally, the value of specific capacity corresponds to galvanostatic measurements. Specific capacitance, represented in units of F/g, typically relates to CV measurements and can be calculated theoretically by dividing the specific capacity by the voltage window used in the CV. Experimentally, the charge stored, Q is calculated by averaging the area under the cathodic and anodic sweeps of the CV and then dividing by the scan rate. The charge is then divided by the voltage window and the mass of active material to obtain the specific capacitance. Because pseudo-capacitors display capacitor- and battery-like behavior, both capacity and capacitance can be assessed. However, since capacitance is dependent on the voltage window, it is difficult to make direct comparisons between results. Thus, capacity is preferred since the value is

consistent for a certain material.[10]

1.3 Niobium Pentoxide

Niobium pentoxide (Nb_2O_5) is a material that displays intercalation pseudocapacitance with a theoretical capacity of 202 mAh/g.[11,12] Research in Nb_2O_5 has been pioneered by the group of Bruce Dunn with detailed studies on the kinetics and electrochemical properties that defined Nb_2O_5 as a pseudocapacitive material and identified changes in the energy storage with crystal structure.[8,11] Intercalation of lithium into Nb_2O_5 is associated with reduction of the niobium metal centers from Nb^{5+} to Nb^{4+}, and the material is capable of storing up to two lithium ions as shown in Equation 1.3:

$$xLi^+ + xe^- + Nb_2O_5 \leftrightarrow Li_xNb_2O_5 \tag{1.3}$$

The crystal structure of Nb_2O_5 can be varied with annealing in air in the range of 400 ^oC to 1000 ^oC.[13] In the orthorhombic (T-Nb_2O_5) and pseudo-hexagonal structures (TT-Nb_2O_5), interstitial sites in the (001) plane can be occupied by lithium ions to store charge.[8,11] The large oxygen-oxygen spacing in the plane offers a low-energy diffusion barrier of lithium ion hopping. However, the orthorhombic structure can store more charge than the pseudo-hexagonal structure due to additional fast lithium ion kinetics in the (180) plane (Figure 1.4).[8] The fast lithium kinetics observed in these channels gives rise to a huge capacitive contribution, approximately 80% to the total capacity. This means that even at very fast rates, i.e. short charge/discharge time scales, 80% of the capacity can be retained due to pseudocapacitive current from diffusion independent surface charging and fast lithium insertion into the lattice.[8]
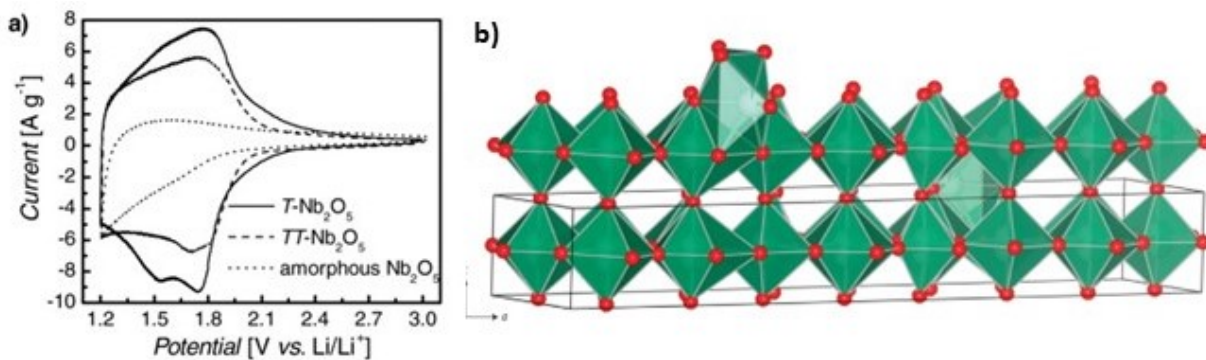
Figure 1.4: Literature Nb_2O_5 Cyclic Voltammetry and Orthorhombic Nb_2O_5 Crystal Structure.a) Voltammetric sweeps for Nb_2O_5 in lithium ion electrolyte. CVs at 10 mV/s for different Nb_2O_5 phases. Reproduced with permission from ref 8 Copyright 2012 WILEY-VCH Verlag GmbH & Co. KGaA, Weinheim b) The structure of T-Nb_2O_5 stacked along the c axis demonstrates the layered arrangement of oxygen (red) and niobium (inside polyhedra) atoms along the a–b plane. Reprinted by permission from Springer Nature Customer Service Centre GmbH: Springer Nature, Nature Materials, ref 11, Copyright 2013.

1.4 Electrophoretic Deposition of Nb_2O_5 Thin Films

The most common ways to synthesis Nb_2O_5 is via hydrothermal reaction of ammonium niobate oxalate hydrate or sol-gel synthesis from niobium chloride salt which are then cast onto a current collector with the addition of binders and conductive supports.[8,11,14–16] Alternatively, niobium metal can be anodized and annealed to achieve the desired crystal structure.[17] Although reports on these methods reveal great electrochemical results, an intimate electrical contact between the active material and the current collector can not be achieved in the mentioned methods as it can be with electrodeposition of Nb_2O_5.

Electrodeposition of the electrode materials provides a better electrical contact between the active material and the current collector and more control over the dimensions of the active material. Pourbaix diagrams can be used to hypothesize how to electrodeposit a material from a solution of its salts by altering the pH, applied voltage, or a combination of both.

However, the Pourbaix diagram of niobium does not pose a direct way of electrodepositing T-Nb_2O_5 which challenges the use of this fabrication method.[18]

T-Nb_2O_5 films can instead be electrodeposited indirectly via electrophoretic deposition (EPD) as described by Zhitomirsky.[19–21] Colloidal NbO_x solutions can be made from cold injection of methanolic $NbCl_5$ solutions into dilute ~ 2 ^oC hydrogen peroxide. The resulting colloids are niobium oxide peroxocations with an overall positive charge. When the current collector is placed into solution and biased at least -2 V versus the counter electrode, the positively charged colloids migrate to the negatively biased current collector. At such a negative voltage, H_2 is evolved at the working electrode from the reduction of water. This reaction causes a build-up of OH^- ions at the surface of the electrode which hydrolyze the peroxocations and Nb_2O_5 is deposited onto the working electrode surface.[19–21] Additionally, H_2 co-evolution at the electrode surface is hypothesized to cause porosity in the film if H_2 nanobubbles are trapped within the film during deposition.[12] Following deposition, the films are calcined in air at 550 ^oC to achieve the orthorhombic crystal structure which is confirmed by x-ray diffraction (XRD).

EPD T-Nb_2O_5 thin films were characterized electrochemically via cyclic voltammetry and galvanostatic cycling (Figure 1.5a,c). Although scan rate series of films from 5 to 500 mV/s show rapid capacitance fade as the scan rate increases, the measured capacitance for thinner films at high scan rates still show high capacitance versus the theoretical capacitance of 403 F/g (Fig 1.5b). At 200 mV/s, the average cycle stability is a 20% fade in capacitance in the first 2000 cycles. The films exceed the theoretical capacity by $\sim$50 mAh/g in the 38 and 60 nm films at high charge/discharge rates of 50 A/g with up to almost 400 mAh/g of excess capacity at slower rates (Figure 1.5d). At 10 A/g, the films are able to cycle for 400 cycles on average before a 20% capacity fade is realized. Overall, these metrics place the films at a much higher specific power and energy as compared to other work indicating the advantages of EPD in making T-Nb_2O_5 thin films.[12]
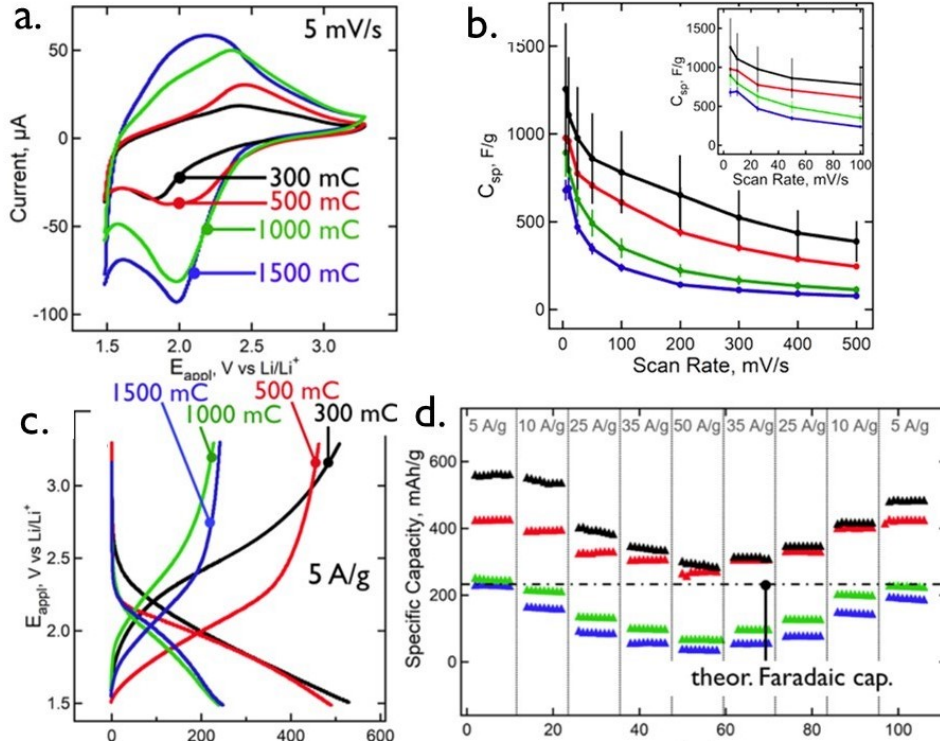
Figure 1.5: Electrochemical characterization of Nb_2O_5 thin films. a) cyclic voltammetry of four film thicknesses at 5 mV/s with b) scan rate dependence of the specific capacitance (theoretical value 403 F/g). c) galvannostatic charge/discharge curves for four film thicknesses at 5 A/g with d) measurements for specific capacity at five galvannostatic rates ranging from 5 to 50 A/g (theoretical value 202 mAh/g). Adapted with permission from ref 12. Copyright 2018 American Chemical Society

As discussed previously, T-Nb_2O_5 stores energy through pseudocapacitive lithiation. Using the scan rate series, the capacitance of the films is deconvoluted into the capacitive (non-insertion) and diffusion-limited (insertion) components.[8,9] Deconvolution shows that at most scan rates, the current is mostly due to non-insertion capacitance which is independent of the scan rate and exceeds the theoretical capacitance for the voltage window (Fig 1.6).[12] This implies that most of the film's capacitance is due to surface effects, and there must be accessible high surface area within the film.
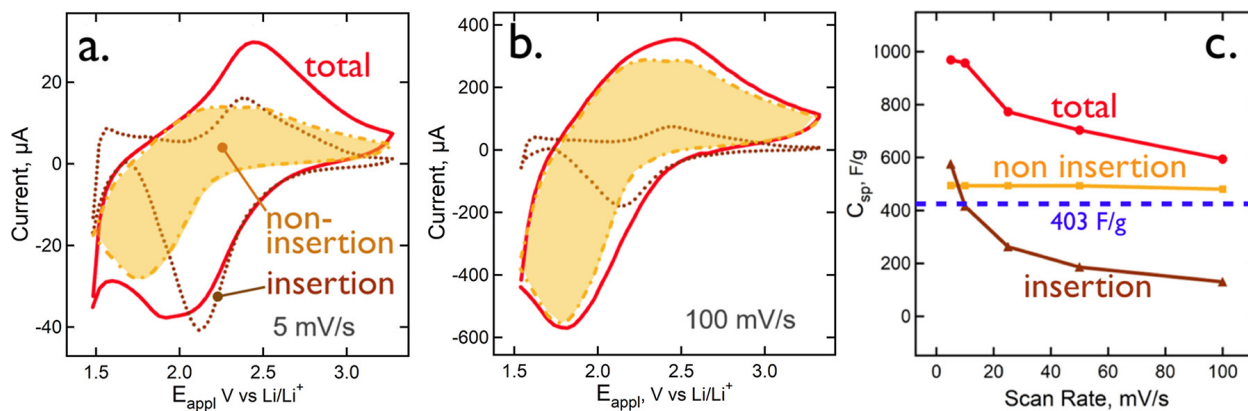
Figure 1.6: Deconvolution of insertion and non-insertion currents in a cyclic voltammogram (a) CV at 5 mV/s for a 500 mC T-Nb_2O_5 film. (b) CV for the same film at 100 mV/s. (c) Plot of total C_{sp}, together with the insertion and non-insertion capacities as a function of scan rate, ν. The dashed blue line marks the theoretical Faradaic capacity, 403 F/g for a 1.8 V window. Reproduced with permission from ref 12. Copyright 2018 American Chemical Society

Porosity in the films is proposed to be the cause of this high surface area. Calculations considering the lithographically controlled deposition area, atomic force microscopy (AFM) measurements of the thickness, quartz crystal microbalance (QCM) measurements of the deposited mass, and theoretical density allow for an estimation of the porosity in the film. The calculations predict that the film is approximately 70% porous, and cross-sectional transmission electron microscopy (TEM) imaging shows small pores in the film. These are hypothesized to be caused by trapped hydrogen bubbles co-evolved during deposition which leave behind pores when the film is annealed.[12]

1.5 Scope of Research

In this thesis, questions raised during the study of EPD of T-Nb_2O_5 are further explored. The method of EPD to fabricate energy storage T-Nb_2O_5 electrodes is new to the field and presents some promising, yet anomalous performance particularly in the high capacitance

that exceeds the theoretical value.

1.5.1 Degradation of Niobium Oxide Thin Film Electrodes

One of the most common issues with energy storage devices is the longevity, or cycle stability, of the active material. Extensive research has been put into understanding and mitigating the degradation pathways that cause capacity fade in lithium-ion energy storage materials. These findings are summarized in Chapter 2 which highlights degradation pathways for intercalation cathodes and anodes and further details the short comings of anode materials similar to T-Nb_2O_5. With this background knowledge, the degradation of T-Nb_2O_5 can be better understood.

As mentioned, the capacitance of EPD T-Nb_2O_5 thin films decreases by 20% in the first 1000-3000 cycles. It is important to understand what degradation pathways cause this capacitance fade to explore improvements to the EPD method. To do this, the T-Nb_2O_5 thin films are cycled to 10,000 cycles and characterized *ex-situ* at regular cycle intervals to track changes in structural, chemical, and electrical integrity. These results are reported in Chapter 3.

1.5.2 Investigation of T-Nb_2O_5 Conductivity as a Function of Lithiation

The most anomalous feature of the T-Nb_2O_5 EPD thin films is the capacitance that exceeds the theoretical Faradaic value. While the porosity proposes a physical path for increase in capacitance, Nb_2O_5 is relatively insulating with a low conductivity of $\sim$3.3 x 10^{-6} S/cm at 330 K and a large band gap of 3.4 eV.[8] Therefore, even if there is high surface area embedded into the film, these areas are only accessible if the conductivity of the film allows it. Thus, it is proposed that the conductivity of the film increases drastically as a function of lithiation

which allows for access to these high surface area regions and a non-insertion capacitance that exceeds the theoretical Faradaic value. In Chapter 4, a nanoribbon device is used to study the changes in conductivity through T-Nb$_2$O$_5$ as the material is lithiated at several potentials.

Chapter 2

Electrode Degradation in Lithium-Ion Batteries

2.1 Introduction

The need for energy-storage devices that facilitate the transition from fossil-fuel-based power to electric power has motivated significant research into the development of electrode materials for rechargeable metal-ion batteries based on Li^+, Na^+, K^+, Mg^{2+}, Zn^{2+}, and Al^{3+}. The lithium-ion rechargeable battery (LIB) has been by far the most successful, enabling the wireless revolution of portable electronics (e.g., cell phones, laptops, digital cameras, power tools, etc.) and emerging as the battery-of-choice for electric vehicles (EVs) and intermittent energy storage (i.e., from wind and solar) due to their high energy density and decreasing costs.[22,23] However, traditional LIBs are also often a limiting factor; in portable electronics, LIBs typically occupy large portions of the mass and volume, and EVs powered by LIBs typically offer small driving ranges or are expensive due to the costs of the large LIB packs and maintenance systems.[22–26] Increases in battery energy density, particularly per unit vol-

ume, would relieve these limitations and greatly expand the possibilities of LIB-powered devices.[24,25] A battery's deliverable energy is a function of its voltage and capacity and can be maximized by (1) having a large potential difference between the anode and cathode, (2) minimizing the mass and volume of active material per exchanged electron, and (3) avoiding oxidation or reduction (and thus consumption) of the liquid electrolyte.[26]

The most commercially successful electrodes are based on "intercalation materials" that reversibly insert ions through ionconductive one-dimensional (1D) paths or two-dimensional (2D) planes in layered, crystalline materials. This chemistry has proven useful due to the low-volume expansion and contraction when accepting ("lithiating") or releasing ("delithiating") Li^+ that provides suitable mechanical and electrochemical stability for long-term use. A typical LIB consists of a transition-metal oxide cathode (e.g., $LiCoO_2$) and a graphite anode. These "Li-storing" materials are mixed with a conductive additive (typically carbon black) and a polymer binder (commonly poly(vinylidene difluoride), PVDF) and cast onto both sides of either aluminum foil (cathode) or copper foil (anode) with an insulating polymer membrane sandwiched between electrode layers to prevent shortcircuiting.[27] The restriction in energy density in this design arises from the low Li^+:host stoichiometries of intercalation materials (e.g., high mass/volume of material per Li^+ stored) that require numerous stacks of electrodes (and thus numerous metal foils and separators) to meet a given energy requirement. Figure 2.1 shows the breakdown of the weight occupied by LIB cell components (Figure 2.1a) and the specific energy targets for LIBs in automotive applications (Figure 2.1b).[24,25,28–30] Although the cathode and anode active materials already comprise the largest and heaviest components of LIBs, further increasing battery energy density requires reducing the proportional weight and volume of separator membranes and metal-foil current collectors. This pursuit has motivated significant research into the development of high-capacity electrode materials and architectures that store more Li^+ per unit mass and volume.[22–26]
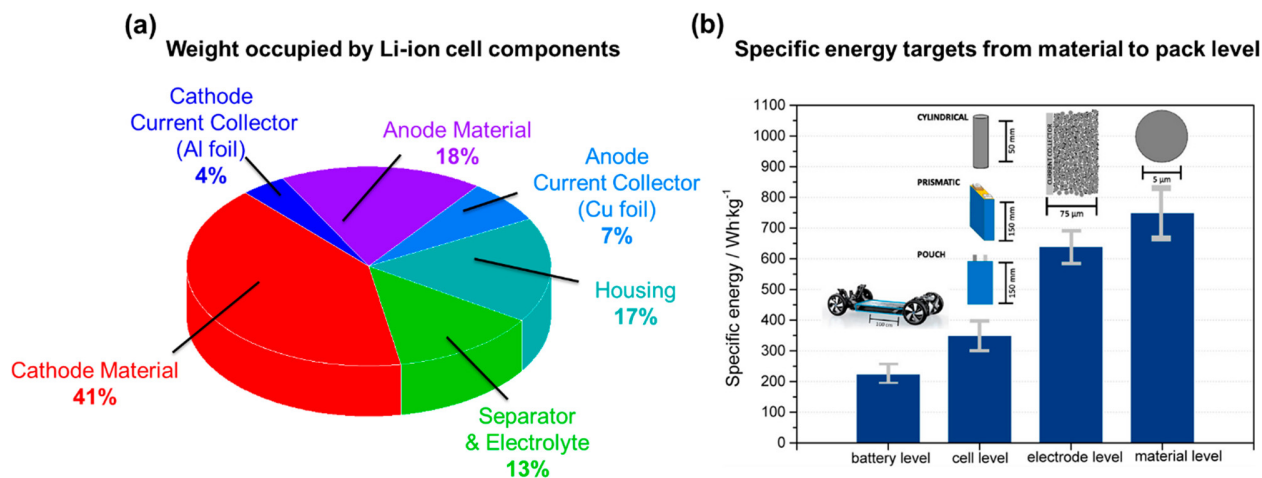
Figure 2.1: Summary of Lithium-Ion Battery Cell Components and Specific Energy Targets. (a) Chart showing the weight fraction occupied by the components of a commercial lithium-ion battery cell. Adapted from with permission from ref (30). Copyright 2014 Royal Society of Chemistry. (b) Specific energy targets for automotive applications from material to pack level. Reproduced from ref (28). Copyright 2017 American Chemical Society.

The degradation mechanisms for intercalation electrodes, the characterization methods that help deconvolute reaction complexity, and the inspired attempts by researchers to prevent or to circumvent electrode degradation in high performance battery electrodes will be discussed in this chapter.

2.2 Cathode Materials

Cathodes are the Achilles' heels of LIBs. With a reversible capacity of 372 mAhg^{-1}, the graphite anode has a capacity much higher than that of the cathode materials that are usually paired with it in commercial batteries. In small lithium-ion cells, for example, $LiCoO_2$ (LCO) cathodes with a usable capacity of 160 mAhg^{-1} and ~60% lithium utilization are widely used.[31] This capacity asymmetry is one factor that has motivated a search for higher-capacity cathode materials that source and sink metal-ions rapidly and reversibly at the requisite positive potentials. A second factor is the high cost of cobalt, and thus many other

cathode formulations have been described in excellent reviews.[31–36]

2.2.1 Intercalation Cathodes

Intercalation materials have skeleton structures that are weakly perturbed upon the incorporation of metal-ions. Intercalation materials typically have small M^{n+}:host stoichiometries (usually in the range from 1:1 to 2:1) and undergo small volume changes during metal-ion incorporation. The prototypical intercalation materials, transition-metal oxides (TMOs), operate according to the following charge/discharge reaction:

$$TMO_2 + xLi^+ + xe^- \rightleftharpoons Li_xTMO_2 \tag{2.1}$$

where TM is a transition metal (Mn, Ni, Co, etc.) and x is in the range $0 < x < 1$ in the case of a monovalent cation (e.g., Li^+). For intercalation materials, the structural changes brought about by metal-ion incorporation are often reversible, leading to high Coulombic efficiencies and good cycle stability of the mass-normalized specific capacity. Layered TMOs having the general formula $LiMO_2$, where M = Ni, Co, and Mn, have been extensively studied. Nonstoichiometric versions containing all three metals - so-called NCM cathodes - have received particular interest.

2.3 Anode Materials

Today's rechargeable LIBs were developed after early batteries with metallic lithium anodes were plagued by the growth of lithium dendrites, leading to overpressurization and fires.[37] Upon realization that lithium could intercalate into graphite and remain ionized (as Li^+) with the graphite lattice accepting an electron for charge balance (LiC_6), the term "lithium-ion battery" was coined and marketed by Sony in 1991.[38,39] Graphite remains the most widely

18

used anode material in commercial LIBs, possessing a theoretical specific capacity of 372 mAhg^{-1}. Although graphite's capacity is not the most limiting factor in commercial systems, significant research has nonetheless been devoted to the development of nanostructured, high-capacity anode materials to improve the capacity and safety of graphite anodes.[22–24,26]

2.3.1 Intercalation Anodes

Although graphite is currently the anode of choice for most applications, LIBs operating in Li salt/organic liquid electrolytes suffer from the consumption of the Li$^+$ (e.g., from the cathode and electrolyte) in the formation of the SEI similar to those for metallic lithium anodes, discussed above. Most of the SEI formation occurs on the first cycle and typically results in an irreversible capacity loss (ICL) of about 10% for graphite anodes. With repeated cycling, the SEI grows in thickness as more Li$^+$ is incorporated into the layers; this film is electronically insulating and hinders Li$^+$ intercalation kinetics, thereby limiting the achievable energy and power density of LIBs employing graphite anodes. Furthermore, the SEI layers become unstable during cycling due to the expansion and contraction of the graphite lattice during lithiation and delithiation. The loss of Li$^+$ from the electrolyte due to continual rearrangement of the SEI layer and constant electrolyte reduction on the graphite surface is one of the main battery degradation mechanisms in commercial LIBs.[40–42]

Although the SEI composition is highly dynamic, HF and LiF are prevalent as decomposition productions from fluorinated Li salts (e.g., LiPF$_6$, LiAsF$_6$, LiBF$_4$) reacting with trace amounts of water in the electrolyte. Decomposition of alkyl carbonate solvents also leads to incorporation of Li$_2$CO$_3$, Li alkyl carbonates, Li$_2$O, and polymeric species derived from the trans-esterification reactions.[40–42] The SEI composition is directly influenced by the electrolyte formulation and, thus, a large set of electrolytes employing various Li$^+$ salts and solvent combinations have been studied in LIBs.[41–44] This complexity is illustrated in Figure

2.2 for propylene carbonate (PC; Figure 2.2b) and ethylene carbonate (EC; Figure 2.2c) electrolytes at different voltages vs Li/Li$^+$. Propylene carbonate intercalation leads to exfoliation and destruction of the graphite lattice, and thus despite its high permittivity, does not find utility in most graphite-based LIBs.
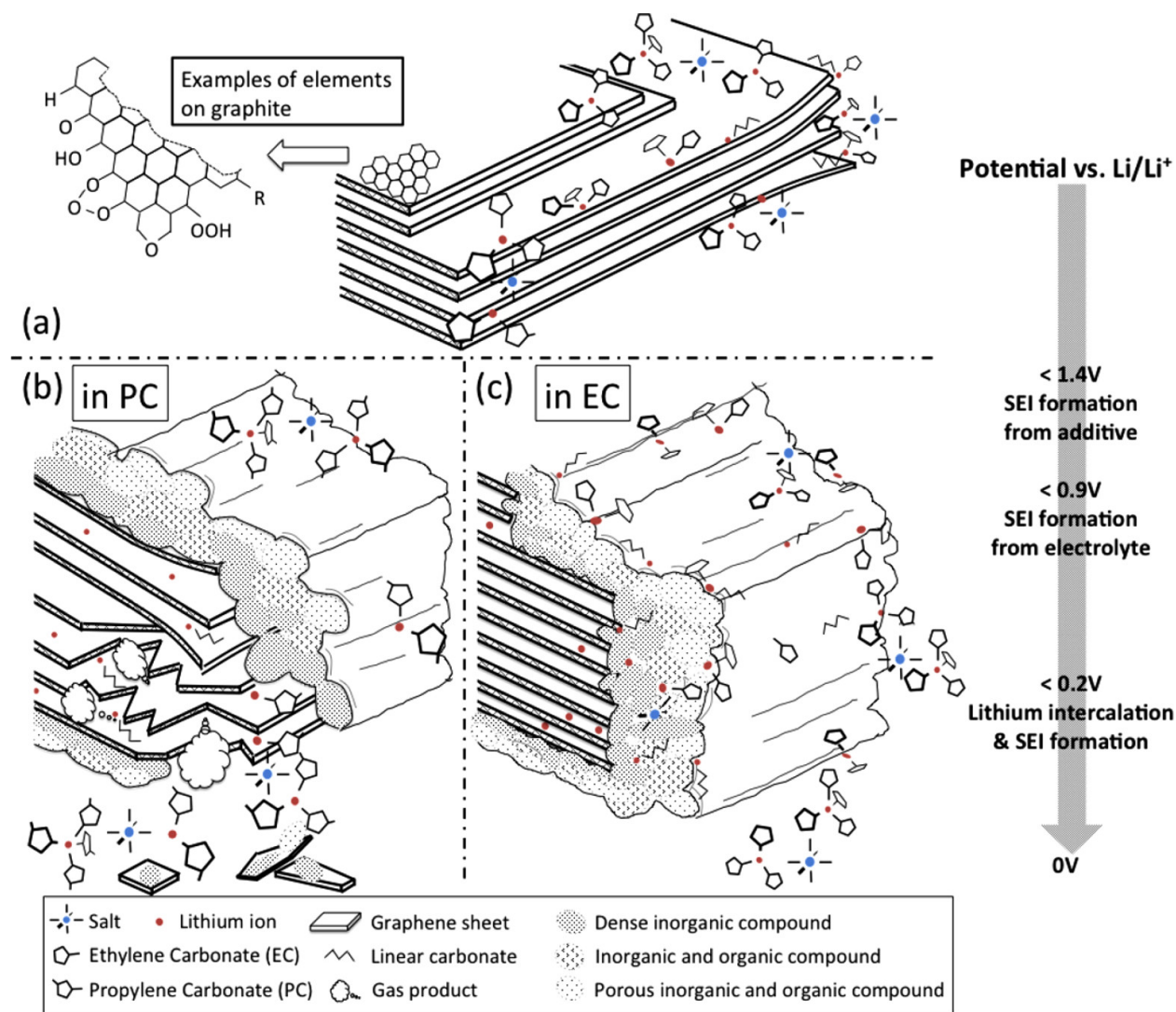
Figure 2.2: Schematic of the anode solid electrolyte interphase (SEI) formation process showing (a) graphene layers surrounded by electrolyte salts and solvents above 1.4 V vs Li/Li$^+$, (b) propylene carbonate (PC) intercalation with lithium-ions into graphene layers resulting exfoliations below 0.9 V vs Li/Li$^+$ and (c) stable SEI formation in ethylene carbonate (EC)-based electrolyte below 0.9 V vs Li/Li$^+$; plane side with thinner SEI and edge side with thicker SEI. Reproduced with permission from ref (41).[41] Copyright 2016 Elsevier.

A combination of the alkyl carbonate solvents (e.g., EC, DEC, DMC, EMC, etc.) with a LiPF$_6$ salt is currently the standard electrolyte in industry, as it offers wide electrochemical stability between $\sim$1.5 - 4.5 V vs Li/Li$^+$ and high ambient-temperature ionic conductivity ($\sim$10^{-2} S/cm). However, the inherent flammability and toxicity due to production of HF has spurred interest into finding Li$^+$ salts with high stability and conductivity. For example, lithium bis(trifluoromethansulfonyl)imide (LiTFSI) has received interest due to its extremely high thermal stability (no degradation until $\sim$360°C) and high ambient-temperature ionic conductivity (9.0 mS/cm in EC/DMC). Concentrated solutions of LiTFSI in 1,3-dioxolane (DOL) or dimethoxyethane (DME) improve reversibility of Li insertion/deinsertion into the graphite lattice. However, the utility of LiTFSI is hindered by its corrosive reaction with Al foil, which is typically used as the cathode current collector in LIBs. Thus, no proposed Li salt has yet exceeded the combined metrics of LiPF$_6$ regarding safety and compatibility, conductivity, thermal stability, and material costs.[41]

To ensure that the ICL due to SEI formation on the graphite anode is minimized in a LIB, assembled cells are typically cycled at slow C rates (0.05C–0.2C) for numerous cycles, which adds processing time and costs to LIB fabrication. Improved SEI homogeneity can be achieved by the addition of compounds that promote faster reduction of the solvent mixture prior to Li$^+$ intercalation and thereby reduce the amount of Li$^+$ consumed by the decomposition reaction on the graphite surface; a variety of additives have been studied to provide this function, including vinylene carbonate (VC), vinyl ethylene carbonate, allyl ethylene carbonate, and vinyl acetate. The most studied electrolyte additive to date is VC and the addition of about 2–3 wt% to mixed-EC/PC solvents promotes faster reduction of the solvent mixture.[45] The alkene functionality in these additives undergoes radical anionic polymerization that can be terminated by solvent molecules and forms an insoluble and stable layer on the graphite surface prior to Li intercalation. These "reductive-type" additives are most critical during the initial steps of SEI formation and they function (1) to reduce the ICL of Li$^+$ in SEI formation; (2) to reduce the amount of gas generation during electrolyte

decomposition on the graphite surface; and (3) to improve the long-term cycle stability of graphite anodes.[45]

Coating the surface of graphite is an effective way to change the surface composition and the resulting SEI that forms.[42] For example, graphene or pyrolytic carbon coatings have been applied to increase the electrical conductivity of the graphite material, conductive polypyrrole or PANI coatings to improve conductivity of the electrode laminate, metal-oxide coatings (e.g., Al_2O_3, ZrO_2) to reduce the graphite/electrolyte contact area,[46] and inorganic coatings such as Li_2CO_3, Na_2CO_3, and K_2CO_3 to promote inorganic-rich SEI.[47] Although these studies have made progress in reducing the initial ICL, few studies have focused on the design of a durable and flexible SEI that minimizes lithium inventory loss during repeated cycling.[42]

Similar to Li-metal anodes that were plagued with safety issues in early rechargeable batteries, graphite anodes are also susceptible to Li plating due to the proximity of its reversible potential with that of Li^+/Li ($\sim$0.1 V vs Li/Li^+; Figure 2.2).[48,49] Li plating onto graphite can be initiated by several factors, including (1) the composition and concentration of the electrolyte (e.g., electrolytes with high contents of EC show higher probability of Li plating); (2) the ratio between the anode and cathode capacities; and (3) when the temperature is low and/or the charge/discharge rate is fast.[42,49,50]

Avoiding Li plating and dendrite formation on graphite anodes is typically achieved by controlling the anode/cathode capacity ratio to be $\sim$1.1.[41,50] This approach reduces the polarization of the anode and mitigates Li electroplating.[42] However, the extra anode material must also undergo SEI passivation and thus increases the cost of the cell and reduces the achievable energy density of the cell and is therefore insufficient for long-term stability and Coulombic efficiency metrics, as Li^+ consumption increases with repeated cycling.[41] The extent of Li plating and dendrite growth is also highly dependent on the degree of disorder in the graphite lattice. As the disorder of the graphite increases, the current distribution

through the electrode becomes heterogeneous, which causes moss-like dendritic growth during Li intercalation. Furthermore, if the particle size distribution is also large, the current becomes more inhomogeneous and dendrite growth intensifies.

Highly ordered graphite remains the leading anode choice in today's commercial LIBs. Unfortunately, LIBs operating in alkyl-carbonate-based electrolytes suffer from electrolyte and Li^+-salt decomposition onto the graphite surface, forming an SEI layer that passivates the graphite. This SEI layer is inherently heterogeneous, leading to cracking and fragmentation of the layer such that further Li^+ and electrolyte repeatedly decompose on the freshly exposed graphite surface; Li^+ consumption due to SEI formation and subsequent Li plating are the major causes of ICL and capacity fade in LIBs.

The search for Li intercalation materials with improved safety metrics and electrochemical stability is motivated by graphite's heterogeneous SEI and Li insertion potential of $\sim$0.1 V, which is close to the lithium electroplating potential. Attractive alternatives, such as lithium titanate (LTO), operate at a higher Li insertion potential than graphite, but well above the reduction potential of common electrolytes so an SEI is not required for stable cycling.[51,52] However, the utility of LTO is limited by its low theoretical specific capacity (175 mAhg^{-1}) and high operating voltage of $\sim$1.5 V (vs Li/Li$^+$) that reduce the energy density of LTO-based LIBs compared to those achievable with graphite anodes. One method to raise the energy density of LTO is to form a composite anode with a high capacity material (e.g., SnO_x, MO) and to extend the voltage window to 0.01–3.0 V vs Li/Li$^+$. Unfortunately, the high-capacity co-anode usually suffers from large volume expansion/contraction with lithium insertion/deinsertion that restricts cyclability and lowering the cutoff voltage below $\sim$0.8 V leads to electrolyte decomposition and formation of a SEI layer on the LTO surface that restricts performance.[53]

Within the oxide family, titanium dioxide (TiO_2) has been one of the most extensively studied materials for energy-storage applications.[54] Theoretically, TiO_2 can accept 1 mol of Li$^+$

($LiTiO_2$) to provide a theoretical specific capacity of 330 mAhg^{-1}. However, significant structural changes and associated large capacity fade have been observed when x > 0.5 in Li_xTiO_2, and thus stable electrochemical cycling has only been observed for TiO_2 anodes when the degree of lithiation is kept low (x < 0.5, reversible capacity $\sim$165 mAhg^{-1}).[55–58] This effect is due to the Li^+ mobility being decreased when x > 0.5 and that further Li^+ insertion could only be achieved in the surface layer of the electrode ($\sim$4 nm). Engineering mesoporous micron-sized secondary particles with nanostructured primary particles is an attractive route to take advantage of the improved reaction kinetics of nanoscale TiO_2, while still achieving suitable tap densities.[56] When cycled between 1.5 and 3.0 V vs Li/Li$^+$, mesoporous TiO_2 materials can deliver specific capacities of 164 mAhg^{-1} at C/2 with good rate capability. However, the improved safety in titanium-based anodes has not been coupled to improved performance over graphite anodes, and the development of higher energy intercalation materials is needed to replace the traditionally used graphite anode.

2.3.2 Niobium Pentoxide

Niobium pentoxide has emerged as a promising high-power anode material, due to its fast lithium intercalation kinetics.[59] The Li^+ intercalation reaction is understood as

$$Nb_2O_5 + xLi^+ + xe^- \rightleftharpoons Li_xNb_2O_5 \qquad (2.2)$$

where x ranges from 1.6 to 2.0, resulting in a theoretical capacity of 202 mAhg^{-1}.[60] Early contributions from Goodenough, Dunn, and others demonstrated energy densities of up to 30 Whkg^{-1} at high power densities of more than 1000 Wkg^{-1}.[16,61–63] Subsequent studies on the lithiation mechanism revealed that the majority of the capacity observed can be attributed to an intercalation process, but the rapid kinetics of intercalation was characteristic of pseudocapacitance.[8,11] Orthorhombic and monoclinic Nb_2O_5 consists of edge-sharing

NbO_6 octahedra, which creates pathways for Li^+ intercalation with low energy barrier for solid-state diffusion.[8,64] Simon and co-workers used *in-situ* XRD to probe the Li^+ intercalation pathway in a 40 μm thick orthorhombic Nb_2O_5 (T-Nb_2O_5) film.[65] They showed reversible expansion and contraction in the d-spacing for (001), (180), and (181) planes during lithiation-delithiation cycles. No change in the crystal phase was observed during cycling, and they were able to cycle the active material for 1000 cycles without any loss in capacity, at 3000 Wkh^{-1}.[65]

Composite Nb_2O_5 architectures formed with a conductive matrix/support has been successfully employed to enhance the performance of Nb_2O_5. For example, immobilization of T-Nb_2O_5 particles on two-dimensional niobium carbide sheets (MXenes) increased the gravimetric capacity to 150 $mAhg^{-1}$ with cycle stability of up to 2000 cycles,[66] whereas Nb_2O_5@ carbon core-shell microspheres demonstrated a capacitance of 140 $mAhg^{-1}$ at high current densities of up to 50 Ag^{-1}.[67] Lim et al. were able to outperform the preceding devices by designing a mesoporous Nb_2O_5/carbon nanocomposite that cycled stably for 4000 cycles at 2 Ag^{-1} while delivering a capacity of more than 100 $mAhg^{-1}$.[68] They attributed the high-rate performance and cycle stability to the uniformly carbon-coated mesoporous template providing surface stability and electronic conductivity to the insulating Nb_2O_5. In pursuit of higher energy density Nb_2O_5 devices, Jha and co-workers recently demonstrated a strategy of preparing mesoporous T-Nb_2O_5 nanoscopic films that delivered superior energy densities of 486 $Whkg^{-1}$ (220 $mAhg^{-1}$) at a power density of 90 $kWkg^{-1}$ (50 Ag^{-1}) (Figure 2.3).[12] Electrophoretic deposition of NbO_x nanoparticles onto fluorine-doped tin oxide (FTO) at significantly negative potential leads to migration of nanoparticles toward the current collector surface while simultaneously evolving hydrogen gas that creates nanobubbles in the deposited film. Upon annealing in air, the T-Nb_2O_5 deposited has a highly porous morphology and has intimate contact with the current collector without the requirement of conductive binders. The porous morphology enhanced the pseudocapacitive contribution to the charge storage and increased the specific capacity to above the theoretical capacity of

Nb_2O_5 at rates of up to 50 Ag^{-1}.[12] However, significant capacity fade was observed over 500 cycles during galvanostatic charge-discharge tests (10 Ag^{-1}), and further characterization of the mesoporous T-Nb_2O_5 nanoscopic films is required to probe the degradation pathways with repeated cycling. Overall, the rapid Li^+ storage kinetics and cycle stability of Nb_2O_5 make it an attractive candidate for future applications that desire fast charge/discharge rates.
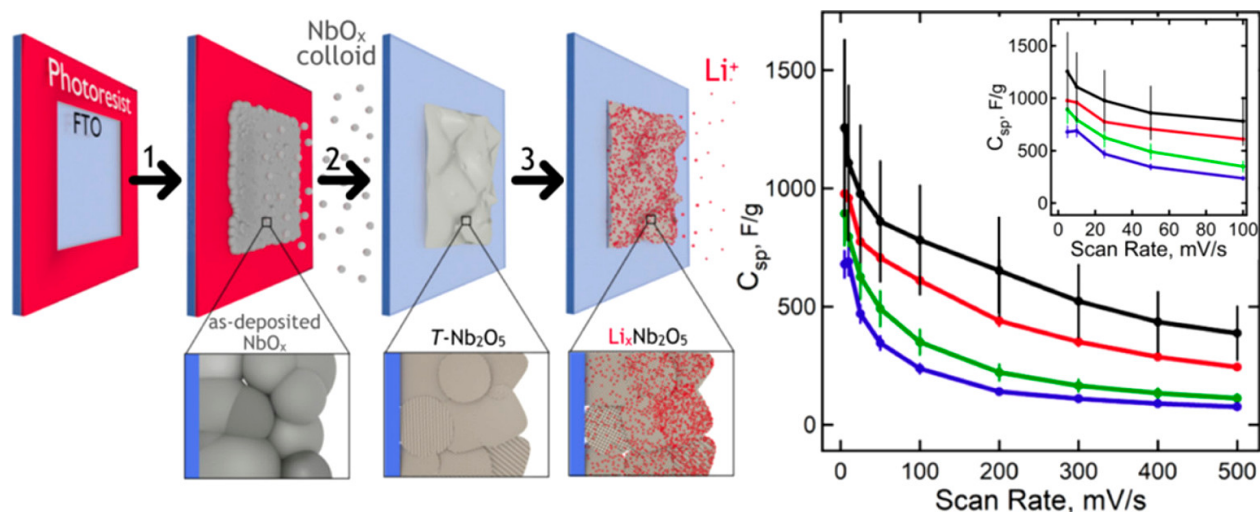
Figure 2.3: Summary of T-Nb_2O_5 Electrophoretic Deposition and Resulting Electrochemical Measurements. (Step 1) Electrophoretic deposition of NbO_x colloids onto fluorine-doped tin oxide (FTO) under constant hydrogen evolution. (Step 2) Amorphous film heated to 550°C for 5 h, creating orthorhombic Nb_2O_5 (T-Nb_2O_5). (Step 3) Lithiation via intercalation pseudocapacitance in porous film leads to high energy density. Reproduced from ref (12).[12] Copyright 2018 American Chemical Society.

2.4 Mechanisms of Degradation and Mitigation for TMO Electrodes

More is known about TMOs than about conversion materials in terms of degradation and failure mechanisms and the spectrum of processes leading to irreversible capacity loss.[69] These issues include degradation of binder particles, loss of conductive contact between cathode

particles, dissolution of cathode particles, the reprecipitation of undesirable phases, disordering, cracking and fracture, the formation of surface layers, and electrolyte decomposition. In the common battery electrolyte LiPF$_6$, decomposition leads to the production of corrosive HF according to[70]

$$LiPF_6 \rightleftharpoons LiF(s) + PF_5 \tag{2.3}$$

$$H_2O + PF_5 \rightleftharpoons POF_3 + 2HF \tag{2.4}$$

Strategies that mitigate the formation of acidic species have been successful in increasing the cycle stability of the cathodes. Coatings that inhibit the dissolution and structural transformations of the active material have been the subject of numerous reports. Other strategies that help to mitigate structural degradation are the judicious selection of synthetic protocols to achieve nanostructures that are inherently less prone to degradation during lithiation/delithiation. This approach focuses on synthesizing structures that are better able to accommodate the lattice strain resulting from repeated insertion/deinsertion of lithium cations. The use of nanoparticles with conductive coatings has been effective in enhancing the performance of the typically insulating intercalation materials, but care must be taken to ensure that feasible mass loadings are achievable with these materials if they are eventually to be included in commercial devices.

2.5   Emerging Tools for Assessing Degradation

The advances in electrode materials and design have undoubtedly benefited from the development of characterization techniques that now enable wholistic understanding of electrode materials at the nanoscale and below to their behavior in a practical device. Here, we highlight the emerging tools for studying battery electrode degradation and provide an overview of the information that can be obtained from a variety of physiochemical methods. We

particularly highlight *in-situ* and *operando* techniques that provide valuable mechanistic information on the system under real conditions.

2.5.1   Diffraction

X-ray diffraction is being applied to problems in energy storage with great efficacy because *operando* XRD data can be acquired on entire batteries and has been applied to studying the phase transitions of a variety of cathode materials).[71–74] Jenson et al. combined X-ray diffraction with tomography (XRD-CT) to probe the structure and composition of commercial AAA nickel metal hydride cells.[75]

Neutron diffraction has greater sensitivity to the atomic parameters of lithium and offers higher contrast with neighboring elements including Mn and Fe. As probes of the structure and dynamics of lithium-ion batteries, neutrons have several advantages over X-rays. In the case of lithium, isotopic enrichment with ^{7}Li provides a strategy for highlighting the naturally abundant ^{6}Li, which has a much higher absorption cross-section (60×10^{-24} cm^2 at 1.54 Å, relative to ^{7}Li with 0.039×10^{-24} cm^2). Neutrons also possess tremendous penetration depth that is sufficient for imaging entire batteries.[76,77]

2.5.2   Microscopy

Vigorous development of TEM has opened up new capabilities since the pioneering work involving the assembly of operating batteries.[78–82] In these experiments, processes associated with charging and discharging electrodes could be observed across many length scales, down to atomic dimensions, in real time. This work launched *operando* and *in-situ* TEM as a potent new tool for the investigation of battery and capacitor electrodes. Two experimental strategies for conducting these experiments have been employed. The first uses an "open"

cell that consists of a nanometer-scale electrode immersed on one end with a vacuum compatible electrolyte containing a reference electrode material (e.g., Li^0). The second strategy is to contain both electrodes within an electrochemical cell that incorporates an ultrathin electrolyte layer and (optionally) a third, reference electrode enabling potential control.

Although the focus in this area has been on the degradation of nanoscopic anodes and cathodes, electrolyte degradation has also been investigated in some recent *in-situ* TEM experiments.[82] Not surprisingly, *in-situ* TEM has also been used to investigate SEI layer formation.[83,84]

X-ray-based probes make possible the nondestructive analysis of battery and capacitor electrodes in operating cells. X-ray microscopy, recently reviewed,[85] provides an emerging set of tools for resolving the elemental composition of materials in real space. Two modes of operation can be distinguished. Full-field X-ray microscopy involves illuminating a micron-scale spot on a sample and imaging the transmitted photons onto a position-sensitive detector, in analogy to conventional TEM. The second approach, called scanning probe mode, operates by raster scanning a prefocused X-ray beam across a sample and analyzing the transmission of this beam, in analogy to scanning transmission electron microscopy (STEM). In both modes, control of the X-ray photon energy provides elemental contrast in the resulting images.[85] Coherent X-ray diffraction imaging (CXDI) has been used to map the local three-dimensional strain inhomogeneity of individual cathode nanoparticles.[86,87]

Transmission X-ray microscopy (TXM) can address the issue of degradation and failure with in *operando* NPD and investigate capacity fade in Li_2MnO_3.[77] Together, these two techniques provide detailed real-space pictures of the compositional changes that are occurring during the charging of this cathode, involving contraction of its volume and the formation of micron-scale cracks, followed by discharge and the healing of some cracks during discharge and Li insertion. These results reveal that capacity fade in this complex system occurs as a consequence of the phase lattice change coupled with phase separation.[77]

Electrochemical strain microscopy is a form of scanning probe microscopy for investigating the transport of ions at the surface of materials. It has been used to probe Li^+ transport at $LiMn_2O_4$ surfaces where it was discovered that the diffusion coefficient for Li^+ was reduced by approximately an order of magnitude in $LiMn_2O_4$ samples that were "aged" by cycling relative to fresh particles of the same material.[88]

Figure 2.4 provides an overview of common techniques used to characterize battery electrodes. The rapid development of advanced characterization techniques has been of great value to current battery research, enabling the study of materials from the atomistic scale (Figure 2.4)[89] to their bulk properties (Figure 2.4b)[90] and behavior at the device scale (Figure 2.4c).[91] The new insights obtained from the suite of techniques listed in Figure 2.4 have contributed to the mechanistic understanding of battery degradation that have, and will continue to guide, future innovation in cell design and material optimization.[92]

Å – nm	>10 nm – 100 µm	mm – cm

Detail
Surfaces and interfaces

Features
- SEI/CEI composition
- surface chemistry
- topology

Techniques
Surface-sensitive techniques, depth-profiling
- STEM
- TEM
- AFM
- XPS
- TOF-SIMS

Detail
Bulk materials

Features
- Electronic/crystal structure
- morphology
- thermal stability

Techniques
Bulk techniques
ex situ and *in situ*
- SEM
- XRD
- Raman
- TGA
- EPMA

Detail
Electrodes

Features
- Cycling behavior
- electrode design
- reaction mechanisms

Techniques
Imaging and mapping techniques
- Optical microscopy
- NPD
- XRD-CT
- TXM
- OEMS

Figure 2.4: Overview and representative examples of techniques used characterize battery electrodes ranging from the angstrom scale to the centimeter scale and beyond. (a) High-angle annular dark-field (HAADF) scanning tunneling electron microscopy (STEM) image of a lithium- and manganese-rich transition-metal oxide (LMR). Reproduced with permission from ref (89).[89] Copyright 2018 Royal Society of Chemistry. (b) Scanning electron microscopy (SEM) image of nanorod gradient $Li[Ni_0.81Co_0.06Mn_0.13]O_2$ cathode particles. Reproduced from ref (90).[90] Copyright 2019 American Chemical Society. (c) 3D rendering of jelly roll assembly inside a LIB pouch cell using synchrotron X-ray computed tomography (CT). The heat mat denotes the X-ray adsorption value of the material. Reproduced from ref (91).[91] Copyright 2017 The Electrochemical Society.

2.6   Conclusions and Outlook

The last six years have seen significant advances at both the anode and cathode sides of secondary metal-ion battery systems. It is important to recognize that powering this science and engineering has been a focused effort by the Department of Energy and other agencies around the world to fund this work. The result has been a flurry of new science and the entry of many scientists into the energy science space, culminating in the emergence of truly transformational technologies with the potential to increase the capacity of batteries by factors of two or more.

The application of advanced characterization techniques spanning orders of magnitude in dimensional resolution (i.e. subnanometer to centimeter) has greatly benefit the development of battery science (see examples in Figure 2.4). In particular, the burgeoning development of *in-situ* and *operando* techniques has enabled deeper understanding of the degradation mechanisms plaguing promising electrode materials and has inspired a plethora of strategies to mitigate electrode degradation, enhance cycle life, and/or improve safety of rechargeable metal-ion batteries (Figure 2.5). Some approaches, such as the addition of strategic electrolyte additives (Figure 2.5a) and the use of protective coatings on the electrode material surface (Figure 2.5b), have already been implemented in commercial lithium-ion cells, whereas synthetic optimization to produce compositionally graded (Figure 2.5c) or shape-controlled materials to expose favorable reactive facets (Figure 2.5d) are emerging as promising strategies to boost energy density and increase rate capability of future rechargeable batteries.[25,28,92]

The significant volume changes, material dissolution, and inadequate energy efficiencies associated with developing high capacity battery chemistries have motivated efforts toward developing conductive composites (Figure 2.5e) and/or 3D architectures (Figure 2.5f) to combat these limitations. Although small-scale demonstrations show great promise for un-

locking higher energy density batteries, transitioning the fundamental advances to commercial use remains a tremendous technological challenge, as the demanding requirements for future applications (e.g., electric vehicles) dictate that the mass loadings of active materials must be increased at both the anode and cathode, coupled with increased utilization of these active materials within the cell. These requirements are often disregarded in small-scale demonstrations employing low tap density nanomaterials with low mass loading during testing.

The pressure for further improvements in material design, characterization techniques, and cell design is certain to build, driven by the significant expansion in the number of manufacturers marketing electric vehicles, already in progress in 2019, that will demand better battery technology in the short term. The continued innovation and interplay between materials science and advanced characterization techniques is necessary to transition fundamental advances to commercial use. As demand for lithium-ion batteries inevitably increases, the associated increased cost of lithium and cobalt will continue to heighten interest in Na^+, K^+, Mg^{2+}, and other ions that are obtainable for lower cost. Surely, there has never been a more exciting time to be engaged in research in electrical energy storage.
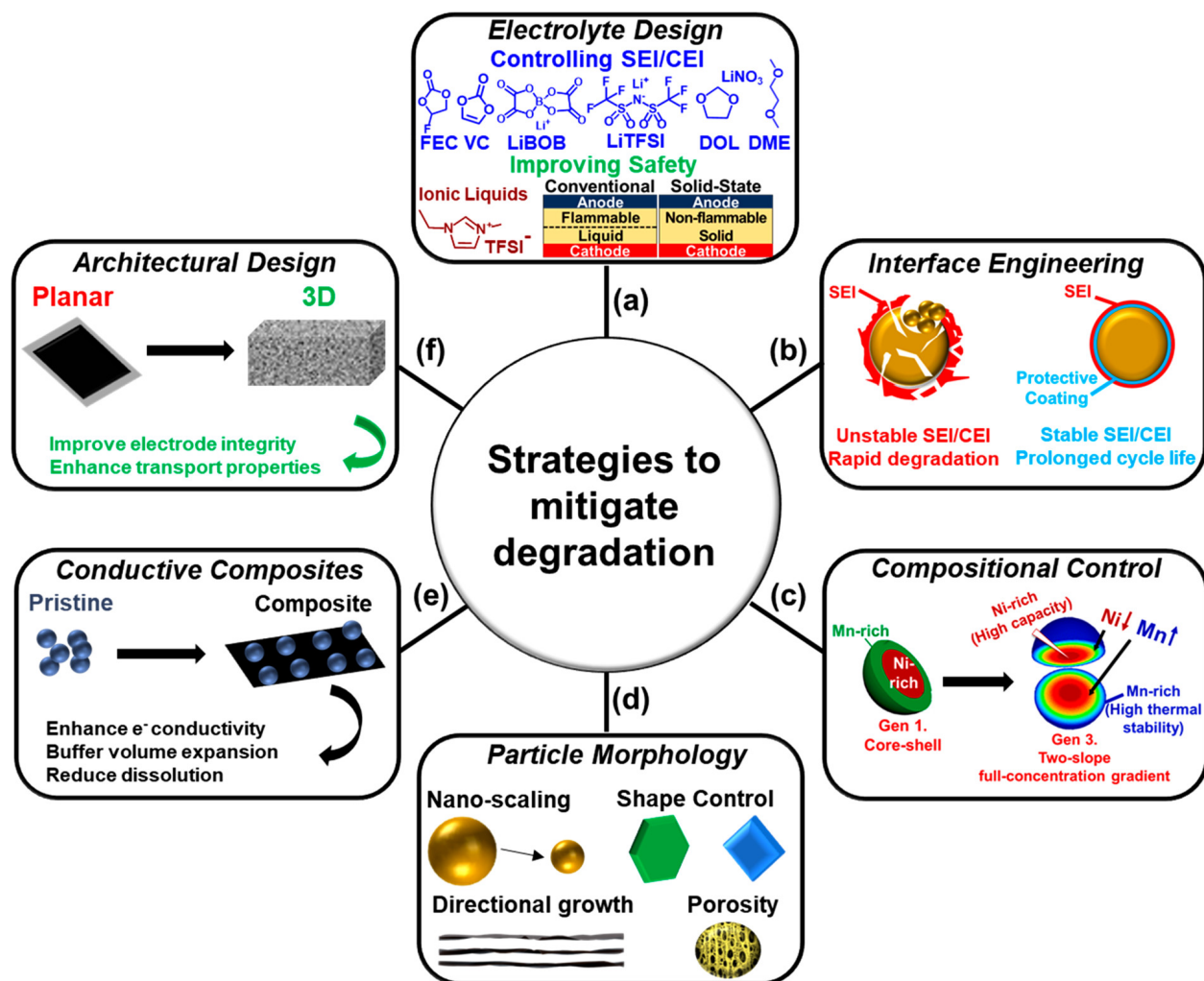
Figure 2.5: Overview of notable strategies used to mitigate degradation of metal-ion battery electrodes, including (a) designing electrolytes for enhanced SEI/CEI formation, cycle stability, (b) interface engineering with protective coatings to prevent breakdown of active-material particles during cycling, (c) composition control of the electrode particles, (d) synthetic optimization to control particle morphology, (e) the use of composites made from conductive scaffolds and active materials. (f) designing new electrode architectures to overcome volume changes and enhance transport properties. Image used in (c) adapted from ref (28).[28] Copyright 2016 American Chemical Society.

Chapter 3

Investigating the Degradation of Nb$_2$O$_5$ Thin Films Across 10,000 Lithiation/Delithiation Cycles

3.1 Introduction

Transition metal oxides (TMOs) gradually lose their ability to reversibly intercalate/ deintercalate metal ions (e.g., Li$^+$) after 500-1000 cycles. When TMOs are used as battery cathodes, this process causes irreversible capacity loss for the battery, necessitating its replacement. The degradation and failure mechanisms responsible for capacity loss are complex, and commonly include three measurable changes:[93–97] 1) a loss of TMO crystallinity, 2) slowed ion intercalation/deintercalation and ion transport within the TMO, and 3) diminished electronic conductivity. In the cathodes of metal ion batteries, TMOs are mixed with conductive fillers to enhance electronic conductivity and binders to promote cohesion of the TMO layer. Mechanisms of degradation operating in such composite films are likely to

involve these fillers and binders.[93–97] Since real battery electrodes contain these components, their participation in degradation is important to understand, but the complexity of these mutlicomponent systems with respect to degradation can be daunting.

In this study of degradation focusing on orthorhombic niobium (V) oxide (T-Nb_2O_5),[8,13,14,16,98–106] we simplify this problem in two ways. First, all binders and fillers are eliminated, insuring that degradation pathways involving these extrinsic materials are removed. Second, electrophoretic deposition (EPD),[12] is used for synthesizing thin films of T-Nb_2O_5 films. We have recently reported[12] that EPD provides an unusually reproducible method for synthesizing thin films of T-Nb_2O_5. The use of many quasi-identical T-Nb_2O_5 films provides a means for studying the evolution of structure and composition during the degradation process using tools including cyclic voltammetry (CV), high-resolution transmission electron microscopy (HR-TEM), x-ray diffraction (XRD), scanning electron microscopy (SEM) coupled with energy dispersive x-ray (fluorescence elemental) spectroscopy (EDS), electrochemical impedance spectroscopy (EIS), Raman microprobe spectroscopy, and x-ray photoelectron spectroscopy (XPS).

T-Nb_2O_5 is an interesting candidate TMO for this study because the orthorhombic polymorph shows unusually rapid Li^+ diffusion and intercalation/deintercalation kinetics:.[8,11,13,15,16,65,104,107,108]

$$Nb_2O_5 + xLi^+ + xe^- \rightleftharpoons Li_xNb_2O_5 \tag{3.1}$$

It also has a relatively high theoretical specific capacity, C_{sp}, of 202 mAh/g or 403 F/g for the 1.8 V voltage window used in this study. These values corresponding to $x = 2$ in Equation (1).[60]

T- Nb_2O_5 films of 60 ($\pm$ 20) nm thickness were prepared from colloidal suspensions of NbO_x
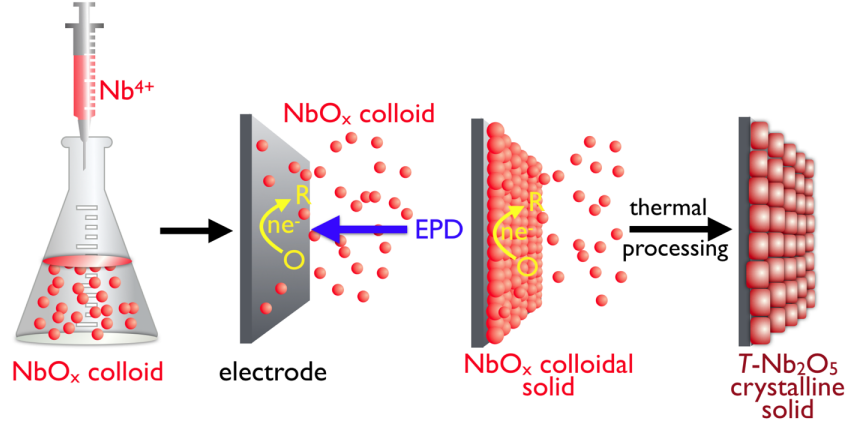
Figure 3.1: Schematic diagram of electrophoretic deposition of NbO_x and subsequent processing to obtain T-Nb_2O_5.

using a two step process involving electrophoretic deposition (EPD) and calcination (Figure 3.1).[12] The reproducibility of these films in terms of their electrochemical response, and the trajectory of the specific capacity over many lithiation/delithiation cycles, is very good. For example, during repetitive potentiostatic cycling of these films at 200 mV/s, the specific capacity, C_{sp}, fades by ∼30% from 400 F/g to 280 F/g after 2000 cycles.[12] Film to film dispersion of the C_{sp} is less than 15% from 0 to 10,000 cycles, providing the opportunity for *ex-situ* investigation of film structure (XRD, TEM, SEM), chemical composition (EDS, XPS), local bonding environments (Raman spectroscopy), and electrochemical metrics (*via in-situ* EIS). The focus of this study are the mechanisms responsible for the degradation causing this irreversible capacity loss.

3.2 Experimental Methods

3.2.1 Chemicals and Materials

Niobium pentachloride (NbCl$_5$, 99%), hydrogen peroxide solution (H$_2$O$_2$, 30% (w/w) in H$_2$O), lithium perchlorate (LiClO$_4$, battery grade, dry, 99.99% trace metal basis), propylene carbonate (anhydrous, 99.7%) and fluorine doped tin oxide (FTO) coated glass slides (surface resistivity $\sim$13 Ω/sq) were all used as received from Sigma-Aldrich. FTO was cleaned using a commercial cleaning solution, Hellmanex 3, obtained from Hellma Analytics. Positive photoresist (Shipley S1808) and developer (Shipley MF-319) were purchased from Kayaku Advanced Materials. Acetone and methanol (ACS certified grade) were used as received from Fisher Scientific.

3.2.2 Electrophoretic Deposition of T-Nb$_2$O$_5$

Electrophoretic deposition of T-Nb$_2$O$_5$ films on FTO was carried out as previously described.[12] Briefly, a modification of the method of Zhitomirsky[19] was used in which a clear, colloidal NbO$_x$ solution was first prepared by rapidly injecting Nb^{5+} in methanol (135 mg NbCl$_5$ dissolved in 4 mL methanol) into cold ($\sim$2°C) hydrogen peroxide. After aging at room temperature for 3 hours, EPD was carried out potentiostatically on a 6 $\times$ 6 mm FTO electrode with area 0.36 cm^2 in two electrode mode at -2.0 V. Under these conditions, a quasi-constant deposition current was measured and EPD was continued until a total Coulombic loading of 1.4 C/cm^2 was obtained - approximately 190 s. T-Nb$_2$O$_5$ films 60 nm in thickness were then obtained by calcination at 600°C for 8 hours.

3.2.3 Electrochemical Characterization

All electrochemical measurements were performed by a one-compartment three-electrode cell using a Gamry Series G 300 potentiostat. Cyclic voltammetry was conducted in 1.0 M LiClO$_4$ (battery grade, dry, 99.99%) in dry propylene carbonate inside a N$_2$ glovebox. Glassy carbon rod (2 mm diameter) was used as counter electrode with a Platinum wire pseudo-reference electrode for the electrochemical measurements. EIS measurements were conducted from 1 Hz to 30 kHz using an amplitude of 10 mV. All potentials are referenced to the Li/Li$^+$ couple, E_{Li/Li^+} = -3.045 V versus normal hydrogen electrode[109] by calibrating the Pt pseudo-reference electrode against Li/Li$^+$ using ferrocene/ferrocenium (Fc/Fc$^{+\cdot}$) in 1.0 M LiClO$_4$, PC.[110]

3.2.4 Structural Characterization

Scanning electron micrographs (SEMs) and energy dispersive x-ray spectroscopy (EDS) were acquired using a FEI Magellan 400 XHR system equipped with an Oxford Instruments EDS detector (80 mm^2, AZtec software). Before imaging, samples were sputter-coated with ~5 nm of iridium. Accelerating voltages of incident electron beams ranged from 10 kV to 30 kV and probe currents ranged from 25 pA to 0.4 nA. All SEM specimens were mounted on stainless stubs and held by carbon tape. X-ray photoelectron spectroscopy (XPS) was measured using the AXIS Supra by Kratos Analytical Inc. equipped with a monochromatic Al/Ag x-ray source. Raman spectra were obtained using a customized Renishaw InVia Raman microscope with a 532 nm excitation laser with a 2 μm spot size. Raman transitions were fit to Gaussians to extract peak positions and the full width half maxima (FWHM). Grazing incidence x-ray diffraction (GIXRD) patterns were collected using a Rigaku Smartlab X-ray diffractometer in parallel beam geometry with a fixed incident angle of 0.3°. The Cu Kα x-ray generator was operated at 40 kV and 44 mA. Transmission electron microscopy (TEM)

was performed on a JEOL JEM 2800 transmission electron microscope equipped with a 200 kV Schottky field-emission electron gun. High resolution TEM images were recorded at a resolution of 0.2 nm. Fast Fourier Transforms were taken from selected areas in the high resolution TEM images.

3.3   Results and Discussion

3.3.1   *ex-situ* TEM Analysis of Degrading T-Nb$_2$O$_5$ Films

T-Nb$_2$O$_5$ films were cycled voltammetrically between 1.3 V and 3.1 V *vs* Li/Li$^+$ at 200 mV/s for 10,000 cycles (Figure 3.2a). Even at this rapid charge/discharge rate, corresponding to a C-rate exceeding 400, the voltammetry of fresh films is characterized by a reversible cathodic lithiation peak at 1.57 V, and an anodic delithiation peak at 1.75 V - as previously observed for Nb$_2$O$_5$ films,[8,11,65,104] and nanostructures.[98–100,102]

Fresh T-Nb$_2$O$_5$ films produce C$_{sp}$ values of 360 - 420 F/g (Figure 3.2b) - approaching the theoretical maximum value of 403 F/g. Beyond 1000 cycles, C$_{sp}$ smoothly decreases by 50% to 200 F/g at 10,000 cycles (Figure 3.2b). The reproducibility of these cycle stability curves is excellent, as evidenced by the error bars that show $\pm 1\sigma$ for up to twelve different films. This cycle stability equals or exceeds that reported for Nb$_2$O$_5$ in previous studies.[8,15,65,104,108,111] This suggests that some degradation channels are eliminated by the omission of conductive fillers and binders, and possibly by the nanoscopic dimensionality of these films in terms of thickness. Understanding the origins of this irreversible capacity loss is the goal of this paper.

The evolution of crystallinity and crystal structure of T-Nb$_2$O$_5$ films were tracked by *ex-situ* TEM during the degradation process by halting the cycling of films and preparing cross-
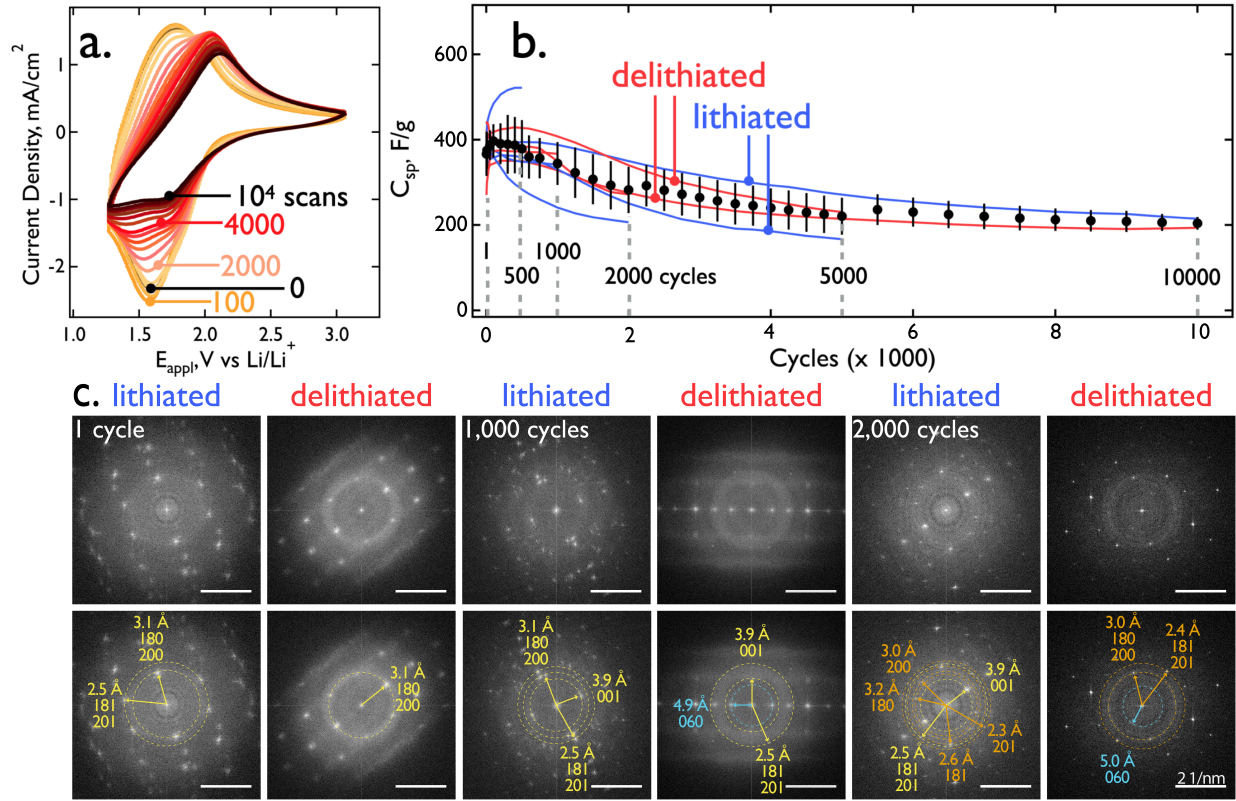
Figure 3.2: Electrochemical and *ex-situ* TEM analysis of T-Nb_2O_5 films. a) Voltammetric cycling of a 60 nm T-Nb_2O_5 film at 200 mV/s in 1.0 M $LiClO_4$/PC showing a loss of capacity coupled with a positive shift in the reversible potential by 100 - 200 mV across 10,000 scans. b) Twelve plots, for twelve T-Nb_2O_5 films, of the reversible capacity, C_{sp} *versus* the number of lithiation/delithiation cycles. Data points (black) are average C_{sp} values with $\pm 1\ \sigma$ error bar. Blue and red data were used to acquire TEM data for lithiated and delithiated films, respectively. c) Raw FFTs of atomic resolution TEM images (top) are paired with assignments (bottom) for lithiated and delithiated films at 1, 1000, and 2000 cycles. Changes in the major three lithiation planes, 001 (3.9 Å), 180/200 (3.1 Å) and 181/201 (2.5 Å), are tracked. Yellow indices represent the periodicities corresponding to literature T-Nb_2O_5 d-spacings. Orange indices correspond to distortions of literature d-spacings either due to lithiation (increase in d-spacing) or damage to the crystal integrity (decrease in d-spacing). Blue indices track the appearance of a 060 (4.9 Å) family of planes which have not been show to contribute to lithiation in T-Nb_2O_5.

41

sectional specimens for TEM analysis. Twelve T-Nb_2O_5 films, corresponding to the twelve C_{sp} *versus* cycles data sets shown in Figure 3.2b, were used for the preparation of the samples studied by TEM. Black data points and error bars are mean values and standard deviations for C_{sp}, showing the reproducibility of the electrochemical energy storage properties of these films. Cross-sectional TEM studies were also conducted on thin films after 0, 1, 1000, 2000, 5000, and 10,000 voltammetric lithiation/delithiation cycles (Figure 3.2c, Figure 3.3). TEM data for 5000 cycles films is omitted here because these films were indistinguishable from 2000 cycle samples. Two samples were examined at each of these junctures corresponding to the lithiated (1.3 V *vs* E_{Li/Li^+}) and delithiated (3.1 V *vs* E_{Li/Li^+}) states, as indicated.

The niobium sub lattice can be seen in HR-TEM images of as-prepared films (Figure 3.3a, top). However, the crystallinity and structure of this material is more readily determined by evaluating Fast Fourier Transforms (FFTs) of the real-space TEM images, as shown in Figure 3.3a (bottom). In the bottom image of Figure 3.3a, the FFT shows prominent peaks produced by the 001, 180/200, and 181/201 periodicities present in the TEM image. At higher magnification (Figure 3.3a, top inset), (001) and (180/200) planes of Nb atoms are resolved. In contrast, after 10,000 cycles, no evidence of crystalline structure is observed in either real space or FFTs of the HR-TEM images (Figure 3.3b). The integrity of the orthorhombic lattice is more easily evaluated from FFTs of the real space TEM data, and FFTs are analyzed exclusively below.
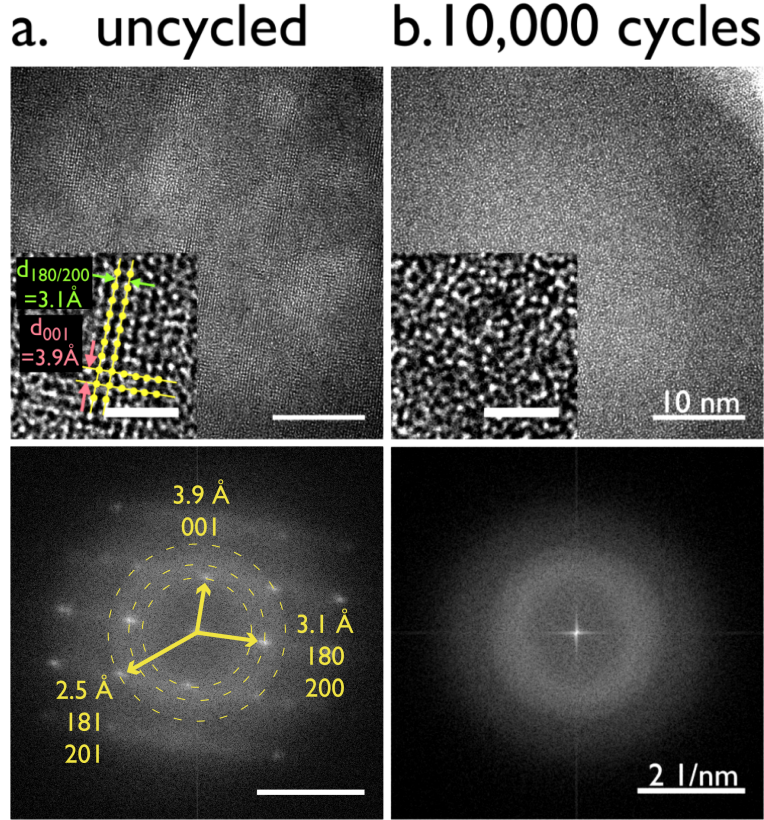
Figure 3.3: Real space and Fourier transformed TEM images. (a,b) TEM images shown in real space (top) and after the application of a Fast Fourier Transform (FFT, bottom) for (a) a freshly prepared, uncycled T-Nb_2O_5 film and (b) a film cycled 10,000 times. a). The inset shows the niobium sub lattice at higher magnification. b) A T-Nb_2O_5 film cycled 10,000 times at 200 mV/s is completely amorphous. FFTs of these images show no prominent reflections, and no atomic order is seen at higher magnification (inset). The distance bar for the inset images is 2 nm.

3.3.2 Correlation of Specific Capacity with Cycling and Local Film Crystallinity

Simon and co-workers[65] collected XRD data of T- Nb_2O_5 film as a function of lithiation potential. They observed that 001 (3.9 Å), 180 (3.1 Å) and 181 (2.5 Å) planes shifted to higher d-spacing values when Li^+ was inserted into the lattice. From their study, it can be inferred that these planes provide the necessary pathway for Li^+ to intercalate and translate

through the material.[65] These planes are readily identified in the FFT of the uncycled film (Figure 3.3a, bottom).

The progressive loss of crystallinity of T-Nb_2O_5 films with cycling is evidenced by the changes seen in these planes at 1 cycle, 1000 cycles, and 2000 cycles (Figure 3.2c). This analysis focuses on the major three planes, 001 (3.9 Å), 180/200 (3.1 Å) and 181/201 (2.5 Å) (Figure 3.2c, yellow). The remaining unmarked reflections are predominantly derived from the same families of planes but are much weaker in intensity. It should be noted that the resolution of these TEM images is insufficient to permit the 180 (3.14 Å) and 200 (3.09 Å) or the 181 (2.45 Å) and 201 (2.43 Å) planes to be resolved. Instead, the d-spacings of each appear as 3.1 Å and 2.5 Å, respectively.

After the first lithiation of the pristine T-Nb_2O_5 thin film sample (Figure 3.2c, 1 cycle), the presence of both shifted and unshifted reflections are seen, revealed by the doubling of the reflections. This implies that lithiation of the lattice was incomplete and both lithiated and delithiated domains in the film are contributing to the TEM image in this region. Multiple reflections and distortions are also observed for the 180/200 (3.1 Å) and 181/201 (2.5 Å) planes but the measured shifts in these reflections are too small to significantly deviate from the literature d-spacings. While the lithiated sample has a distorted orthorhombic structure, it has not lost significant crystallinity in the first lithiation. As the sample is delithiated (Figure 3.2c, 1 cycle), the FFT shows that the sample returns to the initial orthorhombic state. The FFT shows the presence of only the 180/200 (3.1 Å) plane, doubled peaks signaling the presence of lithiated and delithiated domains are no longer visible.

By the 1000th cycle, the distortions in the lattice are more evident in the lithiated FFT. While the reflections for the three major lithiation planes are indexed with literature values, multiple double reflections can be seen with slight deviations from the literature distances. Blurring of the bright reflections into rings can be attributed to a decrease in the crystallite size and random orientation of the crystals approaching a more polycrystalline sample as

the stress of de/lithiation damages the crystal integrity. As the sample is delithiated, the family of planes with the d-spacing of 4.9 Å (Figure 3.2c, blue) can be assigned to the 060 plane, but this plane has not been show to contribute to lithiation in T-Nb_2O_5.

After 2000 cycles, the lattice is severely distorted. In the lithiated sample, the d-spacings for the 180/200 and 181/201 planes show significant deviations from the literature values. Reflections that do not conform to the orthorhombic model are proposed to be the result of minor to severe deformations from the parent orthorhombic structure (Figure 3.2c, orange). For the 181/201 (2.5 Å) plane, reflections show both an increase in the d-spacing (2.6 Å) which can be attributed to expansion due to lithiation and a decrease in the d-spacing (2.3 Å) which could be due to degradation of the crystallinity. In the delithiated state, all the visible planes do not revert back to the original orthorhombic structure after thousands of cycles, but appear to remain contracted as compared to literature values. By 2000 cycles, the distortions in the d-spacings are much more severe and irreversible. Although faint, the family of reflections with 5.0 Å d-spacing corresponding to the 060 plane is again visible at 2000 cycles.

As the films are cycled beyond 2000 cycles, several reflections show the orthorhombic structure (3.9 Å, 3.1 Å, 2.5 Å) (Figure 3.2c, yellow), but most of the reflections show distorted orthorhombic planes (3.2 Å, 3.0 Å, 2.3 Å, 2.4 Å, 2.6 Å) (Figure 3.2c, orange) or orthorhombic planes that do not contribute to lithiation (4.9 Å, 5.0 Å) (Figure 3.2c, blue). The distorted reflections are also doubled and blurred, representing a small crystallite size, random crystal orientation, and nonuniform lithiation throughout the film. Finally, after 10,000 cycles, the distortions increase to the point that the whole structure breaks down and only amorphous Nb_2O_5 remains (Figure 3.3b). To summarize, as the lithiation-delithiation progresses, the T-Nb_2O_5 structure slowly degrades to a completely amorphous structure, destroying the lowest energy pathways for Li^+ through this lattice (Table 1). In addition to impeding Li^+ transport in the lattice, the loss of crystallinity can be expected to reduce the rate of Li^+

intercalation and to increase the electrical resistance of the T-Nb$_2$O$_5$. These TEM observations demonstrate that the observed capacity fade (Figure 3.2b) occurs in parallel with a monotonic loss of lattice integrity and, eventually, the complete loss of the orthorhombic crystal structure.

Table 3.1: Evolution of T-Nb$_2$O$_5$ structure with cycling.

Cycle	Phases	
	Lithiated	Delithiated
Pristine	-	Orthorhombic
1	Expanded Orthorhombic	Orthorhombic
1000	Disoriented Orthorhombic	Deformed Orthorhombic
2000	Deformed/disoriented Orthorhombic	Highly deformed/disoriented Orthorhombic
10000	Amorphous	Amorphous

3.3.3 Delamination of the T-Nb$_2$O$_5$ Film from the FTO

In parallel with the loss of crystallinity seen in the TEM data of Figures 3.2 and 3.3, cross-sectional TEM images of the T-Nb$_2$O$_5$ film/FTO interface (Figure 3.4) reveal a second process is occurring that is likely to depress C_{sp}. This is the delamination of the film from the FTO current collector resulting in the formation of cavities (Figure 3.4, white regions). For the pristine T-Nb$_2$O$_5$ film, a tight interface is observed (Figure 3.4a). However, small cavities are already observed after just one lithiation/delithiation cycle (Figure 3.4b), and these cavities pervade most of the interface after 1000 cycles, extending for up to one micron (Figure 3.4c). Strain between the FTO electrode and the T-Nb$_2$O$_5$ film is a likely cause for

the loss of film adhesion to the FTO and the formation of cavities at this interface.
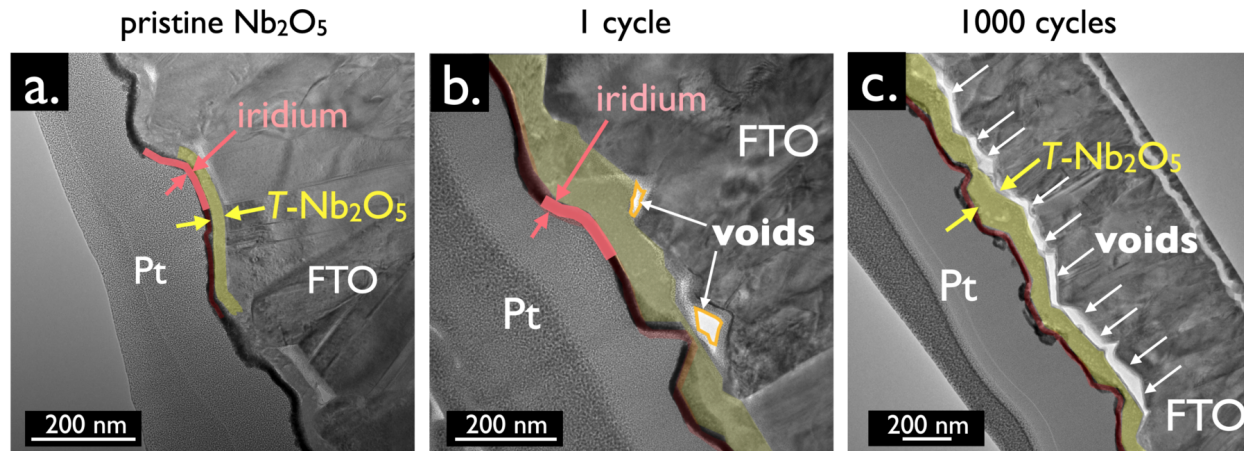
Figure 3.4: Cross-sectional TEM of the T-Nb$_2$O$_5$ film/FTO Interface. a) pristine T-Nb$_2$O$_5$ film showing intimate contact between the film and the FTO. b). After one lithiation/delithiation cycle, small voids (white outlined in orange), begin to open between the film and the FTO. c). After 1000 cycles, delamination between the FTO and the film extends for up to one micron.

This progressive delamination of the film from the FTO conductor provides a second mechanism, in addition to the degradation of the T-Nb$_2$O$_5$ lattice itself, that can be expected to contribute to the increased electrical resistance at the FTO/film interface potentially contributing to a loss of C_{sp}.

3.3.4   SEM Images and EDS Elemental Mapping

Strain caused by the volume change produced by lithium intercalation/deintercalation is implicated in the degradation of the orthorhombic T-Nb$_2$O$_5$ lattice (Figures 3.2,3.3), and in the delamination of the film from the FTO current collector (Figure 3.4). On the other side of the film which is in contact with the electrolyte, the roughening and pitting of cycled T-Nb$_2$O$_5$ film surfaces is seen in *ex-situ* SEM images (Figure 3.5). An EDS elemental map showing the Nb L$_{\alpha_1}$ peak reveals dark areas where active material is no longer present. Pris-
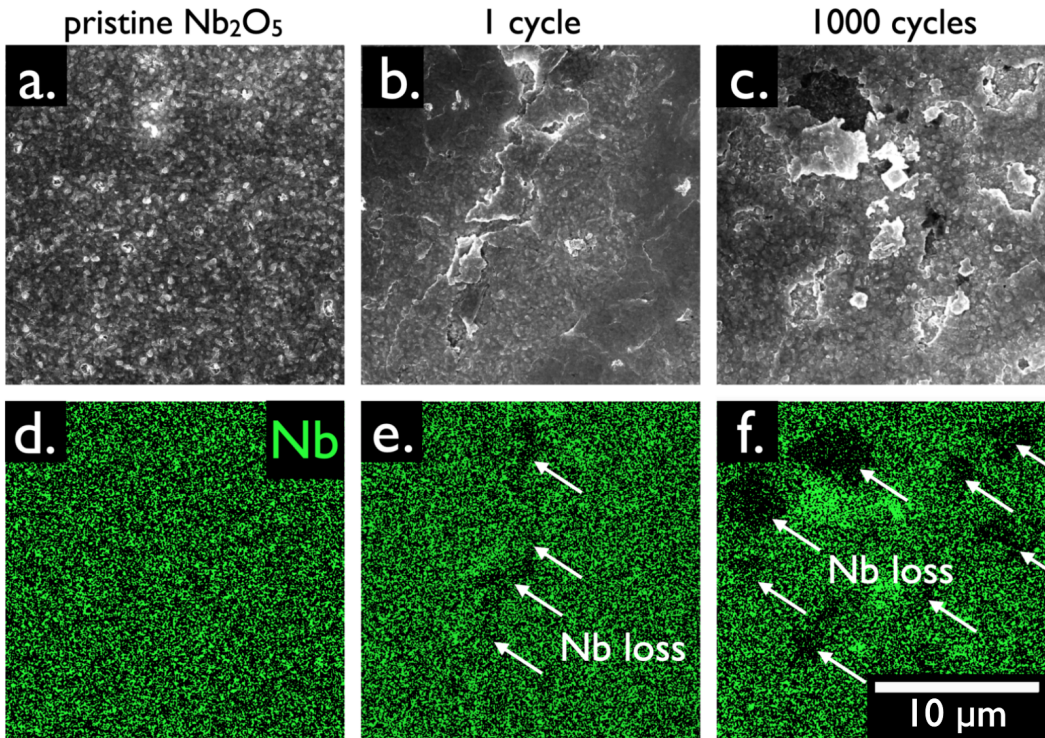
Figure 3.5: SEM (a,b,c) and EDS (d,e,f) analysis of T-Nb$_2$O$_5$ film surfaces. a,d) Typical texture for pristine T-Nb$_2$O$_5$ films. EDS analysis of this region shows quasi-uniform Nb signal (green). b,e) After one lithiation/delithiation cycle, cracking of the film surface is observed. Such cracks also show loss of Nb signal. c,f) After 1000 cycles, pitting and flaking of the film surface is seen.

tine, uncycled films show typical pebbled texture that derives from the deposition of colloidal Nb$_2$O$_5$ particles during EPD film growth (Figure 3.5a). These films show a quasi-uniform Nb EDS signal across the image (Figure 3.5d). After just one lithiation/delithiation cycle, cracking is observed (Figure 3.5b) and loss of Nb is seen at these cracks (Figure 3.5e). For films cycled 1000 times, pitting and flaking of the film surface is pronounced (Figure 3.5c) and Nb loss is co-localized with these defects (Figure 3.5f).

48

3.3.5 Bulk Crystallinity as a Function of Cycling

While TEM probes the localized crystalline structure of these films in nanometer-scale regions, x-ray diffraction is capable of assessing the spatially averaged structure across a much larger, 100 micron or millimeter-scale area, probed by the x-ray beam. Thus, TEM and XRD provide fully complimentary data on the evolving structure of these films as degradation occurs. To this end, grazing incidence XRD (GIXRD) was conducted on a series of T-Nb_2O_5 films across the same 10,000 cycle range explored by TEM and other techniques in this study.

The GIXRD pattern of the pristine, uncycled film aligns with the literature pattern for T-Nb_2O_5,[8,13,65] in agreement with the diffractions points seen in the FFT of the pristine film (Figure 3.3a, bottom), and tetragonal SnO_2 from the FTO (Figure 3.6a).[112] The three planes associated with the main lithiation pathways are tracked as a function of cycling (Figure 3.6b). The calculated d-spacing for the 001, 180/200, and 181/201 planes are 3.911 Å, 3.099 Å, and 2.438 Å respectively, which agree with the d-spacing values measured from TEM. Crystallite size calculated using the Scherrer equation is approximately 20 nm.
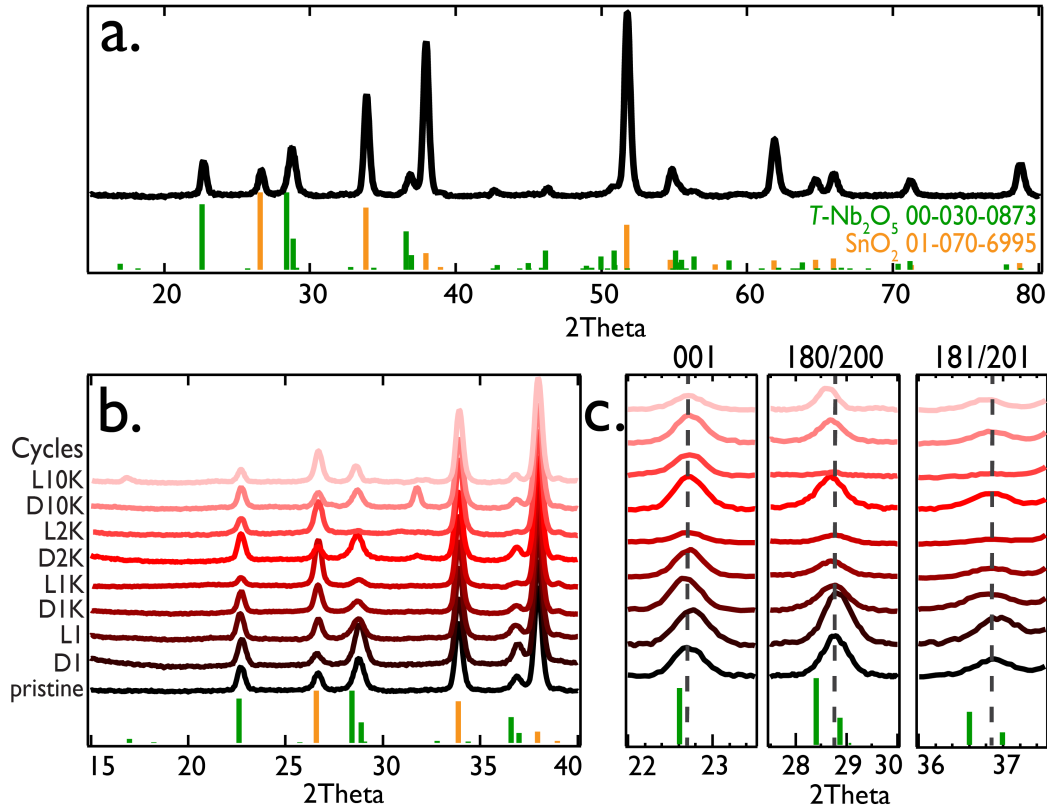
Figure 3.6: Grazing incidence XRD (GIXRD) data for T-Nb_2O_5 thin films on FTO. a) GIXRD pattern for a pristine T-Nb_2O_5 film on FTO. T-Nb_2O_5 reflections are indexed in green and SnO_2 reflections from the FTO substrate are indexed in orange. b) XRD patterns collected from 15 to 40 degrees across 10,000 cycles. Delithiated films are denoted with a "D" and lithiated films are labeled with "L". GIXRD data for films cycled for 0 (pristine), 1, 1000, 2000, and 10,000 cycles are shown in both the lithiated and delithiated state. The reflection at 31.8^o can be assigned to the cubic phase of SnO_2 from FTO and the small reflection at 16.9^o in the 10,000 cycle lithiated sample is assigned to the 130 plane of T-Nb_2O_5 with a d-spacing of 5.2 Å. c) Expanded windows for the 001, 180/200, and 181/201 reflections showing changes in peak position as compared to the pristine sample (dashed line).

After one cycle, GIXRD reflections are shifted to a smaller d-spacing for delithiated films and a larger d-spacing for lithiated films (Figure 3.6b,c). Approximately a 0.01 Å contraction/expansion is observed which can account for the lack of significant change in the d-spacing measured by TEM between the pristine film and the one cycle de/lithiated films (Figure 3.2c, Figure 3.3a bottom, Figure 3.6b,c). Simon and coworkers[65] measured a 0.1 Å change

in d-spacing with lithiation in T-Nb$_2$O$_5$ electrodes, suggesting nonuniform de/lithiation in the thin films observed here. Peak broadening from pristine films to films after one cycle can suggest that films are partially de/lithiated and the XRD reflections represent both states of lithiation across the film (Figure 3.6c). Additionally, peak broadening could be due to a decrease in crystallite size which is seen in TEM by the blurring and doubling of diffraction spots (Figure 3.2c).

By 1,000 cycles, signs of degradation are noticeable, particularly in the lithiated films (Figure 3.6b,c). Very little peak shift occurs with lithiation and delithiation suggesting that these lithiation pathways are starting to deteriorate. A slight increase in peak broadening, especially in the lithiated samples, continues to suggest that films are non-uniformly lithiated as seen in the TEM. Furthermore, the low intensity of T-Nb$_2$O$_5$ reflections hints at a decrease in the crystallinity of the film.[113]

At 2,000 and 10,000 cycles, there is virtually no change in d-spacing between the pristine film and the de/lithiated films except for the 180/200 plane which appears to remain lithiated even in the delithiated sample (Figure 3.6b,c). The intensity of the lithiated (Figure 3.6b,c) film after 2,000 cycles is so low that the 180/200 and 181/201 peaks appear amorphous. However, in contrast to the TEM data of Figure 3.3, GIXRD does not show that the films are amorphous after 10,000 cycles. However in view of the fact that crystallinity of these films is substantially degraded at 1,000 and 2,000 cycles, the possibility exists that film delamination of the 10,000 cycle samples from the current collector occurred, preventing these films from cycling and preserving the crystallinity of these samples. This scenario is supported by the fact that little change in d-spacing and peak width are observed between the pristine film and the 10,000 cycle film samples. A decrease in cycle stability and little change in crystallinity hints that the delaminated portion of the film does not contribute to de/lithiation capacity.

Overall, these GIXRD data support the conclusion that in the bulk of these T-Nb$_2$O$_5$ films,

lithiation pathways deteriorate as a function of cycling as evidenced by the loss of d-spacing changes - between lithiated and delithiated films - after 2,000 cycles. TEM hints that local regions within these films are "trapped" in a lithiated or delithiated state by 2,000 cycles, accounting for the broad peaks seen in GIXRD that average out to d-spacing values close to those of an uncycled film. Between 2,000 and 10,000 cycles, the lack of amorphization in GIXRD and low capacity suggest that large areas of the films delaminate to the point where they can no longer contribute to de/lithiation and stop degrading. However, TEM shows that regions that do remain in contact become fully amorphous by 10,000 cycles.

3.3.6 *ex-situ* XPS Analysis of Surface Chemical Composition.

In 2016, Yu and co-workers[103] used *ex-situ* XPS to monitor the oxidation state of a Nb_2O_5 nanosheet anode as a function of its equilibrium potential in 1 M $NaClO_4$ in a mixture of ethylene carbonate and propylene carbonate. They found that upon intercalation of sodium cations, Nb 3d peaks shift to a lower binding energy due to conversion of most Nb^{5+} centers to Nb^{4+} centers, and then reverts to higher binding energy upon deintercalation.[103] Luo and co-workers[114] also investigated the sodiation of T-Nb_2O_5 using *ex-situ* XPS over the course of two cycles and noted that a full conversion of the Nb metal centers between the charged and discharged states was not observed. Rather, the Nb centers cycled between two charge states, $Nb^{4.92+}$ and $Nb^{4.10+}$, suggesting a mix of Nb valences are present in the sample throughout the sodiation process. These studies focused on the initial intercalation and deintercalation cycles for Nb_2O_5.

Few investigations report the XPS analysis of the surface chemical state of T-Nb_2O_5 caused by long term cycling. Nakajima and co-workers[115] looked at different states of charge over the course of ten lithiation/delithiation cycles for T-Nb_2O_5 films. These authors reported a reversible shift of 0.5 eV to lower binding energies for the Nb 3d peaks when the sample
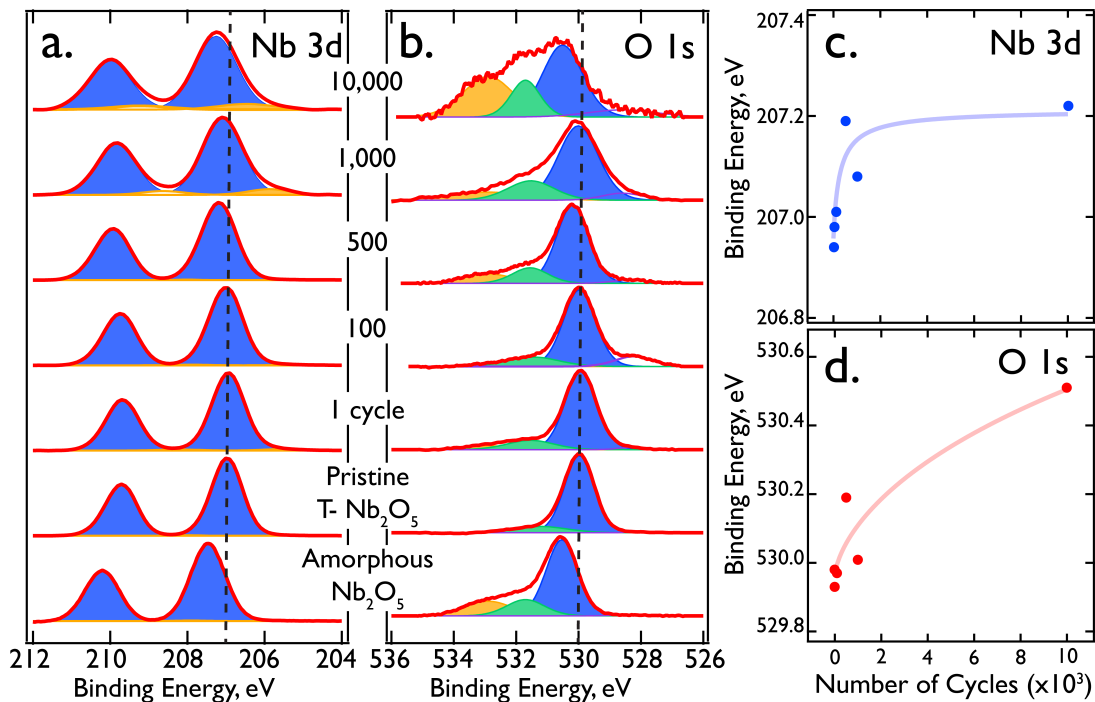
Figure 3.7: XPS Analysis of delithiated T-Nb_2O_5 as a function of number of lithiation/delithiation cycles. a). Nb 3d high resolution photoelectron spectra for five T-Nb_2O_5 samples subjected to 1 - 10,000 cycles compared with pristine and amorphous (un-annealed) samples. Blue fittings corresponds to Nb^{5+} and orange corresponds to Nb^{4+}. b) Oxygen 1s photoelectron spectra for the same samples shown in (a). In these spectra, blue corresponds to lattice O^{2-}, green to non-lattice oxygen, and orange to adsorbed OH^- and H_2O. c) Plot of Nb 3d binding energy *versus* number of cycles, d) Plot of O 1s binding energy *versus* number of cycles.

was fully lithiated. Subsequent cycling led to the disappearance of clear peaks in the Nb 3d region. In the O 1s spectra, lithiation caused an irreversible 2 eV shift in the lattice O^{2-} peak from 531.3 to 533.3 eV, that recovered to 533.0 eV upon delithiation.[115]

XPS data was acquired for delithiated films as a function of the number of lithiation/ delithiation cycles (Figure 3.7a,b). As-synthesized but un-annealed Nb_2O_5 films show Nb 3d peaks (Figure 3.7a, "Amorphous") with binding energies of 207.47 and 210.21 eV assigned to Nb $3d_{5/2}$ and $3d_{3/2}$, respectively, in agreement with literature values for amorphous Nb_2O_5 films.[116] Calcining introduces oxygen vacancies to T-Nb_2O_5 films (Figure 3.7a, "Pristine"), and this is demonstrated by the Nb:O stoichiometry of 29.9% Nb and 70.1% O, correspond-

ing to a stoichiometry of $Nb_2O_{4.7}$ for the orthorhombic films. Nb $3d_{3/2}$ and Nb $3d_{5/2}$ peaks are shifted lower by ∼500 meV in the films annealed at 600° C, compared with the amorphous material. These shifts are similar to those seen by others who have investigated Nb_2O_5 with oxygen vacancies resulting from elevated annealing temperatures.[117,118] For example, Atak investigated the effect of heat treatment on the optical, structural, electrochromic, and bonding properties of 0.125 inch thick T-Nb_2O_5 films and observed a negative shift of 300 meV upon annealing as-synthesized material at 600°C.[117] The O 1s region in the pristine film (Figure 3.7b, "Pristine") shows the presence of three peaks at 530.0, 531.0, and 532.1 eV which correspond to lattice O^{2-}, non-lattice oxygen, and adsorbed -OH and H_2O, respectively.[119] Film stoichiometry was determined using the peaks for lattice O^{2-} and non-lattice oxygen. Atak and co-workers[117] reported a negative shift by 0.4 eV in the binding energy of the O 1s peaks after annealing their films to 600°C, which is also seen here for films transitioning from amorphous Nb_2O_5 to crystalline T-Nb_2O_5.

After one lithiation/delithiation cycle, a small shift in Nb 3d peaks by 40 meV is observed (Figure 3.7a, "1 cycle"). This shift is much smaller than the ∼0.5 eV shift to lower binding energy that has been reported when Nb_2O_5 films are lithiated[116] but it is in the same direction. This implies that it could be a consequence of irreversible Li insertion into the T-Nb_2O_5. In the O 1s spectrum (Figure 3.7b, "1 cycle") the lattice O^{2-} peak is also shifted negative by 30 meV. This is interesting because the irreversible shift seen by Nakajima and co-workers[115] is absent here. As the T-Nb_2O_5 is cycled, Nb 3d peaks steadily shift to higher binding energies, approaching values seen in amorphous films (Figure 3.7a,c). The O 1s spectrum displays similar behavior, with both lattice O^{2-} and non-lattice oxygen peaks shifting to higher binding energies (Figure 3.7b,d). The observed evolution of O 1s and Nb 3d are consistent with an increasing contribution of high valance Nb^{5+} as cycling progresses. In parallel with these shifts, both Nb 3d and O 1s peaks also broaden considerably. For example, in the case of the Nb 3d peaks (Figure 3.7a), the line-width of the Nb 3d peaks for pristine T-Nb_2O_5 is 0.95 eV, and these peaks broaden to 1.35 eV after 10,000 cycles,

suggesting an increase in the heterogeneity of the Nb chemical state. Even more dramatic broadening of the O 1s peak (Figure 3.7b) is caused by increased contributions from non-lattice O and adsorbed H_2O and OH^- species.

The evolution of the XPS spectrum with cycling can be accounted for by a combination of two processes: First, T-Nb_2O_5 films become progressively more amorphous with cycling causing line-widths to broaden for both Nb 3d and O 1s peaks. The amorphous, as-synthesized state of Nb_2O_5 has an oxidation state of Nb^{5+}. Calcination imparts crystallinity while also intro-ducing oxygen vacancies resulting in a mixture of Nb^{4+} and Nb^{5+} species.[117,120] Continuous cycling, and the associated repetitive stress of lithium insertion and deinsertion, leads to fatigue of the T-Nb_2O_5 lattice culminating in a collapse of the orthorhombic structure and the formation of an amorphous Nb_2O_5. The resulting inhomogeneity of Nb centers accounts for the increased line width of the Nb 3d peaks after being cycled 10,000 times.

Second, a progressive loss of T-Nb_2O_5 is occurring as a consequence of pitting (Figure 3.5) and, potentially, dissolution of the film as more soluble Nb^{4+} dissolves into the electrolyte during cycling, leaving behind less soluble Nb^{5+} of the delithiated oxide. To corroborate this hypothesis, XPS was used to examine the composition of salts recovered by evaporation from the electrolyte used for lithiating/delithiating T-Nb_2O_5 films for 10,000 cycles (Figure 3.8). There is overlap between the regions where Nb 3d peaks and Cl 2p peaks from the perchlorate salt used as electrolyte appear, however the Nb $3d_{5/2}$ peak and the O 1s lattice O^{2-} peak are observed at 206.7 eV and 533.2 eV respectively, binding energies which are characteristic of Nb^{4+} species.[121] This supports the hypothesis that Nb^{4+} is selectively dissolved from the film into the electrolyte.
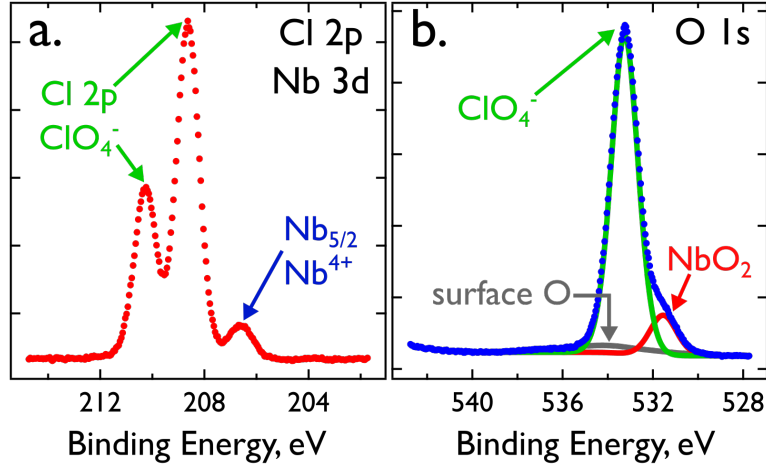
Figure 3.8: XPS analysis of dissolved salts recovered from electrolyte after 10,000 cycles. a). Overlapping Cl 2p and Nb 3d regions showing both Cl 2p peaks consistent with ClO_4^- and Nb^{4+} peaks. b). O 1s region with deconvolutions illustrating contributions from surface oxygen, ClO_4^-, and NbO_2, as indicated.

3.3.7 Degradation and the Niobium Co-ordination Sphere: *Ex-situ* Raman Spectroscopy

There is extensive literature on crystal disorders and phase changes observed in the Raman spectra of niobium oxides.[122–124] Amorphous niobia consists of distorted NbO_6, NbO_7, and NbO_8 polyhedra, characterized by strong and broad stretching modes at or about 650 cm^{-1} in the Raman spectrum.[125] Crystalline niobia are characterized by Nb-O-Nb stretching at 690 cm^{-1}, with sharper transitions than are seen for the amorphous phase, since a majority of the polyhedra are NbO_6 and a minority of polyhedra have distorted co-ordination. Raman spectra evolution of lithiated and delithiated T-Nb_2O_5 performed by Liu and coworkers[126] showed a weakening of signal intensity between 570-770 cm^{-1} upon lithiation. They suggest that this attenuation is due to Li$^+$ "bridging" Nb-O-Nb oxygens across layers, confirming that Raman peaks in the 570-770 cm^{-1} region correspond to Nb-O-Nb stretching.[126]

The influence of the repetitive stress imposed by many lithiation/delithiation cycles on the

stretching frequencies of niobia, however, has not been intensively investigated. But the influence of another mode of damage, mechanical milling, was studied by Senna and co-workers.[127] Starting with pure monoclinic Nb_2O_5, damage by milling induced a softening of the Nb-O-Nb stretch by up to 10 cm^{-1} coupled with an increase in its full width half maxima (FWHM).[127] Figure 3.9a shows the progress of niobium pentoxide degradation monitored via Raman spectroscopy, at regular intervals from pristine to 10,000 cycles. The 60 nm T-Nb_2O_5 film was deposited on a 600 nm fluorine doped tin oxide (FTO) layer which in-turn was deposited on glass. The glass layer shows a vibration at 560 cm^{-1} (shown in blue) and vibrations of the FTO appear at 600 cm^{-1} and 630 cm^{-1} (shown in green) along with a weak vibration near 680 cm^{-1} (shown in gray) that was not seen in the Nb_2O_5 films (Figure 3.9a). Pristine, uncycled orthorhombic Nb_2O_5 shows an average stretching vibration band at 686 cm^{-1} with a FWHM of 72 cm^{-1} and changes in these values are tracked across the 10,000 cycles (Figure 3.9b,c).

The FWHM of the Nb-O-Nb band (Figure 3.9b) increases significantly (up to 7 cm^{-1}) after 1000-2000 cycles. This is attributed to an increase in the inhomogeneity of the polyhedra in these degraded films. The increase in FWHM coincides with TEM images that show strong distortions of the orthorhombic structure, also at 2000 cycles (Figure 3.2c). With cycling, the Nb-O-Nb stretching peak shift fluctuates about 5 cm^{-1} (Figure 3.9c), but it remains in the range from 685 to 692 cm^{-1} providing no definitive evidence for a change in bond order within the T-Nb_2O_5. Large error bars in both (9b) and (9c) indicate inhomogeneity of these quantities across a single sample. This makes the subtle changes in the Raman spectra difficult to precisely track due to interfering spectra of the FTO substrate, especially the small vibration around 680 cm^{-1}, but suggest that the co-ordination sphere of T-Nb_2O_5 becomes more distorted as the film is cycled.
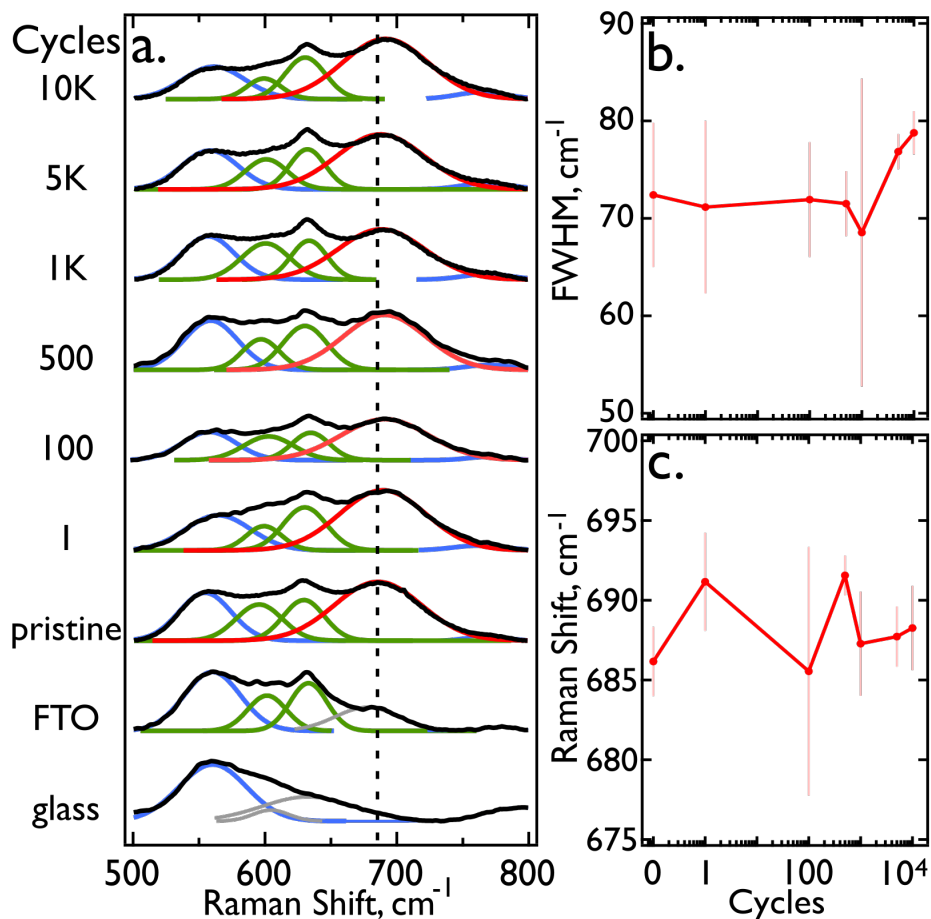
Figure 3.9: Degradation of T-Nb$_2$O$_5$ co-ordination sphere upon cycling of a 60 nm T-Nb$_2$O$_5$ film deposited on FTO@glass to 10,000 cycles, monitored *via ex-situ* Raman spectroscopy. a) Raman spectra at different intervals of cycling left at a delithiating potential. The blue curve depicts the stretching vibrations for the glass substrate, green for FTO, and red for the Nb-O-Nb stretching vibrations. Gray curves in glass spectra correspond to weak stretching vibrations that are more prominent in the FTO spectra and the gray curve in the FTO spectra notes a weak stretching vibration in the FTO that is hidden by the Nb-O-Nb stretching vibration. b-c) Changes in the FWHM and Raman shift, respectively, across 10,000 cycles measured across several regions of the films.

3.3.8 Electrochemical Impedance Analysis (EIS)

In contrast to the other techniques employed in this study, EIS was used as an *in-situ* rather than an *ex-situ* probe of the electronic and electrochemical properties of T-Nb_2O_5 films during cycling.[128] EIS has been used to study Nb_2O_5 battery electrodes[129,130] and supercapacitors[118,131–133] systems, but its application to degradation analysis has not yet been reported to our knowledge. A simple two-interface circuit provides excellent fits to our EIS data across all 10,000 scans (Figure 3.10a,b,c). This circuit accounts for the impedance contributions of two interfaces with parallel capacitor-resistor pairs: the FTO/T-Nb_2O_5 interface (interface 1), and the T-Nb_2O_5/solution interface (interface 2). In addition, a solution resistance, R_s is included in series. Constant phase element (CPE) approximations of a capacitor are used in this analysis.[128]

Nyquist plots acquired at 7 frequencies (Figure 3.10a) consist of two, fused semicircles that are well modeled by this equivalent circuit (solid lines, Figure 3.10a). However, stable values for the circuit elements R_1, CPE_1, R_2, and CPE_2 are not obtained until after $\sim$100 cycles. The initial impedance response is characterized by highly fluxional values for all four circuit elements, as seen for example in the <1000 cycle data of CPE_2 (Figure 3.10f). This impedance instability is attributed to the mechanical delamination of the T-Nb_2O_5 film from the FTO surface, as documented by the TEM cross-sections of Figure 3.4. As indicated above, we speculate that delamination is the result of the relief of strain between the FTO and T-Nb_2O_5 imposed by lithiation volume expansion of the T-Nb_2O_5. Once delamination has occurred and this strain is relieved, impedance noise disappears and high signal-to-noise impedance data are obtained (Figure 3.10e,f).

Delamination is expected to increase R_1 as electrical continuity between the FTO and the and T-Nb_2O_5 film is lost, and decrease CPE_1 by increasing the effective "capacitor spacing" as the FTO and T-Nb_2O_5 film surfaces are progressively separated from one another. These
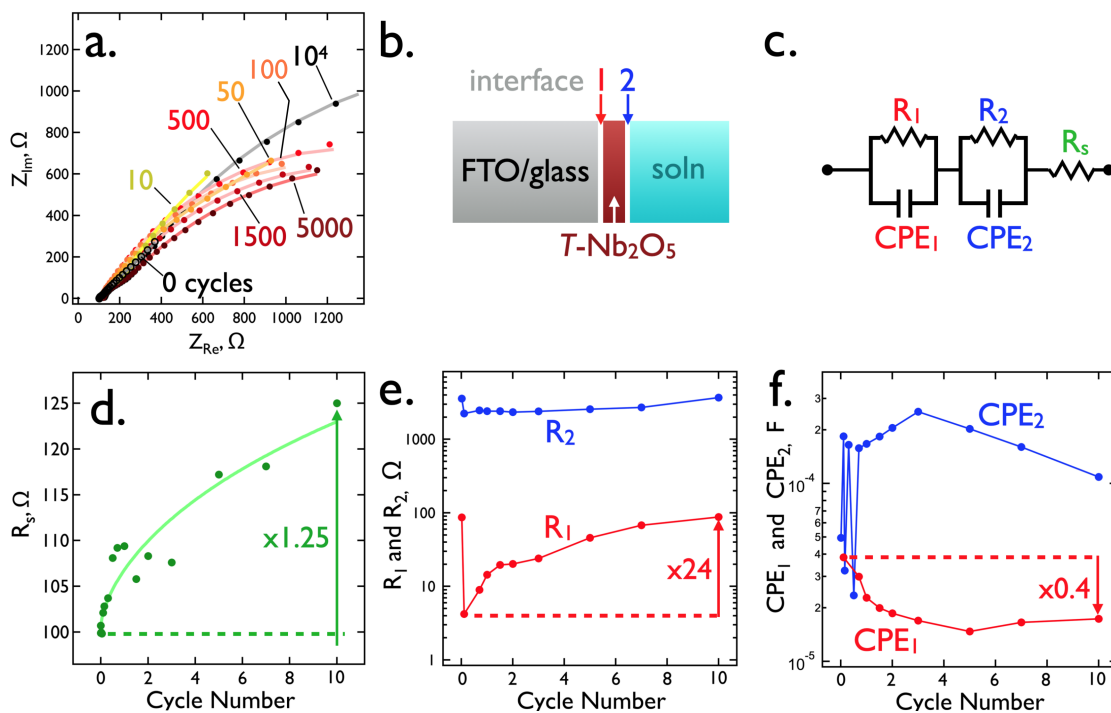
Figure 3.10: EIS analysis of T-Nb_2O_5 films. a). Nyquist plots of EIS frequency spectra acquired from 1 Hz to 40 kHz for the delithiated state of T-Nb_2O_5 films in 1.0 M $LiClO_4$, PC. Voltammetric scanning at a rate of 200 mV/s for this film was interrupted at 16 junctures and EIS spectra acquired. Data from 7 data sets, are shown here for clarity. The solid lines are least squares fits to the equivalent circuit model shown in (c). b). Schematic diagram showing the system under investigation, c) Equivalent circuit used to model the EIS response of a T-Nb_2O_5 film on FTO. d) R_s versus number of cycles. e). Log-linear plots of the resistances R_1 and R_2. f). Log-linear plots of the constant phase elements (CPEs) CPE_1 and CPE_2.

two changes are observed in the data of Figure 3.10e and 3.10f which documents an increase in increase R_1 by a factor of 24, and a decrease in CPE_1 by 40%.

Changes in R_2 and CPE_2, the culmination of a loss in crystallinity by the T-Nb_2O_5 film, are somewhat more difficult to rationalize. The conversion of a crystalline T-Nb_2O_5 film to an amorphous one should increase R_2, and this is clearly observed: R_2 increases substantially, by 48%, from 2.5 kΩ to 3.7 kΩ from 100 to 10,000 cycles (Figure 3.10e). CPE_2, on the other hand, increases from 1.5×10^{-4} F at 1000 to 2.5×10^{-4} F at 2000 cycles, but with continued cycling, CPE_2 declines to 1.0×10^{-4} F at 10,000 cycles. The source of the noise seen in the CPE_2 data for <1000 cycles is likely caused by the delamination of the film from the FTO.

Finally, the solution resistance, R_s, stays almost constant throughout 10,000 scans, increasing by just 25% (Figure 3.10d). In view of the magnitude of the changes to the other circuit elements measured here, this change is inconsequential.

How will the observed changes to these five circuit elements influence the performance of T-Nb_2O_5 films? To answer this question, it is important to appreciate that even at the rapid, 200 mV/s scan rate and a 1.8 V voltage window, the effective frequency is just 0.06 Hz - considerably lower than the 1 Hz lowest frequency measured in this study. So in terms of impacting the energy storage performance of these films, the low frequency impedance provides the most direct measure of impact. The total film impedance, Z_{total} at 1 Hz, encompassing the capacitive (Z_{im}) and the resistive (Z_{re}) impedance components ($Z_{total} = (Z_{im}^2 + Z_{re}^2)^{1/2}$), increases from 780 Ω at 10 cycles to 1860 Ω at 10,000 cycles. So the approximate doubling of the Z_{total} coincides with a reduction in C_{sp} by one-half (from ~400 C/g to ~200 C/g, Figure 3.3b), quantitatively as expected.

3.4 Conclusion

We report the characterization as a function of number of lithiation/delithiation cycles of ultra-thin (60 nm) T-Nb_2O_5 films prepared by EPD. Many (>100) identical films were prepared and characterized using *ex-situ* tools including TEM, SEM, EDS, GIXRD, XPS, Raman microprobe spectroscopy, cyclic voltammetry, and (*in-situ*) EIS. The main conclusions of this work are the following:

As-prepared T-Nb_2O_5 films prepared by EPD exhibit high C_{sp} in the 400 F/g range approaching the theoretically expected maximum value of 403 F/g, and highly reversible electrical energy storage, retaining significant C_{sp} for up to 10,000 cycles; losing approximately 50% over this number of scans (see data in Figure 3.2b).

After 1000 lithiation/delithiation cycles the crystalline, orthorhombic lattice begins to undergo degradation within 1000 cycles, with numerous lattice distortions visible at 2000 cycles (Figure 3.2c). This is the interval of scans over which most of the C_{sp} loss occurs. Delamination of the T-Nb_2O_5 film from the FTO current collector producing an appreciable gap is observed (Figure 3.4). SEM/EDS images of the film surfaces shows circular pitting with complete loss of Nb signal within these regions (Figure 3.5). An inhomogeneity develops in the co-ordination sphere of oxygens about Nb centers, and NbO_7 and NbO_8 co-ordinations are observed along with NbO_6 characteristic of T-Nb_2O_5 (Figure 3.9). This leads to destruction of the low energy barrier pathway for Li^+ intercalation, which comprises the corner-shared NbO_6 octahedra.

In addition to impeding Li^+ diffusion, these chemical changes increase the barrier for electrons to reach the Nb centers, resulting in increased electrical resistance. This increased resistance at 1000 cycles is directly measured by EIS, which shows significant increases in both R_1 and R_2 (Figure 3.10) commencing at 1000 cycles.

Between 2000 and 10,000 lithiation/delithiation cycles. T-Nb_2O_5 films are largely rendered amorphous at 2000 cycles, and the deleterious changes in film resistance (Figure 3.10) and chemical state (Figures 3.7,3.9) continue to be observed. These are direct evidence for the selective leaching of Nb^{4+} from the film (Figure 3.8). At 10,000 cycles, chemical shifts for Nb 3d and O 1s return to values seen for freshly-deposited, amorphous Nb_2O_5 films (i.e., purely Nb^{5+}) prior to annealing. This means that these films are nearly depleted of Nb^{4+}, formed during lithiation.

Remarkably, in spite of the damage documented by these data after 10,000 cycles, the amorphous Nb_2O_5 films retain a $C_{sp} \sim 200$ F/g, or 50% of the capacity of freshly annealed and crystalline T-Nb_2O_5 films of $C_{sp} \sim 400$ F/g.

Chapter 4

In-Situ Electrical Conductivity of Lithium Niobium Pentoxide as a Function of Lithiation Potential

4.1   Introduction

The electrical conductivity, σ, of lithium ion intercalating battery electrode materials such as transition metal oxides (TMOs) like Li_xMnO_2[134–138] and Li_xCoO_2[139–141] can be strongly dependent upon the value of x. σ is also influenced by the formation of defects, dissolution, and irreversible electrochemical processes, all of these promoted by the stress/strain imposed by lithiation/delithiation cycling.[142–144] *In-situ* measurement of σ as a function of x and during potential cycling is important for understanding mechanisms of degradation and failure for TMOs and other active materials, but there are few methods for measuring the electrical conductivity of battery electrode materials *in-situ*, particularly for electrodeposited battery materials.

In-situ measurements of σ for battery electrode materials were first described in the early 1990's. A version of the method employed in the present study was first described by Baudais and Dahn[145] who evaporated WO_3 films onto two aluminum electrodes patterned on glass. The film resistance was then obtained by analyzing the current transients generated by an applied potential step between these two aluminum electrodes. Uchida and coworkers[135] deposited $Li_{(1-x)}Mn_2O_4$ using an electrostatic spray deposition process onto an interdigitated metal electrode that was then used to measure *in-situ* conduction; a strategy similar to that employed here. More recently, Sauvage *et al.*[146] used a similar approach to investigate the *in-situ* conductivity of $LiCoO_2$ and α-Fe_2O_3 films prepared by pulsed laser deposition (PLD). A different approach described by Wang, Appleby, and Little[147,148] involved the embedding nickel screen electrodes in solid-state batteries in order to directly measure the electrical resistivity of these systems *in-situ*. Prior measurements of σ have focused on films prepared by non-electrochemical means - evaporation, spray deposition, PLD.[135,145,146] All of these methods allow the material of interest to be deposited directly onto an insulating surface within the gap between two measurement electrodes as required for the conductivity measurement. This is not possible for electrodeposited materials because an electrode is required to effect the electrodeposition process and this electrode invariably interferes with the conductivity measurement.

The most common tool used for probing the electronic conductivity of battery electrode materials *in-situ* is electrochemical impedance spectroscopy (EIS) in which the resistive and capacitive components of the complex impedance are measured as a function of frequency, often across many orders of magnitude from < 1 Hz to 10^5 Hz.[139,149–153] EIS is applicable to battery electrode material prepared by any technique including electrodeposition. But an EIS frequency spectrum is not readily translated into a numerical measurement of the electrical conductivity of the battery electrode material for three reasons: 1) battery active materials are often dispersed on highly conductive current collectors that interfere with quantitative interpretation of the EIS data, 2) the precise dimensions of the battery electrode material

through which charge is conducted are often not well defined, and, 3) the resistance (or conductance) of a battery electrode is difficult to deconvolute from the total impedance using an equivalent circuit model that may contain multiple circuit elements including capacitors, ionic resistors, and other contributions. EIS does provide qualitative information on the change in conductance of a battery material as a function of potential, lithiation state, and during cycling.[139,149–153]

Recently[138] we adapted the method of Sauvage *et al.*[146] to the *in-situ* measurement of σ for electrodeposited δ-Li$_x$MnO$_2$ which demonstrated an increase in σ by up to one order of magnitude upon lithiation to $x = 1$. This approach is made possible by performing the conductivity measurement on an array of nanoribbons (NRs) instead of a film.[138] Nanoribbons of δ-MnO$_2$ with controllable dimensions (height $\times$ width $\times$ length) were patterned[138] on glass using lithographically patterned nanoribbon electrodeposition (LPNE)[154–156] which provides for the removal of the electrode in the last step of the process. Here this method is used for the *in-situ* measurement of σ for Li$_x$Nb$_2$O$_5$ as a function of lithiation potential. Electrophoretic deposition (EPD) instead of conventional electrodeposition is used to prepare the Nb$_2$O$_5$ nanoribbons.[12]

4.2   Experimental Methods

4.2.1   Chemicals and Materials

Niobium pentachloride (NbCl$_5$, 99%), ferrocene (98%), hydrogen peroxide solution (H$_2$O$_2$, 30% (w/w) in H$_2$O), and lithium perchlorate (LiClO$_4$, battery grade, dry, 99.99% trace metal basis) were all used as received from Sigma-Aldrich. Propylene carbonate (99.95%) was received from Fischer Scientific then degassed and dried on 4 Å molecular sieves. Iso-propyl alcohol, acetone, and methanol (ACS certified grade) were used as received from

Fisher Scientific. Nitric acid (70.0%) was received from VWR. Fused quartz microscope slides were cleaned using Nochromix, both received from VWR. Positive photoresist (PR) (Shipley S1808), negative PR (SU-8 2002), and respective developers (Shipley MF-319, SU-8 Developer) were purchased from Kayaku Advanced Materials. Nickel, chromium, and gold pellets for physical vapor deposition were purchased from Ted Pella. Commercial gold plating solution was obtained from Clean Earth Solutions. Millipore water (Milli-Q, ρ>18 MΩ·cm) was used for all aqueous solutions.

4.2.2   Nanoribbon Fabrication

A niobium oxide plating solution was prepared as previously described from a modification of the method by Zhitomirsky.[12,19–21] A 0.005 M NbO$_x$ colloidal plating solution was prepared by rapid, cold injection of 67.5 mg of NbCl$_5$ dissolved in 2 mL methanol into 48 mL of 0.05 M H$_2$O$_2$ at <2°C. After 3 hours of aging, the solution was used for electrophoretic deposition (EPD) of Nb$_2$O$_5$ NRs.

NRs were fabricated using an adapted method of LPNE (Figure 4.1).[138,155,156] Quartz slides (1"x1") were cleaned with Nochromix, and a 60 nm layer of nickel was deposited onto the clean, quartz slides using physical vapor deposition (PVD) (Figure 4.1a, step 1). Positive PR (Shipley 1808) was spincoated (2500 rpm, 80 s) onto the Ni coated slides and soft baked in an oven at 90°C for 30 minutes (Figure 4.1a, step 2). The PR was patterned with a contact mask using UV light (Newport, 83210i-line, 365 nm, 2.80 s) and developed (MF-319, 35 s) to reveal a pattern of 200 bands (2 cm x 4 μm) with a 4 μm pitch (Figure 4.1a, step 3). Exposed Ni was etched in 0.08 M nitric acid for 9 minutes to produce a deep undercut and a Ni edge in the undercut (Figure 4.1a, step 4). The patterned Ni film was contacted as a working electrode versus a Pt foil electrode. A two electrode electrochemical cell was used to EPD NbO$_x$ colloids in the Ni undercut under a -2 V bias for 500 s (Figure 4.1b).

The remaining PR was removed with an acetone/IPA/water rinse and the remaining Ni was removed with 0.08 M nitric acid to reveal bare amorphous niobium oxide NRs on quartz (Figure 4.1a, step 5). The NRs were annealed in a tube furnace at 600°C in air for 8 hrs to achieve T-Nb$_2$O$_5$ (Figure 4.1a, step 6). After annealing, positive PR was spincoated and pattered with the negative of the 10 μm contact pattern (Figure 4.1a, step 7). An 80 nm layer of gold with a 4 nm adhesion layer of chromium were deposited with PVD (Figure 4.1a, step 8) and the PR was lifted off using acetone to reveal the gold contacts (Figure 4.1a, step 9). Devices were spincoated with negative PR (SU-8 2002)(500 rpm, 10 s; 4000 rpm, 60 s) to insulate the gold contacts (Figure 4.1a, step 10), and an approximately 9 μm contact mask was used to photopattern and expose only the NRs (Figure 4.1a, step 11). The PR was then hard-baked on a hot plate at 150°C for 20 mins. Prior to measurements, nanoribbon devices were cleaned using O$_2$ plasma for 5 minutes.

For x-ray diffraction, the above fabrication procedure was modified to produce samples of 6000 T-Nb$_2$O$_5$ NRs and samples of core-shell Au@Nb$_2$O$_5$ nanowires. For bare T-Nb$_2$O$_5$ NRs, a 6000 NR array photolithography pattern was used instead of a 200 NR array pattern (Figure 4.1a, step 3). For core-shell Au@Nb$_2$O$_5$ nanowires, gold nanowires were first deposited at -0.9 V vs. SCE in the Ni undercut using a commercial gold plating solution as described in previous work.[155,157] PR and Ni in the middle of the device was removed to reveal gold nanowires contacted by Ni on each end. The exposed Au nanowires were then coated with niobium oxide colloids using the EPD method with a 200 s deposition at -2 V in two electrode mode. After removal of all PR and nickel, the bare core-shell nanowires were annealed. After annealing, no additional processing was performed on XRD samples.
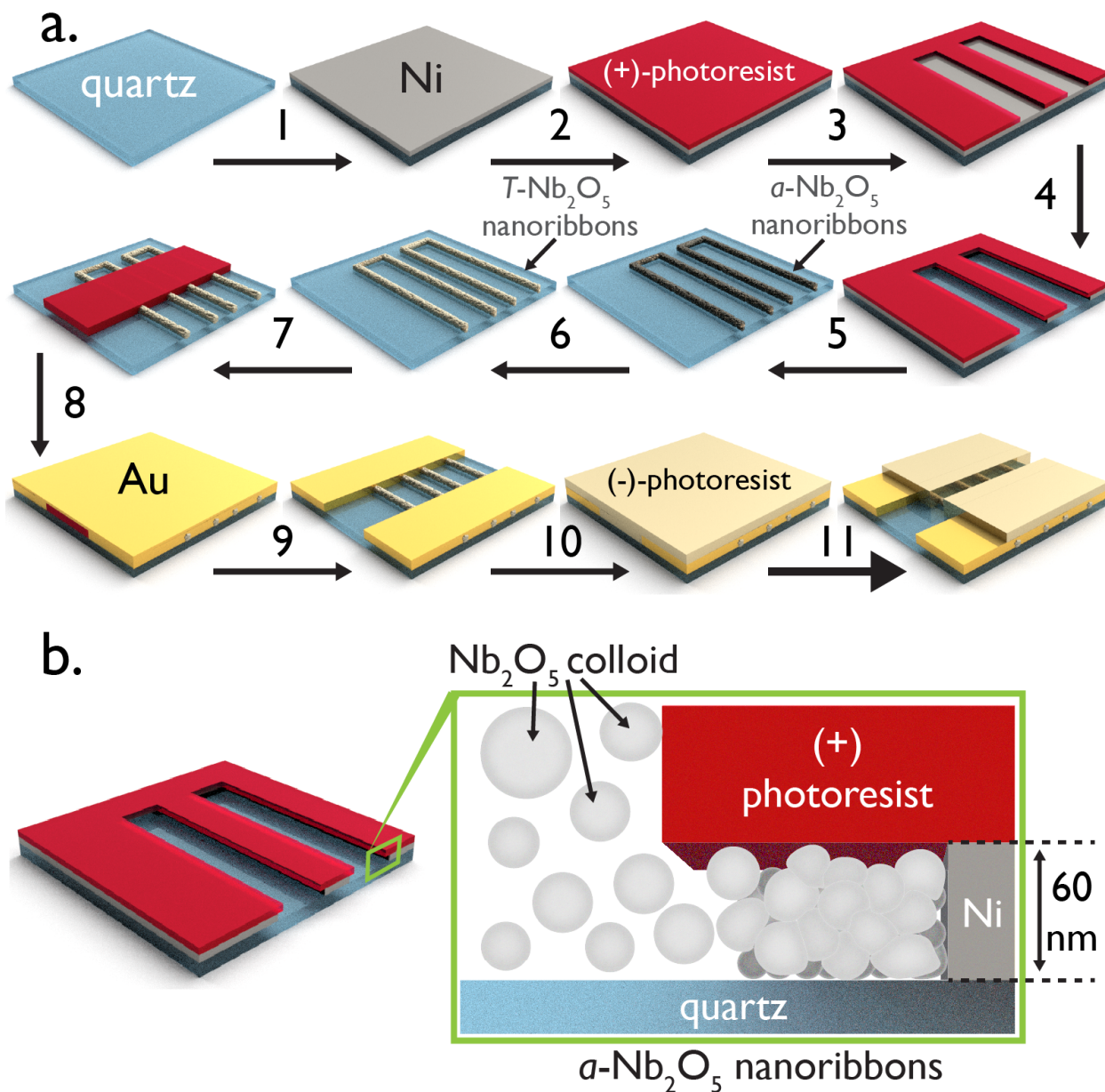
Figure 4.1: Lithographically Patterned Nanoribbon Electrodeposition (LPNE). a. Flow diagram outlining the lithography steps: (1) 60 nm of Ni is evaporated onto cleaned quartz. (2) Positive PR is spincoated on top of the Ni. (3) The PR is photopatterned with a mask of 200 2 cm x 4 μm rectangles using UV light and then developed. (4) Exposed Ni is over etched using 0.08 M nitric acid. (5) Nb_2O_5 colloids are electrophoretically deposited into the trench as depicted in b and PR and Ni is removed. (6) Amorphous Nb_2O_5 NRs are annealed at 600°C in air to the orthorhombic crystal structure. (7) Positive PR is used to protect desired nanoribbon area during (8) evaporation of 4 nm of chromium + 80 nm of gold so that (9) lift-off can be used to apply contacts to the ends of the ribbons. (10) Negative PR is used to insulate the gold contacts and (11) patterned to expose the desired area of NRs and contact points.

4.2.3   Electrochemical Methods

Electrochemical measurements were performed in a nitrogen atmosphere dry box using a Gamry Series G 300 potentiostat. Three steps were performed to collect conductance data: (1) cyclic voltammetry (CV) of T-Nb$_2$O$_5$ NRs, (2) lithiation at fixed potential using chronoamperometry (CA), and (3) conductance measurement using I-V curves. All measurements were performed in 1 M lithium perchlorate (LiClO$_4$) in propylene carbonate (PC). CVs and lithiation CA curves were measured versus a Pt wire quasireference electrode (QRE) with a glossy carbon rod (2 mm diameter) counter electrode (Figure 4.2b). Potentials were converted to versus Li/Li$^+$ using ferrocene/ferrocenium calibration of the Pt QRE.[110,158] CVs of NRs were collected over 1.04 V to 2.84 V vs Li/Li$^+$ at 1 and 10 mV/s. CAs were collected at regular potential intervals for 150 s. Conductance measurement were collected through the NRs by assigning one contact as the working electrode and the other contact as the counter/reference electrode (Figure 4.2c). IV curves were collected over a 10 mV window at 0.2 mV/s for 3 cycles. CAs and conductance I-V measurements were repeated for several de/lithiation potentials.
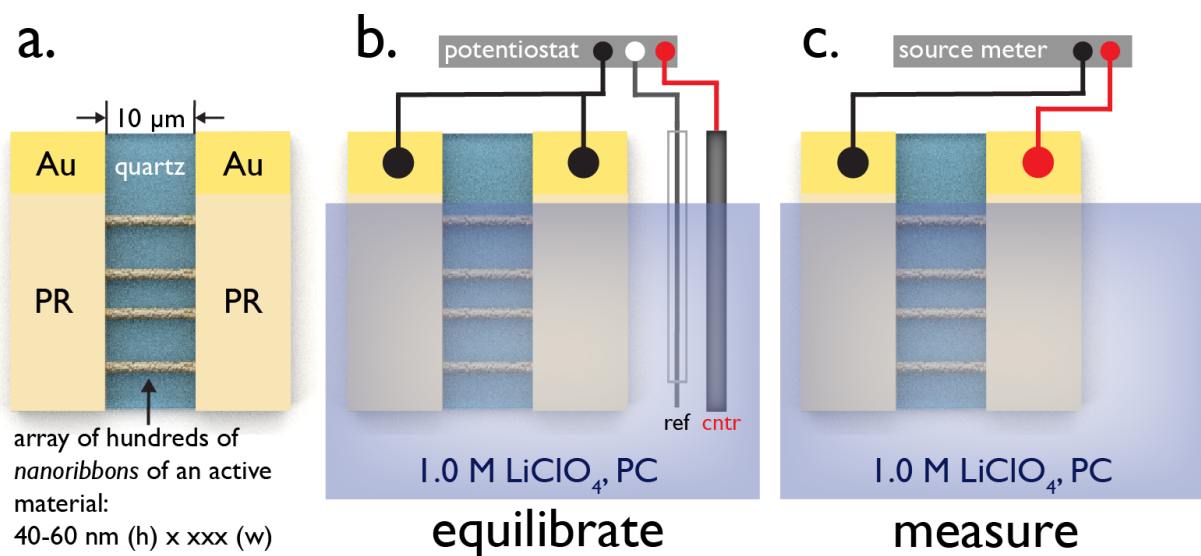
Figure 4.2: Electrochemical Set-Up for Conductivity Measurements. (a) Representative diagram of the nanoribbon devices. Hundreds of NRs are contacted across 10 μm with gold and the contacts are insulated with PR. (b) Electrochemical configuration for cyclic voltammetry and chronoamperometry equilibration. Both ends of the wires are contacted as the working electrode, a glossy carbon rod is used as a counter electrode, and a Pt wire is used as a quasireference. The electrodes are submerged in propylene carbonate containing 1.0 M LiClO$_4$. (c) To measure conductivity through the wires with I-V curves, the counter and reference are disconnected and the device contacts are connected as a positive (working) and negative (counter/reference) electrode.

4.2.4 Structural Characterization

Scanning electron micrographs (SEMs) and energy dispersive x-ray spectroscopy (EDS) were acquired using a FEI Magellan 400 XHR system equipped with an Oxford Instruments EDS detector (80 mm^2, AZtec software). Before imaging, samples were sputter-coated with $\sim$5 nm of iridium. Accelerating voltages of incident electron beams ranged from 15 kV to 30 kV and probe currents ranged from 0.4 nA to 6.4 nA. All SEM specimens were mounted on stainless stubs and held by carbon tape.

Atomic force microscopy (AFM) data was collected using an Asylum Research, MFP-3D

AFM equipped with Olympus, AC160TS tips in a laboratory air ambient.

Grazing incidence x-ray diffraction (GIXRD) patterns were collected using a Rigaku Smart-lab X-ray diffractometer in parallel beam geometry with a fixed incident angle of 0.3°. The Cu Kα x-ray generator was operated at 40 kV and 44 mA.

4.3   Results and Data

4.3.1   Prior measurements and calculations of Li$_x$Nb$_2$O$_5$ conductivity.

The conductivity of Nb$_2$O$_5$ has been proposed to change as the material is lithiated. The model pseudocapacitive material RuO$_2$ is very conductive yet Nb$_2$O$_5$, which is very insulating with bulk conductivity of $\sim$3.3 x 10^{-5} S/cm, can reach similar lithium energy storage capacities. This raises the question of changes in conductivity during lithiation.[8,120] What is already known about the electrical conductivity of Li$_x$Nb$_2$O$_5$? Nb$_2$O$_5$ ($x = 0$) is a d^0 transition metal oxide with a band gap, E_g, of 3.7 eV (measured by UPS)[159] or 3.2 - 4.0 eV (measured optically) or 2.0 - 4.0 eV (calculated).[159–162] Low values of E_g within this range are attributed to systematic underestimation of band-gaps by density functional theory (DFT) calculations employing functionals of the generalized gradient approximation (GGA) type.[159,160] Recent DFT calculations using the HSE06 functional[162] produce higher estimates of E_g (indirect) = 4.05 eV for the orthorhombic polymorph. Based upon these more accurate calculations, Nb$_2$O$_5$ is expected to be an insulator. DFT further predicts[159,160] that the reduction of Nb centers from +5 to +4 with lithiation causes n-doping as half-filled Nb-4g states at the conduction band edge are filled and their energy shifts lower. This reduction is predicted by DFT to produce a metallic lithiated state. While DFT calculations do not predict numerical values for the conductivity, these calculations predict that the electrical

conductivity will increase dramatically with lithiation as insulating Nb_2O_5 is converted into metallic $Li_xNb_2O_5$.[159–162]

In-situ measurements of σ for $Li_xNb_2O_5$ have not been reported previously to our knowledge. However, some *ex-situ* data are the following. Direct measurement of σ for bulk Nb_2O_5 samples yields 3.3×10^{-5} S/cm.[120] It's been proposed that electrons in Nb^{4+} ions are more mobile than those in Nb^{5+} ions, so as the material is reduced at negative potentials, the material becomes more conductive.[60] Reduction of Nb_2O_5 to produce oxygen vacancies and a stoichiometry of $Nb_2O_{4.96}$ produces metallic material with a conductivity at least 5 orders of magnitude higher than Nb_2O_5.[120] These data are not specific to the orthorhombic polymorph. Numerical data for σ have also been reported for the monoclinic polymorph, H-Nb_2O_5 which has $\sigma = 3 \times 10^{-6}$ S/cm whereas reduction to $Nb_2O_{4.978}$ increases σ to 3×10^3 S/cm - or nine orders of magnitude.[163] Several prior experiments also provide evidence that the σ of $Li_xNb_2O_5$ increases with lithiation without providing numerical measurements of its value. EIS measurements before and after lithiation were able to observe a three order of magnitude increase in conductivity in lithiated T-Nb_2O_5 versus pristine T-Nb_2O_5.[8] ^{7}Li NMR data[13] for $Li_xNb_2O_5$ with $x = 0.44$ and 1.86 is interpreted in terms of an increase in σ with x. In investigations of the electrochromism of Nb_2O_5 films[164] associated with the lithiation process, the kinetics and reversibility of the color change has been observed to be enhanced for lithiated films.[164]

4.3.2   Nanoribbon Electrophoretic Deposition

Like the EPD thin films studied in previous work,[12,165] the EPD NRs have incredibly reproducible electrochemistry that strong resemble the patterns seen in the thin films (Figure 4.3). In comparing the cyclic voltammetry of the Nb_2O_5 colloidal solution using FTO as the working electrode (Figure 4.3a) versus the LPNE processed Ni (Figure 4.3b), few differences are

seen, especially after the first scan once the surface has been stabilized. Most notably, both CVs exhibit a large decrease in current after ∼-1 V. Naturally, the magnitude of currents observed for the NRs is much smaller than that of the thin films due to the much smaller exposed conductive surface area of the LPNE Ni edges. Although the conductive surfaces used for EPD is very different, the overall interactions between the colloidal solution and the working electrode are very similar, so the NRs can be good models for the thin films. One difference to keep in mind is the filtering effect of the LPNE trenches. Previous work showed a strong distribution of 30 nm and 1000 nm colloids in the plating solution.[12] While the thin film can accept colloids of any size, the NRs are only composed of the colloids less than 60 nm in diameter, or the height of the trench. Thus, while the thin films have a signature pebbly texture, the NRs will have a smoother texture.

In chronoamperograms of EPD deposition, the same relatively flat current profile is seen between the thin film EPD and the nanoribbon EPD, with the only difference being the magnitude of the current, understandably due to the the differences in surface area (Figure 4.3c). Moreover, the current profiles for EPD NRs for varying depositions times: 50 s, 100 s, and 500 s, are very reproducible. When NRs width for each deposition time is measured with SEM and plotted versus time, there is almost a linear relationship between the nanoribbon width and the deposition time (Figure 4.3d). The average widths of the NRs were 110 nm, 180 nm, and 600 nm for 50 s, 100 s, and 500 s respectively. At longer deposition times, it seems the relationship begins to deviate from linearity, possibly due to the low conductivity of the NRs impeding further depositions as the NRs get wider. For conductivity measurements, 500 s was used as the deposition time as it produced the most stable NRs.
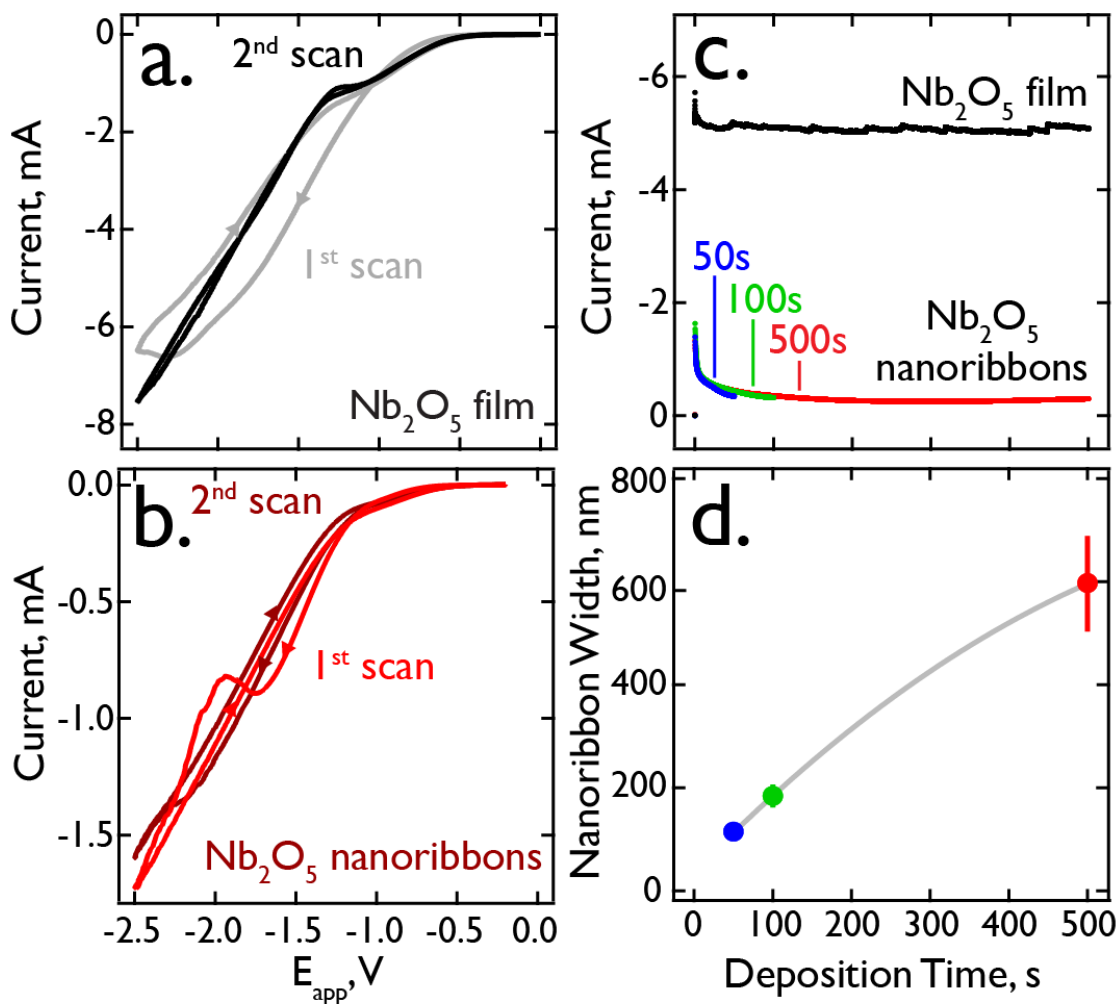
Figure 4.3: T-Nb_2O_5 Nanoribbon Electrophoretic Deposition. Cyclic voltammograms of Nb_2O_5 colloid solution with respect to (a) a 0.6 $\times$ 0.6 cm square FTO as the electrode vs. (b) LPNE Ni edges as the electrode. (c) Comparison of chronoamperometry profiles of thin film deposition for 500 s and NR depositions for 50 s, 100 s, and 500 s. (d) Average nanoribbon width with error measured from SEM images as a function of deposition time, 50 s (blue), 100 s (green), and 500 s (red). Low error bars for 50 s and 100 s are included but are not visible.

4.3.3 Confirmation of Orthorhombic Phase

The importance of the crystal structure of Nb_2O_5 with respect to lithium insertion has been extensively studied. While Nb_2O_5 can take on several crystal structures, the most efficient

for lithium storage is the orthorhombic structure.[8,11,13] As the lithium dynamics are strongly dependent on the crystal structure, it is crucial to ensure the NRs are in the orthorhombic phase. To confirm the crystal structure of the niobium oxide NRs, grazing incidence XRD (GIXRD) was performed on the bare NRs. Due to the small dimensions of the wires (20 nm x 600 nm), the signal intensity was low and reflections greater than 40 degrees are lost in the noise. Still, the reflections observed were representative of T-Nb_2O_5 (Figure 4.4, red). In order to observe a higher diffraction intensity, Au@Nb_2O_5 core-shell nanowires were also fabricated via a similar method to the NRs. Gold was electrodeposited into the LPNE Ni undercut and then partially exposed by removing PR and Ni. EPD was performed to coat the exposed gold nanowires with the Nb_2O_5 colloids and the wires were annealed at 600^oC in air. The resulting gold core was approximately 40 nm x 200 nm x 2 cm and the Nb_2O_5 shell was approximately hemispherical and 150 nm thick. Here, the presence of characteristic T-Nb_2O_5 is more defined and confirms fabrication of the orthorhombic crystal structure (Figure 4.4, green).
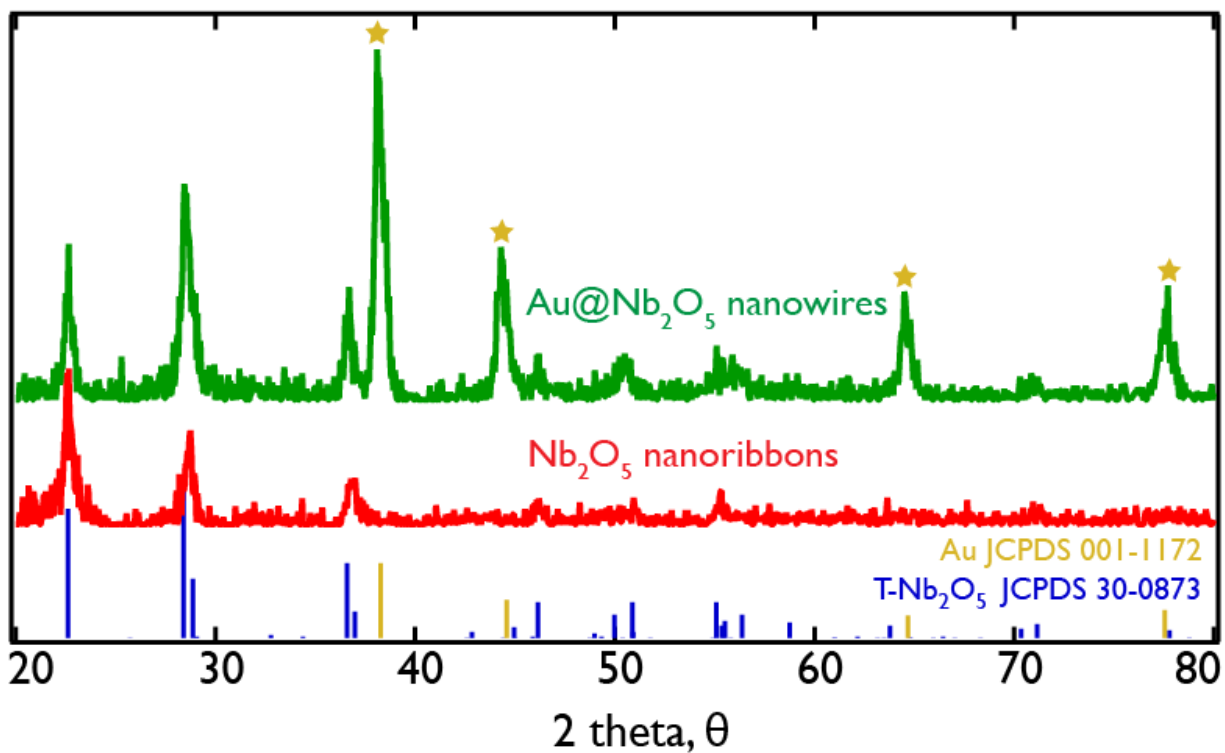
Figure 4.4: X-ray Diffraction of Nb_2O_5 NRs (red) and core-shell $Au@Nb_2O_5$ nanowires (green). Orthorhombic Nb_2O_5 reflections are shown in blue according to JCPDS 30-0873. Gold reflections are marked with a star and correspond to JCPDS 01-1172. Both data have had background subtracted.

4.3.4 Cyclic Voltammetry

In order to compare cyclic voltammetry performed in this work to literature, the studied potentials had to be converted to reference the Li/Li^+ redox couple. A small amount of ferrocene powder was added to the 1 M $LiClO_4$/PC solution and the redox electrochemistry was measured with a gold working electrode, glossy carbon rod counter, and Pt wire QRE (Figure 4.5a, inset). The $E_{p/2}$ for ferrocene versus the Pt QRE was compared to that of ferrocene in a similar high concentration Li salt in carbonate solvent solution and used to calibrate the potentials.[110,158]

Before lithiation and conductance measurements are taken, CVs at differing scan rates must be collected to confirm the proper lithiation profile of the T-Nb_2O_5 NRs. Characteristic T-Nb_2O_5 lithium electrochemistry is defined by the presence of two broad lithiation peak between 1.2 V and 2.2 V and a broad delithiation peak between 1.5 V and 1.8 V at 10 mV/s, all referenced versus the Li/Li$^+$ redox couple .[8,11] Our previous work with EPD films showed similar electrochemistry with a broad lithiation peak centered around 2.0 V and a broad delithiation peak centered around 2.3 V for a 5 mV/s scan rate.[12] Several factors can interfere with the Nb_2O_5 electrochemistry in samples of this scale and are easily identified in this first CV step.

Improper insulation of the gold contacts is the main source of interfering electrochemistry. On a control sample of exposed gold contacts, signature gold/lithium electrochemistry can be identified in comparison to the work by Moshkovich et al. (Figure 4.5a).[166] Identification of gold exposure can be seen at 0 V and 0.5 V were bulk Li deposition is seen marked by sharp deposition and stripping waves. Additionally, Li underpotential deposition waves can be identified at approximately 0.5 V and 1.0 V. While these peaks are outside of the lithiation potential window for niobium oxide, they can be used to identify interfering gold electrochemistry and confirm calibration of the Pt QRE. To confirm that the gold contacts could be sufficiently insulated with SU-8 PR, a control of just covered gold contacts with no Nb_2O_5 NRs was studied (Figure 4.5b, red). The CV shows low current in the pA range which notes that the gold contacts are fully insulated and do not contribute to the electrochemistry of the device.

Other notable interfering waves are attributed to water and oxygen contamination in the electrolyte solution, but these peaks can also be seen when gold is insulated due to their reaction with Nb_2O_5. The interference of oxygen is particularly insidious since an oxygen reduction wave centered within 1.8 - 2.2 V can be mistaken for a lithiation wave which is typically seen between 1.2 - 2.2 V. At 1 mV/s, these waves can be deconvoluted as an oxygen
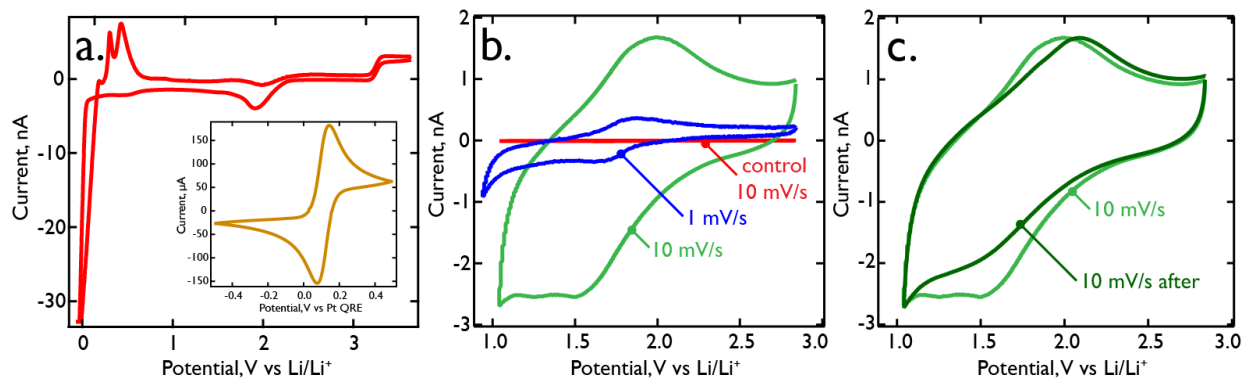
Figure 4.5: Cyclic Voltammetry of T-Nb$_2$O$_5$ NRs. (a) Cyclic voltammogram of a control sample of exposed gold contacts with no NRs. Expanded window is shown to locate possible interfering gold electrochemistry. Potentials have been converted to a lithium reference electrode using ferrocene as shown in the inset. (b) Cyclic voltammetry of T-Nb$_2$O$_5$ NRs at 10 mV/s (green) and 1 mV/s (blue). The presence of reversible electrochemistry at both scan rates shows little interference from water or oxygen. CVs of a control with no NRs and insulated gold contacts at 10 mV/s in red shows the insulated contacts add negligible current. (c) Electrochemistry of NRs before (light green) and after (dark green) conductivity experiments indicates little degradation of the NRs during conductivity measurements.

reduction wave will be grossly irreversible as this slow scan rate.

When the contacts are properly insulated and the electrolyte solution water/oxygen free, CVs similar to those of literature and previous T-Nb$_2$O$_5$ EPD thin films at low scan rates are observed (Figure 4.5b, blue and green).[12] One interesting feature of the Nb$_2$O$_5$ electrochemistry is the size of the capacitive envelope before and after lithiation. This is both seen in literature and is especially noticeably in the 1 mV/s CV of the Nb$_2$O$_5$ NRs (Figure 4.5b, blue). At potentials greater than 2.2 V, the capacitive envelope is very narrow but at potentials less than 1.5 - 1.8 V, the capacitive envelope is significantly greater. This hints at a increase in conductivity in Nb$_2$O$_5$ which allows for more capacitive contributions to the current. CVs were also compared before and after a full set of conductivity measurements (Figure 4.5c). Little change in the CVs notes that no significant degradation occurred during the measurements that could have contributed to the measured conductivity values.

4.3.5 Determination of Conductivity as a Function of Potential

Conductivity of the material can be calculated by treating each individual wire as a resistor. From the I-V curves, the slope gives the conductance, $G = \frac{1}{R} = \frac{I}{V}$, from Ohm's Law, $V = IR$. Using the relationship between resistance, R, and resistivity, ρ, an equation can be derived for conductivity, σ, as a function of the conductance, G:

$$\sigma = G * \frac{l}{A} \tag{4.1}$$

where l is the length of the wire and A is the cross-sectional area of the ribbon, $w \times h$. The conductivity of the device is directly related to the slope. There are N NRs in a device which can be treated resistors in parallel to extract the resistance through each ribbon, R_i, from the total measured resistance, R_T.

$$\frac{1}{R_T} = \frac{1}{R_1} + \frac{1}{R_2} + ... + \frac{1}{R_N} = N * \frac{1}{R_i} \tag{4.2}$$

Using the inverse relationship between R and G, the total conductance measured, G_T, can be related to the conductance of a single ribbon, G_i,

$$G_T = N * G_i \tag{4.3}$$

and used to calculate the conductivity of a single ribbon, σ_i:

$$\sigma_i = \frac{G_T}{N} * \frac{l}{A} \tag{4.4}$$

Upon SEM examination of the device, 191 of the originally 200 nanowires were active in the measurements and this was taken into consideration in the calculations. SEM is also used to measure the length of exposed nanoribbon and the width to calculate the cross-sectional
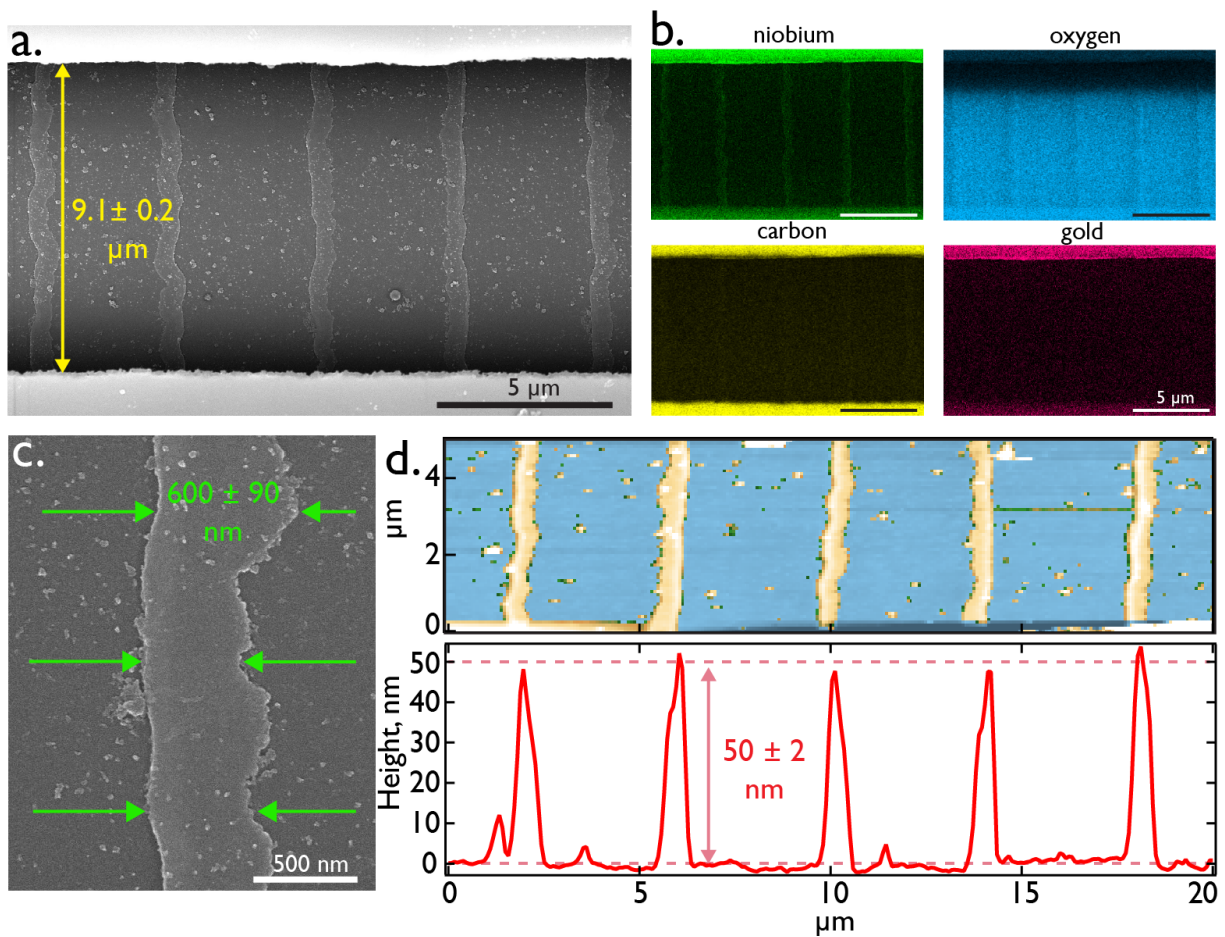
Figure 4.6: SEM, EDS, and AFM Measurements of T-Nb$_2$O$_5$ Nanoribbon Dimensions. (a) SEM image of the device displaying several NRs and the PR covered contacts. The average exposed length of NRs is 9.1 ± 0.2 μm. (b) EDS images of (a) highlighting niobium L$_{\alpha 1}$ and oxygen K$_{\alpha 1}$ confirming the presence of Nb$_2$O$_5$ and carbon K$_{\alpha 1}$ and gold L$_{\alpha 1}$ highlighting the PR covered gold contacts. (c) SEM image of a single nanoribbon from a 500 s deposition. The average width is 600 ± 90 nm. (d) AFM heat map and line scan of several Nb$_2$O$_5$ NRs. The average height is 50 ± 2 nm.

area of the ribbon. On average, 9.1 ± 0.2 μm of wire are exposed (Figure 4.6a). Due to the thickness of the SU-8 insulating layer, it is difficult to distinguish the gold contacts and the PR in SEM images. EDS of carbon and gold can be used to see that the SU-8 covers the gold contacts very well and extends very minimally past the gold to expose as much length of the nanowires as possible (Figure 4.6b). Additionally, EDS of niobium and oxygen clearly highlights the observed nanoribbons confirming an absence of impurities in the NRs. At higher magnification, the NRs are measured to be 600 ± 90 nm wide on average (Figure 4.6a,c). The height of the NRs is limited by the 60 nm thickness of the sacrificial nickel layer in the fabrication procedure. This can be measured accurately with AFM which shows an average nanoribbon height of 50 ± 2 nm (Figure 4.6d).

Chronoamperometry was used to lithiate the NRs. Starting at a delithiated potential (2.84 V), the potential was increase incrementally by 0.2 V until the most lithiated potential was reached (1.24 V) (Figure 4.7a). Potentials beyond that range were explored but were not included due to potential reduction of niobium to the +3 oxidation state below 1.24 V and increasing anodic current above 2.84 V that strayed from literature behavior. Regardless, the range of potentials chose included a fully delithiated state, a fully lithiated state, and several intermediate lithiation states. For each potential, the NRs were held at the fixed potential for 150 s to reach equilibration, apparent by the negligible current by 150 s (Figure 4.7a).

Immediately after each lithiation, the contacts were arranged to two electrode mode where one gold contact was the working electrode and the other was the counter/reference electrode. I-V curves were measured across a 10 mV window at 0.2 mV/s. The results resembled resistor I-V curves with the slope corresponding to the conductance (Figure 4.7b). As the NRs were equilibrated to increasingly more lithiated potentials, the slope of the I-V curves increased incrementally. The same phenomenon was observed up delithiation where the slopes of the I-V curves decreased incrementally. After each conductance measurement, the contacts were

returned to three electrode mode to equilibrate at the next potential in the sequence. Using the dimensions of the NRs, the conductance values were converted to conductivity values by Equation 4.4.
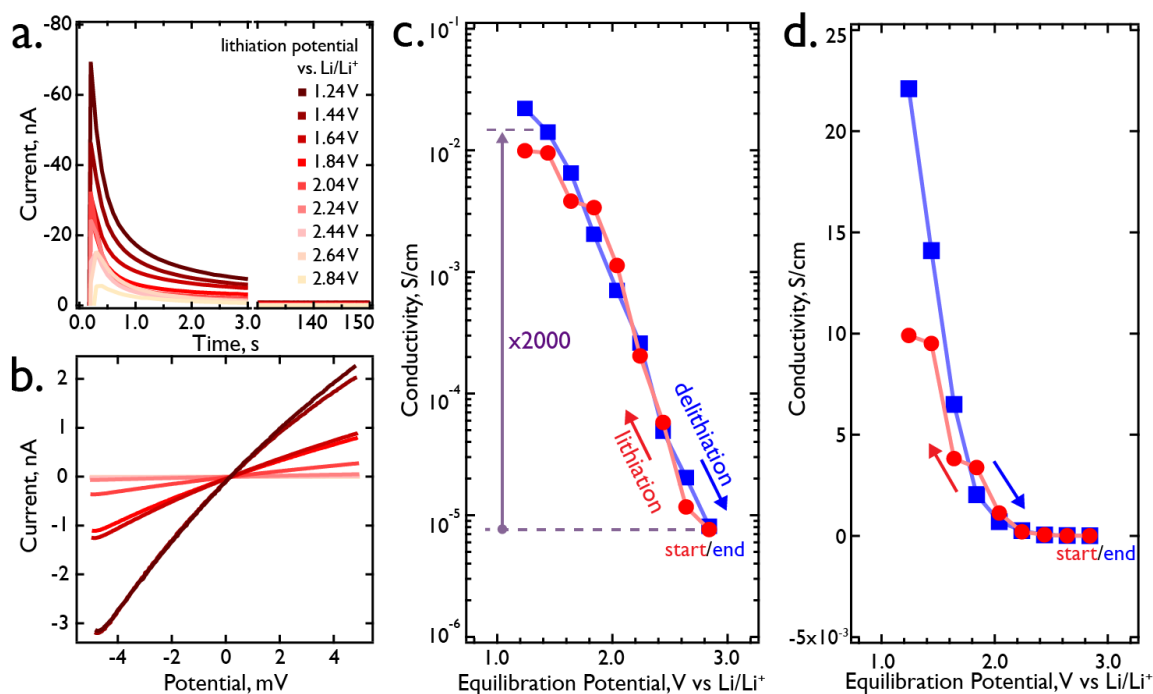
Figure 4.7: Equilibration and Conductivity Measurements of T-Nb_2O_5. (a) Equilibration current profiles at various potentials. Current is shown be negligible by 150 s. (b) Current-voltage (I-V) plots of the NRs after lithiation at the potentials shown in (a). (c & d) Conductivity calculated from the dimensions of the wires and the conductance measured from the slopes in (b) (logarithmic & linear scale) plotted as a function of lithiation. An increase in conductivity is seen as lithium is inserted (red) into the NRs that is reversible upon delithiation (blue).

When the conductivity of the NRs is plotted as a function of the lithiation potential, there is a 3.3 order of magnitude difference between the NRs in the lithiated versus delithiated state (Figure 4.7c). This corresponds well with previous research suggesting that the conductivity of Nb_2O_5 increases by 3-4 orders of magnitude with lithiation.[8] A sharp increase in the conductivity can be seen between 2.04 V and 1.44 V which corresponds to the lithiation wave at the slower scan rates indicating that the lithium is responsible for the increase in conductiv-

ity (Figure 4.7d). Conversely, the conductivity decreases drastically between 1.04 - 2.04 V, which encapsulates the delithiation peak, supporting this hypothesis. The reversibility of the lithiation and delithiation is also incredibly reproducible with the delithiation conductivity at each potential returning to almost the same value as the lithiation conductivity.

4.4 Conclusions

The LPNE technique for fabricating nanoribbons on sacrificial conductive edges was explored with EPD of Nb_2O_5. This was shown to have comparable deposition characteristics as thin film EPD, allowing for direct comparison of behaviors observed in NRs to those of the thin films. Mainly, this fabrication technique allowed for an *in-situ* investigation into the conductivity of electrodeposited TMOs as a function of lithium insertion. LPNE was used to fabricate an array of 200 NRs with controllable dimensions contacted across two gold contacts. Lithium intercalation was conducted by using both contacts as a working electrode and then I-V curves were measured by using one contact as the working electrode and the other as the counter/reference electrode to determine conductivity through the wire. Starting at T-Nb_2O_5 in the fully delithiated state, the conductivity of 7.3 x 10^{-6} S/cm experienced an increase of 3.3 orders of magnitude to 0.015 S/cm upon full lithiation. The greatest change in conductivity was observed at the potentials corresponding to lithium insertion and deinsertion in the CVs supporting the hypothesis that the lithium strongly changes the conductivity of T-Nb_2O_5.

Bibliography

[1] Whittingham, M. S. Electrical Energy Storage and Intercalation Chemistry. *Science* **1976**, *192*, 1126–1127.

[2] Deng, D. Li-Ion Batteries: Basics, Progress, and Challenges. *Energy Sci. Eng.* **2015**, *3*, 385–418.

[3] Goodenough, J. B. How We Made the Li-Ion Rechargeable Battery. *Nat. Electron.* **2018**, *1*, 204–204.

[4] Simon, P.; Gogotsi, Y. Materials for Electrochemical Capacitors. *Nat. Mater.* **2008**, *7*, 845–854.

[5] Simon, P.; Gogotsi, Y. Perspectives for Electrochemical Capacitors and Related Devices. *Nat. Mater.* **2020**, *19*, 1151–1163.

[6] Augustyn, V.; Simon, P.; Dunn, B. Pseudocapacitive Oxide Materials for High-Rate Electrochemical Energy Storage. *Energy Environ. Sci.* **2014**, *7*, 1597.

[7] Choi, C.; Ashby, D. S.; Butts, D. M.; DeBlock, R. H.; Wei, Q.; Lau, J.; Dunn, B. Achieving High Energy Density and High Power Density with Pseudocapacitive Materials. *Nat. Rev. Mater.* **2020**, *5*, 5–19.

[8] Kim, J. W.; Augustyn, V.; Dunn, B. The Effect of Crystallinity on the Rapid Pseudocapacitive Response of Nb_2O_5. *Adv. Energy Mater.* **2012**, *2*, 141–148.

[9] Wang, J.; Polleux, J.; Lim, J.; Dunn, B. Pseudocapacitive Contributions to Electrochemical Energy Storage in TiO_2 (Anatase) Nanoparticles. *J Phys Chem C* **2007**, *111*, 14925–14931.

[10] Brousse, T.; Bélanger, D.; Long, J. W. To Be or Not To Be Pseudocapacitive? *J. Electrochem. Soc.* **2015**, *162*, A5185–A5189.

[11] Augustyn, V.; Come, J.; Lowe, M. A.; Kim, J. W.; Taberna, P.-L.; Tolbert, S. H.; Abruña, H. D.; Simon, P.; Dunn, B. High-Rate Electrochemical Energy Storage through Li^+ Intercalation Pseudocapacitance. *Nat. Mater.* **2013**, *12*, 518–522.

[12] Jha, G.; Tran, T.; Qiao, S.; Ziegler, J. M.; Ogata, A. F.; Dai, S.; Xu, M.; Le Thai, M.; Chandran, G. T.; Pan, X.; Penner, R. M. Electrophoretic Deposition of Mesoporous Niobium(V) Oxide Nanoscopic Films. *Chem. Mater.* **2018**, *30*, 6549–6558.

[13] Griffith, K. J.; Forse, A. C.; Griffin, J. M.; Grey, C. P. High-Rate Intercalation Without Nanostructuring in Metastable Nb_2O_5 Bronze phases. *J. Am. Chem. Soc.* **2016**, *138*, 8888–8899.

[14] Kong, L.; Zhang, C.; Wang, J.; Qiao, W.; Ling, L.; Long, D. Nanoarchitectured Nb_2O_5 Hollow, Nb_2O_5@Carbon and NbO_2@Carbon Core-Shell Microspheres for Ultrahigh-Rate Intercalation Pseudocapacitors. *Sci. Rep.* **2016**, *6*, 21177.

[15] Zhang, C.; Maloney, R.; Lukatskaya, M.; Beidaghi, M.; Dyatkin, B.; Perre, E.; Long, D.; Qiao, W.; Dunn, B.; Gogotsi, Y. Synthesis and Electrochemical Properties of Niobium Pentoxide Deposited on Layered Carbide-Derived Carbon. *J. Power Sources* **2015**, *274*, 121–129.

[16] Wang, X.; Li, G.; Chen, Z.; Augustyn, V.; Ma, X.; Wang, G.; Dunn, B.; Lu, Y. High-Performance Supercapacitors Based on Nanocomposites of Nb_2O_5 Nanocrystals and Carbon Nanotubes. *Adv. Energy Mater.* **2011**, *1*, 1089–1093.

[17] Rahman, M. M.; Rani, R. A.; Sadek, A. Z.; Zoolfakar, A. S.; Field, M. R.; Ramireddy, T.; Kalantar-Zadeh, K.; Chen, Y. A Vein-Like Nanoporous Network of Nb_2O_5 with a Higher Lithium Intercalation Discharge Cut-Off Voltage. *J. Mater. Chem. A.* **2013**, *1*, 11019–11025.

[18] Asselin, E.; Ahmed, T. M.; Alfantazi, A. Corrosion of Niobium in Sulphuric and Hydrochloric Acid Solutions at 75 and 95°C. *Corros. Sci.* **2007**, *49*, 694–710.

[19] Zhitomirsky, I. Electrolytic Deposition of Niobium Oxide Films. *Mater. Lett.* **1998**, *35*, 188–193.

[20] Zhitomirsky, I. Cathodic Electrosynthesis of Titania Films and Powders. *Nanostructured Mater.* **1997**, *8*, 521–528.

[21] Zhitomirsky, I. Electrolytic Deposition of Oxide Films in the Presence of Hydrogen Peroxide. *J. Eur. Ceram.* **1999**, *19*, 2581–2587.

[22] Nitta, N.; Yushin, G. High-Capacity Anode Materials for Lithium-Ion Batteries: Choice of Elements and Structures for Active Particles. *Part. Part. Syst. Charact.* **2014**, *31*, 317.

[23] Goodenough, J. B.; Park, K.-S. The Li-Ion Rechargeable Battery: A Perspective. *J. Am. Chem. Soc.* **2013**, *135*, 1167.

[24] Wood, D. L.; Li, J.; Daniel, C. Prospects for Reducing the Processing Cost of Lithium Ion Batteries. *J. Power Sources* **2015**, *275*, 234.

[25] Andre, D.; Hain, H.; Lamp, P.; Maglia, F.; Stiaszny, B. Future High-Energy Density Anode Materials from an Automotive Application Perspective. *J. Mater. Chem. A* **2017**, *5*, 17174.

[26] Armand, M.; Tarascon, J.-M. Building Better Batteries. *Nature* **2008**, *451*, 652.

[27] Arora, P.; Zhang, Z. Battery Separators. *Chem. Rev.* **2004**, *104*, 4419.

[28] Myung, S. T.; Maglia, F.; Park, K. J.; Yoon, C. S.; Lamp, P.; Kim, S. J.; Sun, Y. K. Nickel-Rich Layered Cathode Materials for Automotive Lithium-Ion Batteries: Achievements and Perspectives. *ACS Energy Lett.* **2017**, *2*, 196.

[29] Lee, J. H.; Yoon, C. S.; Hwang, J.-Y.; Kim, S.-J.; Maglia, F.; Lamp, P.; Myung, S.-T.; Sun, Y.-K. High-Energy-Density Lithium-Ion Battery Using a Carbon-Nanotube–Si Composite Anode and a Compositionally-Graded $Li[Ni_{0.85}Co_{0.05}Mn_{0.10}]O_2$ Cathode. *Energy Environ. Sci.* **2016**, *9*, 2152.

[30] Golubkov, A. W.; Fuchs, D.; Wagner, J.; Wiltsche, H.; Stangl, C.; Fauler, G.; Voitic, G.; Thaler, A.; Hacker, V. Thermal-Runaway Experiments on Consumer Li-Ion Batteries with Metal-Oxide and Olivin-Type Cathodes. *RSC Adv.* **2014**, *4*, 3633.

[31] Liu, W.; Oh, P.; Liu, X.; Lee, M.-J.; Cho, W.; Chae, S.; Kim, Y.; Cho, J. Nickel-Rich Layered Lithium Transition-Metal Oxide for High-Energy Lithium-Ion Batteries. *Angew. Chem., Int. Ed.* **2015**, *54*, 4440.

[32] Xu, B.; Qian, D.; Wang, Z.; Meng, Y. S. Recent Progress in Cathode Materials Research for Advanced Lithium Ion Batteries. *Mater. Sci. Eng., R* **2012**, *73*, 51.

[33] Yan, J.; Liu, X.; Li, B. Recent Progress in Li-Rich Layered Oxides as Cathode Materials for Li-Ion Batteries. *RSC Adv.* **2014**, *4*, 63268.

[34] Whittingham, M. S. Lithium Batteries and Cathode Materials. *Chem. Rev.* **2004**, *104*, 4271.

[35] Fergus, J. W. Recent Developments in Cathode Materials for Lithium Ion Batteries. *J. Power Sources* **2010**, *195*, 939.

[36] Ellis, B. L.; Lee, K. T.; Nazar, L. F. Positive Electrode Materials for Li-Ion and Li-Batteries. *Chem. Mater.* **2010**, *22*, 691.

[37] Brandt, K. Historical Development of Secondary Lithium Batteries. *Solid State Ionics* **1994**, *69*, 173.

[38] Basu, S. Ambient Temperature Rechargeable Battery. US Patent Appl. 4423125, 1983.

[39] Basu, S. Rechargeable battery. US Patent Appl. 4304825, 1981.

[40] Agubra, V.; Fergus, J. Lithium Ion Battery Anode Aging Mechanisms. *Materials* **2013**, *6*, 1310.

[41] An, S. J.; Li, J.; Daniel, C.; Mohanty, D.; Nagpure, S.; Wood, D. L. The State of Understanding of the Lithium-Ion-Battery Graphite Solid Electrolyte Interphase (SEI) and Its Relationship to Formation Cycling. *Carbon* **2016**, *105*, 52.

[42] Shi, Q.; Liu, W.; Qu, Q.; Gao, T.; Wang, Y.; Liu, G.; Battaglia, V. S.; Zheng, H. Robust Solid/Electrolyte Interphase on Graphite Anode to Suppress Lithium Inventory Loss in Lithium-Ion Batteries. *Carbon* **2017**, *111*, 291.

[43] Ng, S. H.; Vix-Guterl, C.; Bernardo, P.; Tran, N.; Ufheil, J.; Buqa, H.; Dentzer, J.; Gadiou, R.; Spahr, M. E.; Goers, D.; Novák, P. Correlations between Surface Properties of Graphite and the First Cycle Specific Charge Loss in Lithium-Ion Batteries. *Carbon* **2009**, *47*, 705.

[44] Joho, F.; Rykart, B.; Blome, A.; Novák, P.; Wilhelm, H.; Spahr, M. E. Relation between Surface Properties, Pore Structure and First-Cycle Charge Loss of Graphite as Negative Electrode in Lithium-Ion Batteries. *J. Power Sources* **2001**, *97–98*, 78.

[45] Zhang, S. S. A Review on Electrolyte Additives for Lithium-Ion Batteries. *J. Power Sources* **2006**, *162*, 1379.

[46] Wang, H.; Wang, F. Electrochemical Investigation of an Artificial Solid Electrolyte Interface for Improving the Cycle-Ability of Lithium Ion Batteries Using an Atomic Layer Deposition on a Graphite Electrode. *J. Power Sources* **2013**, *233*, 1.

[47] Komaba, S.; Watanabe, M.; Groult, H.; Kumagai, N. Alkali Carbonate-Coated Graphite Electrode for Lithium-Ion Batteries. *Carbon* **2008**, *46*, 1184.

[48] Bugga, R. V.; Smart, M. C. Lithium Plating Behavior in Lithium-Ion Cells. *ECS Trans.* **2009**, *25*, 241.

[49] Smart, M. C.; Ratnakumar, B. V. Effects of Electrolyte Composition on Lithium Plating in Lithium-Ion Cells. *J. Electrochem. Soc.* **2011**, *158*, A379.

[50] Tarascon, J. M.; Armand, M. Issues and Challenges Facing Rechargeable Lithium Batteries. *Nature* **2001**, *414*, 359.

[51] Zhao, B.; Ran, R.; Liu, M.; Shao, Z. A Comprehensive Review of $Li_4Ti_5O_{12}$-Based Electrodes for Lithium-Ion Batteries : The Latest Advancements and Future Perspectives. *Mater. Sci. Eng., R* **2015**, *98*, 1.

[52] Ohzuku, T.; Ueda, A.; Yamamota, N. Zero-Strain Insertion Material of $Li[Li_{1/3}Ti_{5/3}]O_4$ for Rechargeable Lithium Cells. *J. Electrochem. Soc.* **1995**, *142*, 1431.

[53] Chen, C. H.; Vaughey, J. T.; Jansen, A. N.; Dees, D. W.; Kahaian, A. J.; Goacher, T.; Thackeray, M. M. Studies of Mg-Substituted $Li_{4-x}Mg_xTi_5O_{12}$ Spinel Electrodes ($0 \leq x \leq 1$) for Lithium Batteries. *J. Electrochem. Soc.* **2001**, *148*, A102.

[54] Van Der Ven, A.; Marianetti, C.; Morgan, D.; Ceder, G. Phase Transformations and Volume Changes in Spinel $Li_xMn_2O_4$. *Solid State Ionics* **2000**, *135*, 21.

[55] Chen, Z.; Belharouak, I.; Sun, Y.; Amine, K. Titanium-Based Anode Materials for Safe Lithium-Ion Batteries. *Adv. Funct. Mater.* **2013**, *23*, 959.

[56] Myung, S.; Takahashi, N.; Komaba, S.; Yoon, C. S.; Sun, Y.; Amine, K.; Yashiro, H. Nanostructured TiO_2 and Its Application in Lithium-Ion Storage. *Adv. Funct. Mater.* **2011**, *21*, 3231.

[57] Dambournet, D.; Chapman, K. W.; Chupas, P. J.; Gerald, R. E.; Penin, N.; Labrugere, C.; Demourgues, A.; Tressaud, A.; Amine, K. Dual Lithium Insertion and Conversion Mechanisms in a Titanium-Based Mixed-Anion Nanocomposite. *J. Am. Chem. Soc.* **2011**, *133*, 13240.

[58] Jung, H.; Oh, S. W.; Ce, J.; Jayaprakash, N.; Sun, Y. Mesoporous TiO_2 Nano Networks: Anode for High Power Lithium Battery Applications. *Electrochem. Commun.* **2009**, *11*, 756.

[59] Xu, W.; Luo, H.; Chen, G.; Zou, G.; Rui, X.; Yan, L. Recent Advances in Nanostructured Nb-Based Oxides for Electrochemical Energy Storage. *Nanoscale* **2016**, *8*, 8443.

[60] Ohzuku, T.; Sawai, K.; Hirai, T. Electrochemistry of L-Niobium Pentoxide a Lithium/Non-Aqueous Cell. *J. Power Sources* **1987**, *19*, 287.

[61] Han, J.; Liu, D.; Song, S.; Kim, Y.; Goodenough, J. B. Lithium Ion Intercalation Performance of Niobium Oxides: KNb_5O_{13} and $K_6Nb_{10.8}O_{30}$. *Chem. Mater.* **2009**, *21*, 4753.

[62] Han, J.; Huang, Y.; Goodenough, J. B. New Anode Framework for Rechargeable Lithium Batteries. *Chem. Mater.* **2011**, *23*, 2027.

[63] Wei, M.; Wei, K.; Ichihara, M.; Zhou, H. Nb_2O_5 Nanobelts : A Lithium Intercalation Host with Large Capacity and High Rate Capability. *Electrochem. Commun.* **2008**, *10*, 980.

[64] Lubimtsev, A. A.; Kent, P. R. C.; Sumpter, B. G.; Ganesh, P. Understanding the Origin of High-Rate Intercalation Pseudocapacitance in Nb2O5 Crystals. *J. Mater. Chem. A* **2013**, *1*, 14951.

[65] Come, J.; Augustyn, V.; Kim, J. W.; Rozier, P.; Taberna, P.-L.; Gogotsi, P.; Long, J. W.; Dunn, B.; Simon, P. Electrochemical Kinetics of Nanostructured Nb_2O_5 Electrodes. *J. Electrochem. Soc.* **2014**, *161*, A718–A725.

[66] Zhang, C.; Beidaghi, M.; Naguib, M.; Lukatskaya, M. R.; Zhao, M.-Q.; Dyatkin, B.; Cook, K. M.; Kim, S. J.; Eng, B.; Xiao, X.; Long, D.; Qiao, W.; Dunn, B.; Gogotsi, Y. Synthesis and Charge Storage Properties of Hierarchical Niobium Pentoxide/Carbon/Niobium Carbide (MXene) Hybrid Materials. *Chem. Mater.* **2016**, *28*, 3937–3943.

[67] Lin, C.; Fan, X.; Xin, Y.; Cheng, F.; Lai, M. O.; Zhou, H.; Lu, L. Monodispersed Mesoporous $Li_4Ti_5O_{12}$ Submicrospheres as Anode Materials for Lithium-Ion Batteries: Morphology and Electrochemical Performances. *Nanoscale* **2014**, *6*, 6651.

[68] Lim, E.; Kim, H.; Jo, C.; Chun, J.; Ku, K.; Kim, S.; Lee, H. I.; Nam, I.-S.; Yoon, S.; Kang, K.; Lee, J. Advanced Hybrid Supercapacitor Based on a Mesoporous Niobium Pentoxide/Carbon as High- Performance Anode. *ACS Nano* **2014**, *8*, 8968.

[69] Bianchini, M.; Ateba-Mba, J. M.; Dagault, P.; Bogdan, E.; Carlier, D.; Suard, E.; Masquelier, C.; Croguennec, L. Multiple Phases in the ϵ-VPO$_4$O–LiVPO$_4$O–Li$_2$VPO$_4$O System: A Combined Solid State Electrochemistry and Diffraction Structural Study. *J. Mater. Chem. A* **2014**, *2*, 10182.

[70] Tebbe, J. L.; Holder, A. M.; Musgrave, C. B. Mechanisms of LiCoO$_2$ Cathode Degradation by Reaction with HF and Protection by Thin Oxide Coatings. *ACS Appl. Mater. Interfaces* **2015**, *7*, 24265.

[71] Zhou, Y. N.; Ma, J.; Hu, E.; Yu, X.; Gu, L.; Nam, K. W.; Chen, L.; Wang, Z.; Yang, X. Q. Tuning Charge-Discharge Induced Unit Cell Breathing in Layer-Structured Cathode Materials for Lithium-Ion Batteries. *Nat. Commun.* **2014**, *5*, 5381.

[72] Liu, H.; Strobridge, F. C.; Borkiewicz, O. J.; Wiaderek, K. M.; Chapman, K. W.; Chupas, P. J.; Grey, C. P. Capturing Metastable Structures During High-Rate Cycling of LiFePO$_4$ Nanoparticle Electrodes. *Science* **2014**, *344*, 1480.

[73] Zhou, Y. N.; Yue, J. L.; Hu, E.; Li, H.; Gu, L.; Nam, K. W.; Bak, S. M.; Yu, X.; Liu, J.; Bai, J.; Dooryhee, E.; Fu, Z. W.; Yang, X. Q. High-Rate Charging Induced Intermediate Phases and Structural Changes of Layer-Structured Cathode for Lithium-Ion Batteries. *Adv. Energy Mater.* **2016**, *6*, 1600597.

[74] Bak, S. M.; Shadike, Z.; Lin, R.; Yu, X.; Yang, X. Q. In Situ /Operando Synchrotron-Based X-Ray Techniques for Lithium-Ion Battery Research. *NPG Asia Mater.* **2018**, *10*, 563.

[75] Jensen, K. M. O.; Yang, X.; Laveda, J. V.; Zeier, W. G.; See, K. A.; Michiel, M. D.; Melot, B. C.; Corr, S. A.; Billinge, S. J. L. X-Ray Diffraction Computed Tomography for Structural Analysis of Electrode Materials in Batteries. *J. Electrochem. Soc.* **2015**, *162*, A1310.

[76] Sharma, N.; Peterson, V. K. In Situ Neutron Powder Diffraction Studies of Lithium-Ion Batteries. *J. Solid State Electrochem.* **2012**, *16*, 1849.

[77] Chen, C.-J.; Pang, W. K.; Mori, T.; Peterson, V. K.; Sharma, N.; Lee, P.-H.; Wu, S.; Wang, C.-C.; Song, Y.-F.; Liu, R.-S. The Origin of Capacity Fade in the Li$_2$MnO$_3$·LiMO$_2$ (M = Li, Ni, Co, Mn) Microsphere Positive Electrode: An Operando Neutron Diffraction and Transmission X-Ray Microscopy Study. *J. Am. Chem. Soc.* **2016**, *138*, 8824.

[78] Liu, X. H.; Huang, S.; Picraux, S. T.; Li, J.; Zhu, T.; Huang, J. Y. Reversible Nanopore Formation in Ge Nanowires during Lithiation- Delithiation Cycling: An in Situ Transmission Electron Microscopy Study. *Nano Lett.* **2011**, *11*, 3991.

[79] Huang, J. Y.; Zhong, L.; Wang, C. M.; Sullivan, J. P.; Xu, W.; Zhang, L. Q.; Mao, S. X.; Hudak, N. S.; Liu, X. H.; Subramanian, A.; Fan, H.; Qi, L.; Kushima, A.; Li, J. In Situ Observation of the Electrochemical Lithiation of a Single SnO_2 Nanowire Electrode. *Science* **2010**, *330*, 1515.

[80] Gu, M. et al. Demonstration of an Electrochemical Liquid Cell for Operando Transmission Electron Microscopy Observation of the Lithiation/Delithiation Behavior of Si Nanowire Battery Anodes. *Nano Lett.* **2013**, *13*, 6106.

[81] Wang, C.-M.; Li, X.; Wang, Z.; Xu, W.; Liu, J.; Gao, F.; Kovarik, L.; Zhang, J.-G.; Howe, J.; Burton, D. J.; Liu, Z.; Xiao, X.; Thevuthasan, S.; Baer, D. R. In Situ TEM Experiments of Electrochemical Lithiation and Delithiation of Individual Nanostructures TEM Investigation of Congruent Phase Transition and Structural Evolution of Nanostructured Silicon/Carbon Anode for Lithium Ion Batteries. *Nano Lett.* **2012**, *12*, 1624.

[82] Abellan, P.; Mehdi, B. L.; Parent, L. R.; Gu, M.; Park, C.; Xu, W.; Zhang, Y.; Arslan, I.; Zhang, J.-G.; Wang, C.-M.; Evans, J. E.; Browning, N. D. Probing the Degradation Mechanisms in Electrolyte Solutions for Li-Ion Batteries by In Situ TEM Experiments of Electrochemical Lithiation and Delithiation of Individual Nanostructures. *Nano Lett.* **2014**, *14*, 1293.

[83] Sacci, R. L.; Dudney, N. J.; More, K. L.; Parent, L. R.; Arslan, I.; Browning, N. D.; Unocic, R. R. Direct Visualization of Initial SEI Morphology and Growth Kinetics during Lithium Deposition by in Situ Electrochemical Transmission Electron Microscopy. *Chem. Commun.* **2014**, *50*, 2104.

[84] He, Y.; Piper, D. M.; Gu, M.; Travis, J. J.; George, S. M.; Lee, S.-H.; Genc, A.; Pullan, L.; Liu, J.; Mao, S. X.; Zhang, J.-G.; Ban, C.; Wang, C. In Situ TEM Experiments of Electrochemical Lithiation and Delithiation of Individual Nanostructures Transmission Electron Microscopy Probing of Native Oxide and Artificial Layers on Silicon Nanoparticles for Lithium Ion Batteries. *ACS Nano* **2014**, *8*, 11816.

[85] Wolf, M.; May, B. M.; Cabana, J. Visualization of Electrochemical Reactions in Battery Materials with X-Ray Microscopy and Mapping. *Chem. Mater.* **2017**, *29*, 3347.

[86] Ulvestad, A.; Singer, A.; Cho, H.-M.; Clark, J. N.; Harder, R.; Maser, J.; Meng, Y. S.; Shpyrko, O. G. Single Particle Nanomechanics in Operando Batteries via Lensless Strain Mapping. *Nano Lett.* **2014**, *14*, 5123.

[87] Ulvestad, A.; Cho, H. M.; Harder, R.; Kim, J. W.; Dietze, S. H.; Fohtung, E.; Meng, Y. S.; Shpyrko, O. G. Nanoscale Strain Mapping in Battery Nanostructures. *Appl. Phys. Lett.* **2014**, *104*, 073108.

[88] Luchkin, S. Y.; Romanyuk, K.; Ivanov, M.; Kholkin, A. L. Li Transport in Fresh and Aged $LiMn_2O_4$ Cathodes via Electrochemical Strain Microscopy. *J. Appl. Phys.* **2015**, *118*, 072016.

[89] Shukla, A. K.; Ramasse, Q. M.; Ophus, C.; Kepaptsoglou, D. M.; Hage, F. S.; Gammer, C.; Bowling, C.; Gallegos, P. A. H.; Venkatachalam, S. Effect of Composition on the Structure of Lithium- and Manganese-Rich Transition Metal Oxides. *Energy Environ. Sci.* **2018**, *11*, 830.

[90] Sun, H.-H.; Weeks, J. A.; Heller, A.; Mullins, C. B. Nanorod Gradient Cathode: Preventing Electrolyte Penetration into Cathode Particles. *ACS Appl. Energy Mater.* **2019**, *2*, 6002.

[91] Bond, T.; Zhou, J.; Cutler, J. Electrode Stack Geometry Changes During Gas Evolution in Pouch-Cell-Type Lithium Ion Batteries. *J. Electrochem. Soc.* **2017**, *164*, A6158.

[92] Andre, D.; Kim, S.-J.; Lamp, P.; Lux, S. F.; Maglia, F.; Paschos, O.; Stiaszny, B. Future Generations of Cathode Materials: An Automotive Industry Perspective. *J. Mater. Chem. A* **2015**, *3*, 6709.

[93] Birkl, C. R.; Roberts, M. R.; McTurk, E.; Bruce, P. G.; Howey, D. A. Degradation Diagnostics for Lithium Ion Cells. *J. Power Sources* **2017**, *341*, 373–386.

[94] Dixit, M.; Markovsky, B.; Schipper, F.; Aurbach, D.; Major, D. T. Origin of Structural Degradation during Cycling and Low Thermal Stability of Ni-Rich Layered Transition Metal-Based Electrode Materials. *J. Phys. Chem. C* **2017**, *121*, 22628–22636.

[95] Han, X.; Lu, L.; Zheng, Y.; Feng, X.; Li, Z.; Li, J.; Ouyang, M. A Review on the Key Issues of the Lithium Ion Battery Degradation among the Whole Life Cycle. *eTransportation* **2019**, *1*, 100005.

[96] Pender, J. P.; Jha, G.; Youn, D. H.; Ziegler, J. M.; Andoni, I.; Choi, E. J.; Heller, A.; Dunn, B. S.; Weiss, P. S.; Penner, R. M.; Mullins, C. B. Electrode Degradation in Lithium-Ion Batteries. *ACS Nano* **2020**, *14*, 1243–1295.

[97] Zhang, S.; Zhao, K.; Zhu, T.; Li, J. Electrochemomechanical Degradation of High-Capacity Battery Electrode Materials. *Prog. Mater. Sci.* **2017**, *89*, 479–521.

[98] Kong, L.; Zhang, C.; Wang, J.; Qiao, W.; Ling, L.; Long, D. Free-Standing T-Nb_2O_5/Graphene Composite Papers with Ultrahigh Gravimetric/Volumetric Capacitance for Li-ion Intercalation Pseudocapacitor. *ACS Nano* **2015**, *9*, 11200–11208.

[99] Lim, E.; Jo, C.; Kim, H.; Kim, M.-H.; Mun, Y.; Chun, J.; Ye, Y.; Hwang, J.; Ha, K.-S.; Roh, K. C.; Kang, K.; Yoon, S.; Lee, J. Facile Synthesis of Nb_2O_5@Carbon Core–Shell Nanocrystals with Controlled Crystalline Structure for High-Power Anodes in Hybrid Supercapacitors. *ACS Nano* **2015**, *9*, 7497–7505.

[100] Wang, J.; Li, H.; Shen, L.; Dong, S.; Zhang, X. Nb_2O_5 Nanoparticles Encapsulated in Ordered Mesoporous Carbon Matrix as Advanced Anode Materials for Li Ion Capacitors. *RSC Adv.* **2016**, *6*, 71338–71344.

[101] Luo, G.; Li, H.; Zhang, D.; Gao, L.; Lin, T. A Template-Free Synthesis via Alkaline Route for Nb_2O_5/Carbon Nanotubes Composite as Pseudo-Capacitor Material with High-Rate Performance. *Electrochim. Acta* **2017**, *235*, 175–181.

[102] Wang, L. P.; Yu, L.; Satish, R.; Zhu, J.; Yan, Q.; Srinivasan, M.; Xu, Z. High-Performance Hybrid Electrochemical Capacitor with Binder-Free $Nb_2O_5$5@Graphene. *RSC Adv.* **2014**, *4*, 37389–37394.

[103] Li, H.; Zhu, Y.; Dong, S.; Shen, L.; Chen, Z.; Zhang, X.; Yu, G. Self-Assembled Nb_2O_5 Nanosheets for High Energy–High Power Sodium Ion Capacitors. *Chem. Mater.* **2016**, *28*, 5753–5760.

[104] Lai, C.-H.; Ashby, D.; Moz, M.; Gogotsi, Y.; Pilon, L.; Dunn, B. Designing Pseudocapacitance for Nb_2O_5/Carbide-Derived Carbon Electrodes and Hybrid Devices. *Langmuir* **2017**, *33*, 9407–9415.

[105] Viet, A. L.; Reddy, M.; Jose, R.; Chowdari, B.; Ramakrishna, S. Nanostructured Nb_2O_5 Polymorphs by Electrospinning for Rechargeable Lithium Batteries. *J. Phys. Chem. C* **2009**, *114*, 664–671.

[106] Muruganantham, R.; Sivakumar, M.; Subadevi, R. Polyol Technique Synthesis of Nb_2O_5 Coated on $LiFePO_4$ Cathode Materials for Li-ion Storage. *Ionics* **2017**, 1–11.

[107] Beidaghi, M.; Zhang, C.; Lukatskaya, M.; Maloney, R.; Dunn, B.; Gogotsi, Y. One-Step Synthesis of Carbon Supported Nb_2O_5 Particles for Electrochemical Capacitor Applications by Oxidation of Layered Nb_2C. Meeting Abstracts. 2014; pp 185–185.

[108] Yan, Y.; Lai, C.-H.; Robbennolt, S.; Dunn, B.; Tolbert, S. Nb_4N_5/Nb_2O_5-rGO Composites as Pseudocapacitive Anode Materials for High Power Lithium Ion Batteries. Abstracts of Papers of the American Chemical Society. 2017.

[109] Bard, A. J.; Faulkner, L. R. *Electrochemical Methods: Fundamentals and Applications*, 2nd ed.; Wiley: New York, 2001.

[110] Laoire, C. O.; Plichta, E.; Hendrickson, M.; Mukerjee, S.; Abraham, K. Electrochemical Studies of Ferrocene in a Lithium Ion Conducting Organic Carbonate Electrolyte. *Electrochim. Acta* **2009**, *54*, 6560–6564.

[111] Lou, S.; Cheng, X.; Wang, L.; Gao, J.; Li, Q.; Ma, Y.; Gao, Y.; Zuo, P.; Du, C.; Yin, G. High-Rate Capability of Three-Dimensionally Ordered Macroporous T-Nb_2O_5 through Li^+ Intercalation Pseudocapacitance. *J. Power Sources* **2017**, *361*, 80–86.

[112] Elangovan, E.; Ramamurthi, K. Studies on micro-structural and electrical properties of spray-deposited fluorine-doped tin oxide thin films from low-cost precursor. *Thin Solid Films* **2005**, *476*, 231–236.

[113] Kumagai, N.; Koishikawa, Y.; Komaba, S.; Koshiba, N. Thermodynamics and Kinetics of Lithium Intercalation into Nb_2O_5 Electrodes for a 2 V Rechargeable Lithium Battery. *J. Electrochem. Soc.* **1999**, *146*, 3203–3210.

[114] Yan, L.; Chen, G.; Sarker, S.; Richins, S.; Wang, H.; Xu, W.; Rui, X.; Luo, H. Ultrafine Nb$_2$O$_5$ Nanocrystal Coating on Reduced Graphene Oxide as Anode Material for High Performance Sodium Ion Battery. *ACS Appl. Mater. Interfaces* **2016**, *8*, 22213–22219.

[115] Kumagai, N.; Tanno, K.; Nakajima, T.; Watanabe, N. Structural Changes of Nb$_2$O$_5$ and V$_2$O$_5$ as Rechargeable Cathodes for Lithium Battery. *Electrochim. Acta* **1983**, *28*, 17–22.

[116] Oezer, N.; Barreto, T.; Bueyueklimanli, T.; Lampert, C. M. Characterization of Sol-Gel Deposited Niobium Pentoxide Films for Electrochromic Devices. *Sol. Energy Mater. Sol. Cells* **1995**, *36*, 433–443.

[117] Coşkun, Ö.; Demirel, S.; Atak, G. The Effects of Heat Treatment on Optical, Structural, Electrochromic and Bonding Properties of Nb$_2$O$_5$ Thin Films. *J. Alloys Compd.* **2015**, *648*, 994–1004.

[118] Zhang, S.; Liu, G.; Qiao, W.; Wang, J.; Ling, L. Oxygen Vacancies Enhance the Lithium Ion Intercalation Pseudocapacitive Properties of Orthorhombic Niobium Pentoxide. *J. Colloid Interface Sci.* **2020**, *562*, 193–203.

[119] Lee, K.; Kim, J.; Mok, I.; Na, H.; Ko, D.; Sohn, H.; S, L. RESET-First Unipolar Resistance Switching Behavior in Annealed Nb$_2$O$_5$ Films. *Thin Solid Films* **2014**, *558*, 423–429.

[120] Cava, R. J.; Batlogg, B.; Krajewski, J.; Poulsen, H.; Gammel, P.; Peck Jr, W.; Rupp Jr, L. Electrical and Magnetic Properties of Nb$_2$O$_{5-\delta}$ Crystallographic Shear Structures. *Phys. Rev. B: Condens. Matter Mater. Phys.* **1991**, *44*, 6973.

[121] Aufray, M.; Menuel, S.; Fort, Y.; Eschbach, J.; Rouxel, D.; Vincent, B. Synthesis of Nanosized Niobium Oxides and Lithium Niobate Particles and Their Characterization by XPS Analysis. *J. Nanosci. Nanotechnol.* **2009**, *9*, 4780–4785.

[122] Pittman, R. M.; Bell, A. T. Raman Studies of the Structure of Niobium Oxide/Titanium Oxide (Nb$_2$O$_5$/ TiO$_2$). *J. Phys. Chem.* **1993**, *97*, 12178–12185.

[123] McConnell, A. A.; Aderson, J.; Rao, C. Raman Spectra of Niobium Oxides. *Spectrochim. Acta A Mol. Biomol. Spectrosc.* **1976**, *32*, 1067–1076.

[124] Hardcastle, F. D.; Wachs, I. E. Determination of Niobium-Oxygen Bond Distances and Bond Orders by Raman Spectroscopy. *Solid State Ion.* **1991**, *45*, 201–213.

[125] Jehng, J. M.; Wachs, I. E. Structural Chemistry and Raman Spectra of Niobium Oxides. *Chem. Mater.* **1991**, *3*, 100–107.

[126] Chen, D.; Wang, J.-H.; Chou, T.-F.; Zhao, B.; El-Sayed, M. A.; Liu, M. Unraveling the Nature of Anomalously Fast Energy Storage in T-Nb2O5. *J. Am. Chem. Soc.* **2017**, *139*, 7071–7081.

[127] Ikeya, T.; Senna, M. Change in the Structure of Niobium Pentoxide due to Mechanical and Thermal Treatments. *J. Non Cryst. Solids* **1988**, *105*, 243–250.

[128] Bredar, A. R.; Chown, A. L.; Burton, A. R.; Farnum, B. H. Electrochemical Impedance Spectroscopy of Metal Oxide Electrodes for Energy Applications. *ACS Appl. Energy Mater.* **2020**, *3*, 66–98.

[129] Aricò, A. S.; Bruce, P.; Scrosati, B.; Tarascon, J.-M.; Van Schalkwijk, W. Nanostructured Materials for Advanced Energy Conversion and Storage Devices. *Nat. Mater.* **2005**, *4*, 366–377.

[130] Qian, S.; Yu, H.; Yan, L.; Zhu, H.; Cheng, X.; Xie, Y.; Long, N.; Shui, M.; Shu, J. High-Rate Long-Life Pored Nanoribbon VNb_9O_{25} Built by Interconnected Ultrafine Nanoparticles as Anode for Lithium-Ion Batteries. *ACS Appl. Mater. Interfaces* **2017**, *9*, 30608–30616.

[131] Zhang, J.; Chen, H.; Sun, X.; Kang, X.; Zhang, Y.; Xu, C.; Zhang, Y. High Intercalation Pseudocapacitance of Free-Standing T-Nb_2O_5 Nanowires@Carbon Cloth Hybrid Supercapacitor Electrodes. *J. Electrochem. Soc.* **2017**, *164*, A820.

[132] Wang, X.; Li, G.; Tjandra, R.; Fan, X.; Xiao, X.; Yu, A. Fast Lithium-Ion Storage of Nb_2O_5 Nanocrystals *In Situ* Grown on Carbon Nanotubes for High-Performance Asymmetric Supercapacitors. *RSC Adv.* **2015**, *5*, 41179–41185.

[133] Wang, L.; Bi, X.; Yang, S. Partially Single-Crystalline Mesoporous Nb_2O_5 Nanosheets in between Graphene for Ultrafast Sodium Storage. *Adv. Mater.* **2016**, *28*, 7672–7679.

[134] Yamamura, S.; Koshika, H.; Nishizawa, M.; Matsue, T.; Uchida, I. *In situ* Conductivity Measurements of $LiMn_2O_4$ Thin Films during Lithium Insertion/Extraction by Using Interdigitated Microarray Electrodes. *J. Solid State Electrochem.* **1998**, *2*, 211–215.

[135] Nishizawa, M.; Ise, T.; Koshika, H.; Itoh, T.; Uchida, I. Electrochemical *In-Situ* Conductivity Measurements for Thin Film of Li_{1-x} Mn_2O_4 Spinel. *Chem. Mater.* **2000**, *12*, 1367–1371.

[136] Ouyang, C.; Shi, S.; Wang, Z.; Huang, X.; Chen, L. Experimental and Theoretical Studies on Dynamic Properties of Li Ions in $Li_xMn_2O_4$. *Solid State Commun.* **2004**, *130*, 501–506.

[137] Kanoh, H.; Feng, Q.; Hirotsu, T.; Ooi, K. AC Impedance Analysis for Li^+ Insertion of a Pt/λ-MnO_2 Electrode in an Aqueous Phase. *J. Electrochem. Soc.* **1996**, *143*, 2610–2615.

[138] Le Thai, M.; Liu, Y.; Wang, H.; Dutta, R. K.; Yan, W.; Hemminger, J. C.; Wu, R. Q.; Penner, R. M. *In-situ* Electrical Conductivity of Li_xMnO_2 Nanowires as a Function of "x" and Size. *Chem. Mater.* **2015**, 3494–3504.

[139] Nobili, F.; Croce, F.; Scrosati, B.; Marassi, R. Electronic and Electrochemical Properties of $Li_xNi_{1-y}Co_yO_2$ Cathodes Studied by Impedance Spectroscopy. *Chem. Mater.* **2001**, *13*, 1642–1646.

[140] Kang, H.; Lee, J.; Rodgers, T.; Shim, J.-H.; Lee, S. Electrical Conductivity of Delithiated Lithium Cobalt Oxides: Conductive Atomic Force Microscopy and Density Functional Theory Study. *J. Phys. Chem. C* **2019**,

[141] Wang, S.; Yan, M.; Li, Y.; Vinado, C.; Yang, J. Separating Electronic and Ionic Conductivity in Mix-Conducting Layered Lithium Transition-Metal Oxides. *J. Power Sources* **2018**, *393*, 75–82.

[142] Spinner, N. S.; Palmieri, A.; Beauregard, N.; Zhang, L.; Campanella, J.; Mustain, W. E. Influence of conductivity on the capacity retention of NiO anodes in Li-ion batteries. *J. Power Sources* **2015**, *276*, 46–53.

[143] Chiu, H.-C.; Lu, X.; Zhou, J.; Gu, L.; Reid, J.; Gauvin, R.; Zaghib, K.; Demopoulos, G. P. Capacity Fade Mechanism of $Li_4Ti_5O_{12}$ Nanosheet Anode. *Adv. Energy Mater.* **2017**, *7*, 1601825.

[144] Palmieri, A.; Yazdani, S.; Kashfi-Sadabad, R.; Karakalos, S. G.; Ng, B.; Oliveira, A.; Peng, X.; Pettes, M. T.; Mustain, W. E. Improved Capacity Retention of Metal Oxide Anodes in Li-Ion Batteries: Increasing Intraparticle Electronic Conductivity through Na Inclusion in Mn_3O_4. *ChemElectroChem* **2018**, *5*, 2059–2063.

[145] Baudais, M.; Dahn, J. *In situ* Technique for Measuring the Resistivity of Lithium Intercalation Compounds as a Function of Lithium Composition. *Solid State Ion.* **1993**, *66*, 175–181.

[146] Sauvage, F.; Tarascon, J.-M.; Baudrin, E. *In Situ* Measurements of Li Ion Battery Electrode Material Conductivity: Application to Li_xCoO_2 and Conversion Reactions. *J. Phys. Chem. C* **2007**, *111*, 9624–9630.

[147] Wang, C.; Patil, P.; Appleby, A. J.; Little, F. E.; Kesmez, M.; Cocke, D. L. *In situ* Ionic/Electric Conductivity Measurement of $La_{0.55}Li_{0.35}TiO_3$ Ceramic at Different Li Insertion Levels. *J. Electrochem. Soc.* **2004**, *151*, A1196–A1201.

[148] Wang, C.; Rakotondrainibe, A.; Appleby, A. J.; Little, F. E. Characterization of Metal Hydride Electrodes via Microperturbation and *In Situ* Intrinsic Resistance Measurement. *J. Electrochem. Soc.* **2000**, *147*, 4432–4439.

[149] Landa-Medrano, I.; de Larramendi, I. R.; Ortiz-Vitoriano, N.; Pinedo, R.; de Larramendi, J. I. R.; Rojo, T. *In Situ* Monitoring of Discharge/Charge Processes in $Li-O_2$ Batteries by Electrochemical Impedance Spectroscopy. *J. Power Sources* **2014**, *249*, 110–117.

[150] Pollak, E.; Salitra, G.; Baranchugov, V.; Aurbach, D. *In Situ* Conductivity, Impedance Spectroscopy, and *Ex Situ* Raman Spectra of Amorphous Silicon During the Insertion/Extraction of Lithium. *J. Phys. Chem. C* **2007**, *111*, 11437–11444.

[151] Wilson, J.; Schwartz, D.; Adler, S. B. Nonlinear Electrochemical Impedance Spectroscopy for Solid Oxide Fuel Cell Cathode Materials. *Electrochim. Acta* **2006**, *51*, 1389–1402.

[152] Buller, S.; Thele, M.; De Doncker, R. W. a. a.; Karden, E. Impedance-Based sSmulation Models of Supercapacitors and Li-Ion Batteries for Power Electronic Applications. *IEEE Trans. Ind. Appl.* **2005**, *41*, 742–747.

[153] Zhu, Y.; Gao, T.; Fan, X.; Han, F.; Wang, C. Electrochemical Techniques for Intercalation Electrode Materials in Rechargeable Batteries. *Acc. Chem. Res.* **2017**, *50*, 1022–1031.

[154] Xiang, C.; Yang, Y.; Penner, R. M. Cheating the Diffraction Limit: Electrodeposited Nanowires Patterned by Photolithography. *ChemComm* **2009**, 859–873.

[155] Xiang, C.; Kung, S.-C.; Taggart, D. K.; Yang, F.; Thompson, M. A.; Guell, A. G.; Yang, Y.; Penner, R. M. Lithographically Patterned Nanowire Electrodeposition: A Method for Patterning Electrically Continuous Metal Nanowires on Dielectrics. *ACS Nano* **2008**, *2*, 1939–1949.

[156] Menke, E. J.; Thompson, M. A.; Xiang, C.; Yang, L. C.; Penner, R. M. Lithographically Patterned Nanowire Electrodeposition. *Nat. Mater.* **2006**, *5*, 914–919.

[157] Le Thai, M.; Chandran, G. T.; Dutta, R. K.; Li, X.; Penner, R. M. 100k Cycles and Beyond: Extraordinary Cycle Stability for MnO_2 Nanowires Imparted by a Gel Electrolyte. *ACS Energy Lett.* **2016**, *1*, 57–63.

[158] Inamoto, J.-i.; Fukutsuka, T.; Miyazaki, K.; Abe, T. Investigation on Surface-Film Formation Behavior of $LiMn_2O_4$ Thin-Film Electrodes in $LiClO_4$/Propylene Carbonate. *ChemistrySelect* **2017**, *2*, 2895–2900.

[159] Weibin, Z.; Weidong, W.; Xueming, W.; Xinlu, C.; Dawei, Y.; Changle, S.; Liping, P.; Yuying, W.; Li, B. The Investigation of NbO_2 and Nb_2O_5 Electronic Structure by XPS, UPS and First Principles Methods. *Surf. Interface Anal.* **2013**, *45*, 1206–1210.

[160] Liu, C.-P. First-Principles Studies of Transition Metal Oxides and Sulfides in Electrochemical Energy Storage Applications. Ph.D., University of Califonia, Los Angeles, Department of Materials Science and Engineering, 2015.

[161] Choi, S.; Wang, J.; Cheng, Z.; Liu, M. Surface Modification of Ni-YSZ Using Niobium Oxide for Sulfur-Tolerant Anodes in Solid Oxide Fuel Cells. *J. Electrochem. Soc.* **2008**, *155*, B449–B454.

[162] Sathasivam, S.; Williamson, B. A.; Althabaiti, S. A.; Obaid, A. Y.; Basahel, S. N.; Mokhtar, M.; Scanlon, D. O.; Carmalt, C. J.; Parkin, I. P. Chemical Vapor Deposition Synthesis and Optical Properties of Nb_2O_5 Thin Films with Hybrid Functional Theoretical Insight into the Band Structure and Band Gaps. *ACS Appl. Mater. Interfaces* **2017**, *9*, 18031–18038.

[163] Aegerter, M. A. Sol-Gel Niobium Pentoxide: A Promising Material for Electrochromic Coatings, Batteries, Nanocrystalline Solar Cells and Catalysis. *Sol. Energy Mater. Sol. Cells* **2001**, *68*, 401–422.

[164] Maček, M.; Orel, B.; Krašovec, U. O. The Effect of Lithiation on the Electrochromism of Sol-Gel Derived Niobium Oxide Films. *J. Electrochem. Soc.* **1997**, *144*, 3002–3010.

[165] Andoni, I.; Ziegler, J. M.; Jha, G.; Gadre, C. A.; Flores-Zuleta, H.; Dai, S.; Qiao, S.; Xu, M.; Chen, V. T.; Pan, X.; Penner, R. M. Investigating the Degradation of Nb_2O_5 Thin Films Across 10,000 Lithiation/Delithiation Cycles. *ACS Appl. Energy Mater.* **2021**, *4*, 6542–6552.

[166] Moshkovich, M.; Gofer, Y.; Aurbach, D. Investigation of the Electrochemical Windows of Aprotic Alkali Metal (Li, Na, K) Salt Solutions. *J. Electrochem. Soc.* **2001**, *148*, E155.